BOUNDARY-LAYER INSTABILITIES ON A COOLED FLARED CONE AT MACH 6

A Dissertation

by

FARHAN SHAKIL AHMED SIDDIQUI

Submitted to the Office of Graduate and Professional Studies of
Texas A&M University
in partial fulfillment of the requirements for the degree of

DOCTOR OF PHILOSOPHY

Co-Chairs of Committee,	William Saric
	Rodney Bowersox
Committee Members,	Helen Reed
	Simon North
Head of Department,	Srinivas Vadali

August 2021

Major Subject: Aerospace Engineering

Copyright 2021 Farhan Shakil Ahmed Siddiqui

ABSTRACT

There are significant challenges involved in the design of hypersonic vehicles/projectiles, one of them being the fluid dynamics on the surface. The fluid dynamics can affect the thermal load, structural load and handling of the vehicle. Boundary-layer transition alone can account for an order of magnitude higher heating and thus it is important to understand how this transition process occurs. In this experiment the boundary layer on a sharp-tip, part-straight, part-flared actively cooled cone is being studied in a quiet Mach 6 wind tunnel. The Mack mode and its associated secondary instability dominate above Mach 4 as a cause of boundary-layer transition and is being focused on in this study. The role of curvature is also included in order to study the effects of Görtler vortices. Boundary-layer transition was tracked using embedded thermocouples, focusing schlieren and Focused Laser Differential Interferometry (FLDI). The Mack-mode disturbances were observed using a high-speed camera and spectral data were taken at a point in the boundary layer using focusing schlieren and FLDI. Constant Temperature Anemometry (CTA) was used in the form of hot-film probes that were traversed in the boundary layer to do azimuthal sweeps and showed periodic mass-flux variations with a wavenumber of 90, which were attributed to Görtler vortices. Distributed Roughness Elements (DREs) were placed at the neutral point with the same wavenumber seen from the hot-film data to force a 3-D breakdown. FLDI was used to probe six points in the boundary layer simultaneously and captured the Mack-mode instability and its harmonics. Computational work confirmed the experimental findings. This work creates a database for Direct Numerical Simulations (DNS) and Non-linear Parabolized Stability Equations (NPSE) computations and adds to the current knowledge of hypersonic boundary-layer transition.

DEDICATION

To my parents, for everything.

ACKNOWLEDGMENTS

I would like to acknowledge first and foremost the chairs of my committee, Dr. Saric, and Dr. Bowersox. Dr. Saric has been very involved in this project and that has been very helpful when working on such a complex problem. He has taught me the value of attention to detail, true critical thinking about every problem, and to never accept mediocre data. Dr. Bowersox gave me a chance by hiring me as a summer undergrad and has been a fantastic mentor over the years. He is one of the busiest people I know and somehow also one of the most patient. I am honored to have worked closely with both of them.

Dr. Reed has always been very helpful, from teaching me about shockwaves in undergrad to boundary-layer stability in graduate school. She has also been instrumental as a computational expert to bounce ideas off of when analyzing data. Dr. North brings great criticism, with a science perspective, and makes us really think about the problems we're facing.

Dr. Gragston from UTSI was instrumental in setting up the Focused Laser Differential Interferometry diagnostic. I have learned a lot about laser diagnostics from him and look forward to working with him in the future.

I have to acknowledge my graduate student mentors, Dr. Ian Neel and Dr. Andrew Leidy. They were the senior graduate students at the NAL and I learned a lot from them. Several other graduate students have been part of the process with me, Heather Kostak, Casey Broslawski, Tyler Dean, and several others. I thank them for the countless hours spent running wind tunnels, helping fix everything that broke, and for their friendship.

I thank Cecil Rhodes for being able to fix almost anything, teaching me how to use multiple tools, mechanical tricks, being a sounding board while I troubleshoot, and always being around with a cheerful spirit.

Rebecca Marianno and Colleen Leatherman work tirelessly behind the scenes to keep everything organized and our labs running well and we appreciate them very much.

I am also thankful for the countless researchers that have come before me and accomplished

so much with so little. I am always astounded by the work earlier researchers such as Mack, Morkovin, Reshotko, Saric, and many others were able to do with the limited technology they had. We truly stand on the shoulders of giants.

Last but not least, I thank my wife for being so patient and loving while I work long hours. And my family for always believing in me and supporting me while I pursue my dreams.

CONTRIBUTORS AND FUNDING SOURCES

Contributors

This work was supported by a dissertation committee consisting of Dr. Saric (chair), Dr. Bowersox (co-chair), Dr. Reed (committee member) of the Department of Aerospace Engineering and Dr. North (committee member) of the Department of Chemistry.

The computational work listed in Sec. 3.4 was carried out by Daniel Mullen and Alex Moyes under the supervision of Dr. Reed at the Computational Stability & Transition (CST) Lab at Texas A&M University.

Funding Sources

This work has been supported by the George Eppright '26 endowed chair and the Texas A&M Aerospace Engineering Department.

The author gratefully acknowledges support for this work in part from a grant from the Department of Defense Office of the Under Secretary of Defense (Vannevar Bush Faculty Fellowship Grant # N00014-18-1-3020). Its contents are solely the responsibility of the authors and do not necessarily represent the official views of the Department of Defense Office of the Under Secretary of Defense.

NOMENCLATURE

2-D	Two-dimensional
3-D	Three-dimensional
7DC	7-degree cone model
91-6	Name of the cooled, partially-flared 18-inch NASA model
93-10	Name of the partially-flared 20-inch NASA model
ACE	Adjustable Contour Expansion wind tunnel
AEDC	Arnold Engineering Development Center
CEV	Crew Exploration Vehicle (NASA)
CFD	Computational Fluid Dynamics
CST	Computational Stability & Transition lab
CTA	Constant Temperature Anemometry
CVA	Constant Voltage Anemometry
DAQ	Data acquisition
DNS	Direct Numerical Simulations
DOE	Diffractive Optical Element
DPLR	Data Parallel Line Relaxation
DREs	Distributed Roughness Elements
DS	Depth of sharp focus of focusing schlieren system
DU	Depth of unsharp focus of focusing schlieren system
EPIC	Euonymous Parabolized Instability Code
f_0	Frequency of fundamental second-mode waves
FLDI	Focused Laser Differential Interferometry

h	Enthalpy
k	Thermal conductivity
LA-FLDI	Linear Array-Focused Laser Differential Interferometry
LDI	Laser Differential Interferometry
LPSE	Linear Parabolized Stability Equations
LST	Linear Stability Theory
M	Mach number
M_∞	Freestream Mach number
M_e	Boundary-layer edge Mach number
$\overline{M}$	Relative Mach number
M6QT	Mach 6 Quiet Tunnel
M6NTC	Mach 6 Nozzle Test Chamber
n	Index of refraction
NAL	National Aerothermochemistry Laboratory
NASA	National Aeronautics and Space Administration
Ni	Nickel
NPSE	Non-linear Parabolized Stability Equations
Nu	Nusselt number
OPL	Optical path length
p	Pressure
PET	Polyethylene Terephthalate
Pr	Prandtl number
PSE	Parabolized Stability Equations
r	Radial coordinate of cylindrical coordinate system
R	Universal gas constant

Re	Reynolds number
Re_∞	Freestream Reynolds number
RMS	Root Mean Square
RTV	Room Temperature Vulcanizing
SNR	Signal to noise ratio
T	Temperature
TAMU	Texas A&M University
T-S	Tollmien-Schlichting
T_w	Operating wire temperature
T_t	Total temperature
UHT	Ultra-High Temperature
UTSI	University of Tennessee Space Institute
$\mathbf{V}$	Velocity vector
VI	Virtual Interface
z	Axial coordinate of cylindrical coordinate system
γ	Ratio of specific heats
δ	Boundary-layer height
η	Wire-recovery factor (T_e/T_t)
θ	Azimuthal coordinate of cylindrical coordinate system
λ	Wavelength
μ	Viscosity coefficient
ρ	Density
τ	Temperature loading factor $(T_w - \eta T_t)/T_t$
τ_{ii}	Normal viscous stress component
τ_{ij}	Shear stress component

TABLE OF CONTENTS

Page

LIST OF FIGURES

FIGURE Page

LIST OF TABLES

TABLE Page

1. INTRODUCTION*

1.1 Motivation

Hypersonic vehicles and projectiles have become a very important venue of research, with countries around the world vying to have the most advanced knowledge and vehicles. As countries race to be most dominant in space it is obvious that having advanced hypersonics programs is crucial. Several commercial ventures are also interested in hypersonic flight, with some companies looking far ahead and hoping to get a head start on what could be the future of transportation.

The hypersonic flow regime is usually defined to be Mach 5 and above. When flow is faster than the speed of sound (Mach 1) it is considered supersonic. Hypersonic flow is more arbitrarily defined, definitions of the start of hypersonic flow can range from as low as Mach 3 to as high as Mach 10, but most often it is defined to be Mach 5. There are changes in flow characteristics at these speeds [1] (also shown in Fig. 1.1) such as:

- *Thin shock layers.* It is common for shocks to lie very close to the surface of a body. This can also lead to Shock-Boundary Layer Interactions (SBLI).
- *Entropy layer.* Entropy of the flow increases across a shock and stronger shocks lead to a higher increase in entropy. The streamlines near the strong, nearly normal part of the shock see a larger increase in entropy than streamlines further away from the centerline. This creates an entropy layer with strong entropy gradients and this entropy layer flows downstream from the nose and affects the boundary layer as it is a region of strong vorticity as related from Crocco's theorem of classical compressible flow.
- *Viscous Interaction.* As fluid slows down in the boundary layer there is viscous dissipation of kinetic energy to internal energy of the gas which increases the temperature. This in turn causes thick boundary layers to maintain the required mass flow. The inviscid solutions are invalid.

*Parts of this chapter are reprinted with permission from [1][2][3].

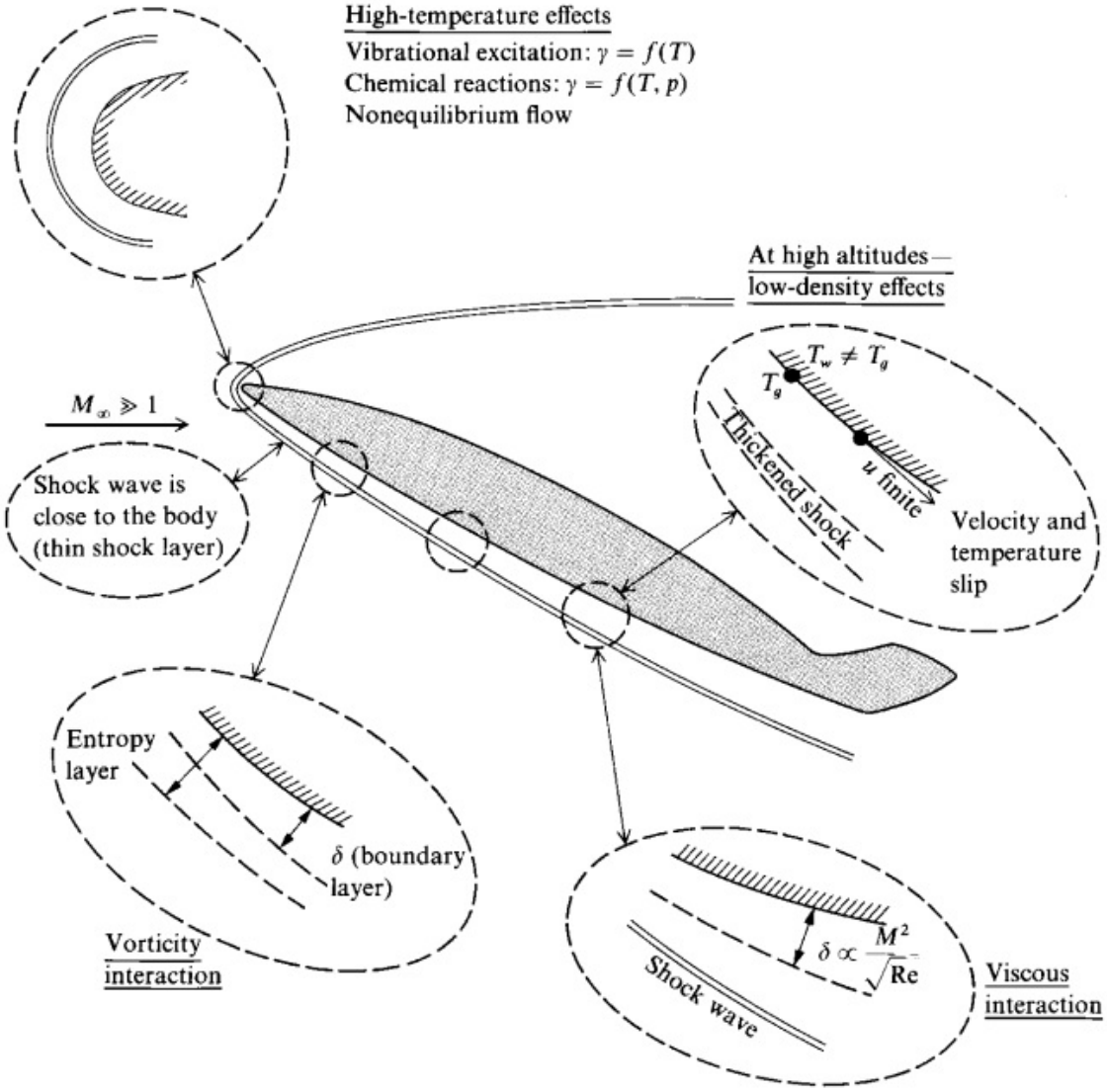

Figure 1.1: Characteristics of hypersonic flow (Reprinted with permission from [1]).

- *High-Temperature flow.* The extreme temperatures reached in a hypersonic boundary layer can cause dissociation and ionization of the gas. This creates a chemically reacting boundary layer which causes extreme temperatures and nonequilibrium flow.

- *Low-Density Flow.* At high altitudes the density of gases can be very low. The high temperatures of hypersonic flow can also lead to lower densities. Conventional viscous no-slip conditions can begin to fail and other models have to be used.

Hypersonic boundary-layer transition is still not fully understood. The transition from laminar to turbulent is dependent on several factors and the mechanisms that lead to transition at hypersonic speeds are very different from those at subsonic and supersonic speeds. It is important to understand the breakdown mechanisms in order to better estimate transition on new vehicles. Experimental hypersonic planes, such as the X-43, and re-entry vehicles, such as the Orion CEV, have to be designed with transition in mind since turbulent boundary layers often have an order of magnitude higher heating than laminar boundary layers. Not understanding precisely how transition occurs can lead to inefficient vehicle design. Current aircraft design has to be conservative and this leads to unnecessarily heavy vehicles because of excess thermal protection [9]. Better prediction tools would better equip designers and make for lighter aircraft or more payload capabilities [10].

Ideally researchers would be able to carry out tests with real hypersonic planes and/or projectiles and come to conclusions about how boundary-layer transition is happening. Unfortunately this would require a lot of time and funding and some measurements would be impossible to make on a flight vehicle. Some flight tests have been done but most research is done either in wind tunnels or using Computational Fluid Dynamics (CFD), sometimes as a precursor to flight tests so flight vehicle designers know what to expect from their expensive flights. CFD can answer a lot of questions and is often used in conjunction with experiments to verify and validate each other. Wind tunnel testing makes up the bulk of experimental work done in hypersonics, models can be designed with many variations and tested at whatever Mach number the facility is designed for. It is worth noting that wind tunnels don't usually recreate the conditions seen in flight. Some wind tunnels are "cold" facilities that recreate the aerodynamics, boundary layers, and shock interactions but don't create the same level of heat seen in actual flight. Some wind tunnels do create flight-like temperatures but even then there are differences from what would be seen in flight, such as the freestream disturbance levels being higher [11].

1.2 Theoretical background

1.2.1 Navier-Stokes Equations

The governing equations of fluid flow for unsteady, compressible, viscous, 3-D flows are the Navier-Stokes equations. They are a set of partial differential equations that are arrived at by analyzing a moving fluid element. They consist of a continuity equation based on the conservation of mass, momentum equations based on conservation of momentum, and an energy equation.

The Navier-Stokes equations can be simplified by considering two-dimensional, steady flow, and nondimensionalizing. Similarity parameters emerge like γ (ratio of specific heats), Mach number, Reynolds number, and Prandtl number. For a boundary layer in hypersonic flow, some assumptions can be made,

$$\delta << c \tag{1.1}$$

$$\frac{1}{Re_\infty} = O(\delta^2) \tag{1.2}$$

where δ is the boundary-layer height, *c* is the scale of the body/vehicle, and Re_∞ is the freestream Reynolds number. The assumptions are that the boundary layer is thin and the Reynolds number is high. After applying these assumptions to the nondimensional Navier-Stokes equations they can be simplified for a boundary layer. The continuity equation,

$$\frac{\partial(\rho u)}{\partial x} + \frac{\partial(\rho v)}{\partial y} = 0 \tag{1.3}$$

x-momentum equation,

$$\rho u\frac{\partial u}{\partial x} + \rho v\frac{\partial u}{\partial y} = -\frac{dp_e}{dx} + \frac{\partial}{\partial y}(\mu\frac{\partial u}{\partial y}) \tag{1.4}$$

y-momentum equation,

$$\frac{\partial p}{\partial y} = 0 \tag{1.5}$$

energy equation,

$$\rho u \frac{\partial h}{\partial x} + \rho v \frac{\partial h}{\partial y} = \frac{\partial}{\partial y}(k \frac{\partial T}{\partial y}) + u \frac{dp_e}{dx} + \mu (\frac{\partial u}{\partial y})^2 \tag{1.6}$$

For a calorically perfect gas,

$$p = \rho R T \tag{1.7}$$

$$h = c_p T \tag{1.8}$$

Thus Eq. 1.3, 1.4, 1.6, 1.7, and 1.8 are five equations for the five unknowns *u*, *v*, ρ, *T*, and *h*. These equations can be solved numerically using different boundary conditions for different configurations.

1.2.2 Linear Stability Theory

Linear Stability Theory (LST) is one way to solve the complex non-linear Navier-Stokes equations for 2-D flows, compressible flows, and 3-D flows. The basic premise of LST is to linearise the Navier Stokes equations by writing each term in the equation in terms of temporally mean and fluctuating components,

$$u(x,t) = U(x) + u'(x,t) \tag{1.9}$$

The Navier-Stokes equations can now be written in terms of the mean and fluctuating components of each flow quantity. The terms with only mean flow satisfy the original Navier-Stokes equations and can be removed. The terms with products of disturbances can be deemed negligible as the fluctuations are assumed to be very small. This results in a set of linear disturbance

equations. These equations can be assumed to have a normal-mode solution [12],

$$q'(x,y,z,t) = q(y)exp[i(\alpha x + \beta z - \omega t)] + C.C. \tag{1.10}$$

where q' is any of the fluctuation variables, α is the chordwise wavenumber, β is the spanwise wavenumber, ω is the frequency, and *C.C.* is the complex conjugate. In general, α and β are complex and ω is real. The Navier-Stokes equations can now be written in terms of this normal-mode solution, this results in an eighth-order system which can be reduced to a sixth-order system by an order of magnitude simplification which is only valid for large Reynolds numbers as shown by Dunn and Lin [13].

In compressible flows, boundary layers have inviscid instabilities and they become more prominent with increasing Mach number. Thus it is useful to approximate the flow as inviscid to arrive at some results that are very useful for high Mach number, high Reynolds number flows such as those present in hypersonic boundary layers. For infinite Reynolds number, the Navier-Stokes equations are simplified. The *z*-momentum and energy equations are uncoupled from the rest of the equations. Two first-order equations can then be written for *v* and *p*,

$$(\alpha U + \beta W - \omega)Dv = (\alpha DU + \beta DW)v + i(\alpha^2 + \beta^2)[T - M_e^2(\frac{\alpha U + \beta W - \omega}{\alpha^2 + \beta^2})]\frac{p}{\gamma M_e^2} \tag{1.11}$$

$$D(\frac{p}{\gamma M_e^2}) = -i\rho(\alpha U + \beta W - \omega)v \tag{1.12}$$

where M_e is the edge Mach number. A relative Mach number, $\overline{M}$ is defined to further simplify the equations,

$$\overline{M} = \frac{(\alpha U + \beta W - \omega)M_e}{(\alpha^2 + \beta^2)^{1/2}T^{1/2}} \tag{1.13}$$

Physically the relative Mach number is the local Mach number of the mean flow in the direction

of the wavenumber vector relative to the phase speed of a neutral wave. Using the relative Mach number Eq. 1.22 and 1.23 can be written as a single second-order equation [14],

$$\frac{\partial^2\psi}{\partial y^2} + (1 - \overline{M}^2)\frac{\partial^2\psi}{\partial x^2} + f(\overline{M}, \psi, \frac{\partial\psi}{\partial y}) = 0 \tag{1.14}$$

where

$$\psi = \frac{v}{\alpha U + \beta W - \omega} \tag{1.15}$$

When $\overline{M}$<1, the solution to this equation is elliptic and the eigenvalue is unique, this is the case for all subsonic flows. When $\overline{M}$>1 on the other hand, the solution is hyperbolic and infinite solutions exist, this means that there can be multiple instability modes. The location where $\overline{M}$=1 is called the sonic line, above this line the solutions are elliptic and below it the solutions are hyperbolic.

Lees and Lin [15] studied the Rayleigh inflection-point criterion for 2-D inviscid disturbances and found that a generalized inflection point exists for compressible boundary layers where

$$D(\rho DU) = 0 \tag{1.16}$$

at $y_s > y_0$ where y_0 is the point where U = 1-1/M_e, M_e being the edge Mach number. Since the boundary layer in supersonic flow will always have such a point, it is always subject to inviscid instabilities [14].

1.2.3 e^N method

One of the earliest transition prediction mechanisms was to combine LST and experimental work to determine a location where the boundary layer had transitioned from laminar to turbulent. Smith and Gamberoni [16] found the Tollmien-Schlichting wave to undergo an amplification of e^9 times its amplitude at the beginning of its growth by the time the transition point was reached. They demonstrated that this could be used as a predictor of transition for low-speed, low-turbulence

flows. Van Ingen [17] independently developed a semi-empirical method to predict transition location on a flat plate in a low-speed, low-disturbance wind tunnel. He found that transition started when the calculated amplification ratio of unstable disturbances reached $e^{7.8}$ and ended at e^{10}. Conversely the amplification factor N can be defined,

$$N = ln(\frac{A}{A_0}) \tag{1.17}$$

where A is the disturbance amplitude at a location and A_0 is its initial amplitude.

The e^N method for predicting transition works well for 2-D incompressible flows but it does not take into account receptivity and the effects it has on boundary-layer transition. Instabilities that are 3-D in nature, like crossflow and Görtler instabilities, are very sensitive to surface roughness, curvature, and initial amplitudes. Thus, Morkovin and Reshotko cautioned that the e^N method has to be used carefully for hypersonic flows where 3-D instabilities are the dominant cause of boundary-layer transition [18]. Regardless, when comparing different situations using the N-factor, the environmental disturbance level and geometry must be similar, or discrepancies can abound [14]. Owing to its popularity, the N-factor is still used as a growth indicator for 3-D boundary layers, relating amplification of modes from some computed or measured initial condition.

1.2.4 Mack modes

Leslie Mack is credited with one of the breakthrough accomplishments in the field of compressible flows because of his discovery of multiple solutions to the governing equations. In Sec. 1.2.2, the Navier-Stokes equations were simplified and linearized by writing them in terms of small fluctuating quantities. A normal mode solution was used and the equation written in terms of the relative Mach number ($\overline{M}$) which is the relative Mach number between the local mean velocity and the speed of the instability. When $\overline{M}$<1 the solution is elliptic and this is the case for subsonic flows. When $\overline{M}$>1 the solution is hyperbolic and multiple modes exist, these are called Mack modes. There is a line in the boundary layer where $\overline{M}$=1 and this is called the sonic line. Physically, the Mack mode disturbances are acoustic waves that reflect inviscidly between the solid wall

and the sonic line in the boundary layer. Thus the sonic line acts as a wave guide. The hyperbolic solution of the Navier-Stokes equations is oscillatory. A representation of the oscillating Mack mode is shown in Fig. 1.2.

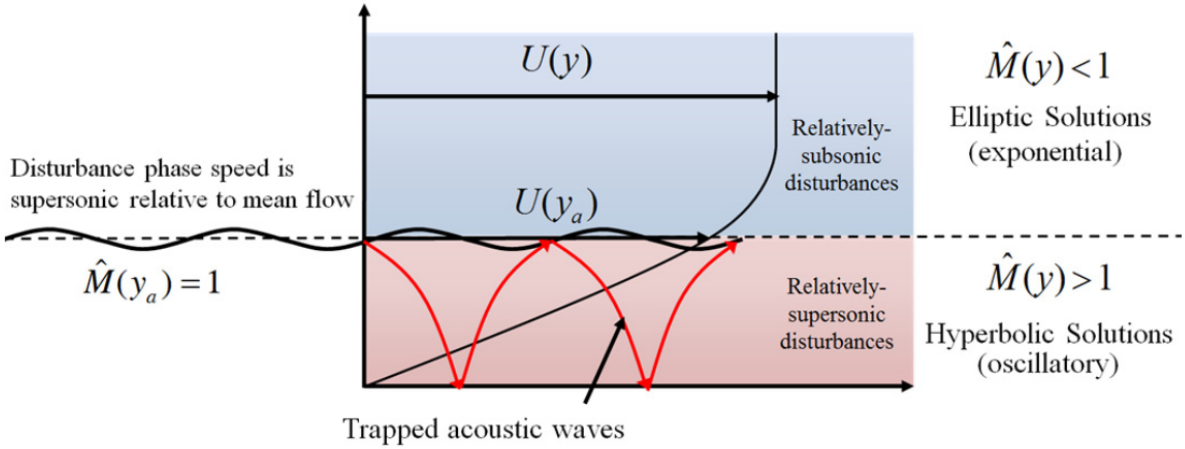

Figure 1.2: Acoustic mode instability in a hypersonic boundary layer (Reprinted with permission from [2]).

The first linear-stability mode is three-dimensional and is the most dominant instability at lower Mach numbers. For a flat plate, the Mack mode appears at M=2.2, it is a two-dimensional (streamwise), inviscid instability. As the Mach number increases the Mack mode becomes more unstable and above Mach 4 it is the most unstable instability in the boundary layer. Mack-mode waves have a wavelength dependent on the boundary-layer height as the sonic line location is dependent on the boundary-layer height. In general, $\lambda \sim 2\delta$ and this results in the Mack-mode instability having a high frequency ($\sim$300 kHz) due to the thin boundary layers (for the present work).

1.2.5 Görtler instability

Görtler vortices are steady, streamwise-oriented, counter-rotating vortices that are induced by curvature in the streamwise direction [19]. In general the vortices have a spanwise wavelength

on the order of the boundary-layer height. According to the Rayleigh circulation criterion, the necessary condition for the existence of an axisymmetric inviscid instability is,

$$\frac{d((rU)^2)}{dr} < 0 \tag{1.18}$$

anywhere in the flow, where r is the distance from the surface and U is the streamwise velocity. Drazin and Reid [20] show the derivation for curved surfaces. For a closed system of a parallel flow (Couette flow) this takes the form of the Taylor instability [21]. For an open system with a parallel basic state this takes the form of the Dean instability [22]. For an open system with a nonparallel basic state, as is the case for a boundary-layer over a concave surface, the Görtler instability is seen.

For a boundary layer over a concave surface rU = 0 at the center of radius of curvature, and rU=0 at the wall. Thus there is a point where rU reaches a maximum and an inflection point is present. Görtler [23] solved the disturbance equations for this case and showed the solutions to be in the form of vortices, as seen in Fig. 1.3. Physically, these vortices can be explained as the wall-normal pressure gradient not being sufficient to suppress the angular momentum of particles rotating due to curvature. The Görtler instability is important because it can cause the boundary layer to transition to turbulence. Beckwith et al. [24] and Chen et al. [25] studied the effect of Görtler vortices on the boundary layers of supersonic nozzles and how they affect transition. Floryan [26] showed that the Görtler vortex structure can exist in turbulent boundary layers on concave surfaces of turbine-compressor blades. The Görtler instability can also lead to transition via a secondary instability [27][28] or by destabilizing the Tollmien-Schlichting waves [29][30][31].

1.2.6 Pathways to boundary-layer transition

Boundary-layer transition can have significant effects on vehicle design and durability as discussed in Sec. 1.1. Thus it is essential to understand how it occurs and how it can be controlled. The subject has been studied for decades and there is a sizeable subset of the scientific aerospace

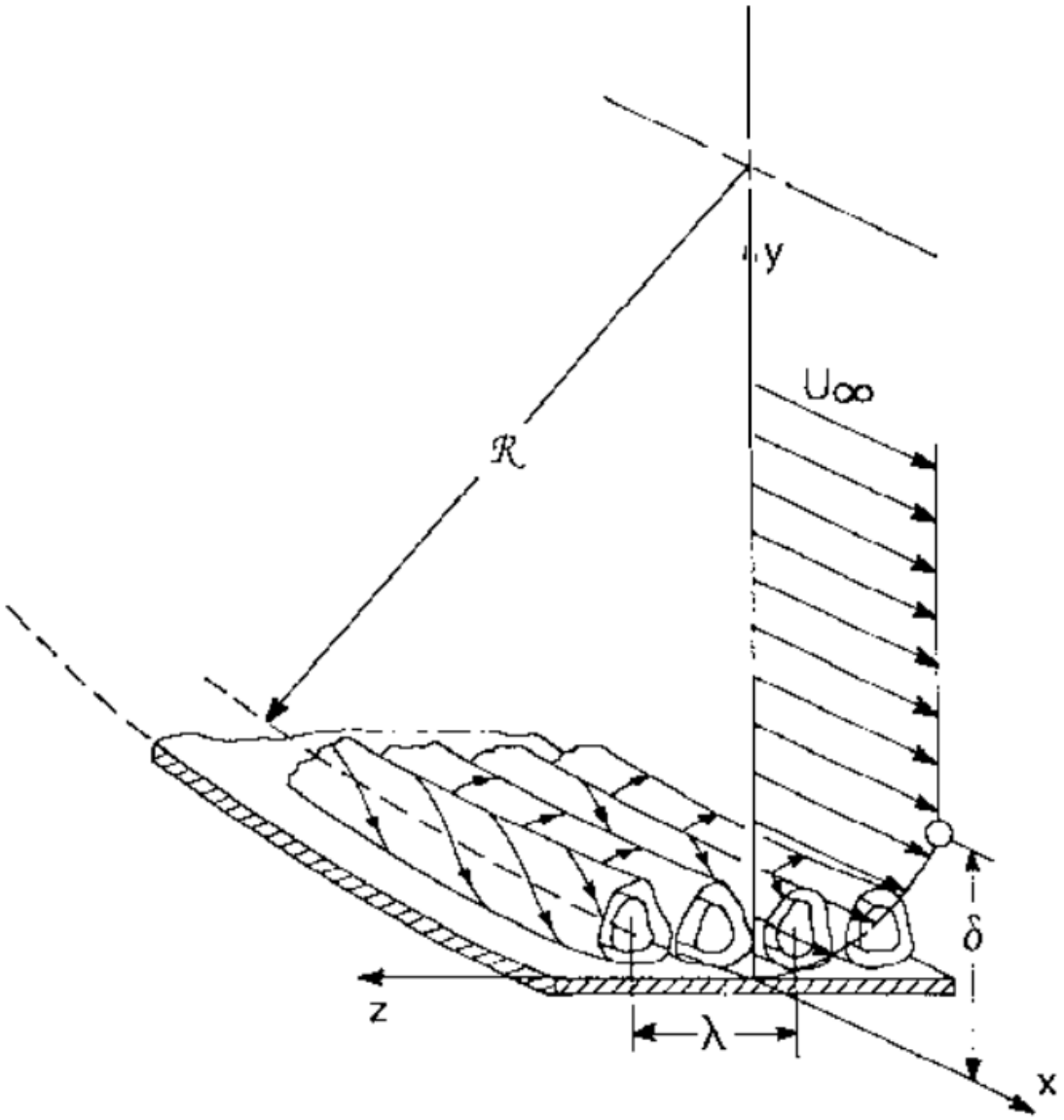

Figure 1.3: The counter-rotating streamwise vortices of the Görtler instability (Reprinted with permission from [3]).

community dedicated to the study of boundary-layer transition, much progress has been made but there remain interactions of the different modes that are not fully understood.

There are several ways a boundary layer can transition from laminar to turbulent, these are called transition modes or pathways. Tollmien-Schlichting (T-S) waves are dominant causes of transition for 2-D flows at subsonic speeds, especially for incompressible flows. T-S waves are

two-dimensional disturbances that grow in a shear layer and grow in amplitude, eventually causing transition of the boundary layer. At supersonic speeds there is a scalar transport of pressure in the spanwise directions and thus three-dimensional oblique disturbances appear and are most dominant. Mack [12] named these dominant disturbances at supersonic speeds the first-mode disturbances. Mack also found that a different disturbance was dominant at hypersonic speeds, at speeds above Mach 4, the first mode becomes less dominant and the "second mode" takes over as the dominant cause of transition. Presently it is more common to use Mack mode instead of second mode [32].

The different modes that lead to transition are separate but do interact with each other, naturally they have been grouped and classified in several ways. The classic transition roadmap is shown in Fig. 1.4. The roadmap has developed over time and the one shown is adapted from Morkovin [33] by Hofferth [2].

Disturbances in the freestream enter the boundary layer as steady and/or unsteady fluctuations of the basic state and this process is called 'receptivity' [34]. In Fig. 1.4, the initial disturbance amplitude increases from left to right. Path A is followed by very weak disturbances and these grow slowly and can be modulated by pressure gradients, temperature gradients, etc. The initial growth of the primary mode and secondary modes can be modeled linearly till they reach an amplitude where nonlinear interactions cannot be ignored [35]. They then experience rapid growth and the boundary layer starts to breakdown, which then leads to turbulence. Paths B, C, and D all have transient growth as part of the breakdown process. Transient growth is when the Tollmien-Schlicting and Squire modes which are nonorthogonal interact and their interaction grows algebraically [36]. This transient growth can then affect the transition process in a few different ways. Smaller amplitude disturbances follow Path B where transient growth amplifies the primary mode in the boundary layer which then follows the same path as path A to turbulence. For larger disturbances the transient growth can bypass primary modes and excite secondary disturbance mechanisms which then lead to breakdown and turbulence, this is path C. Even larger initial disturbances follow path D where the mode interaction grows fast and bypasses both primary and secondary modes to lead

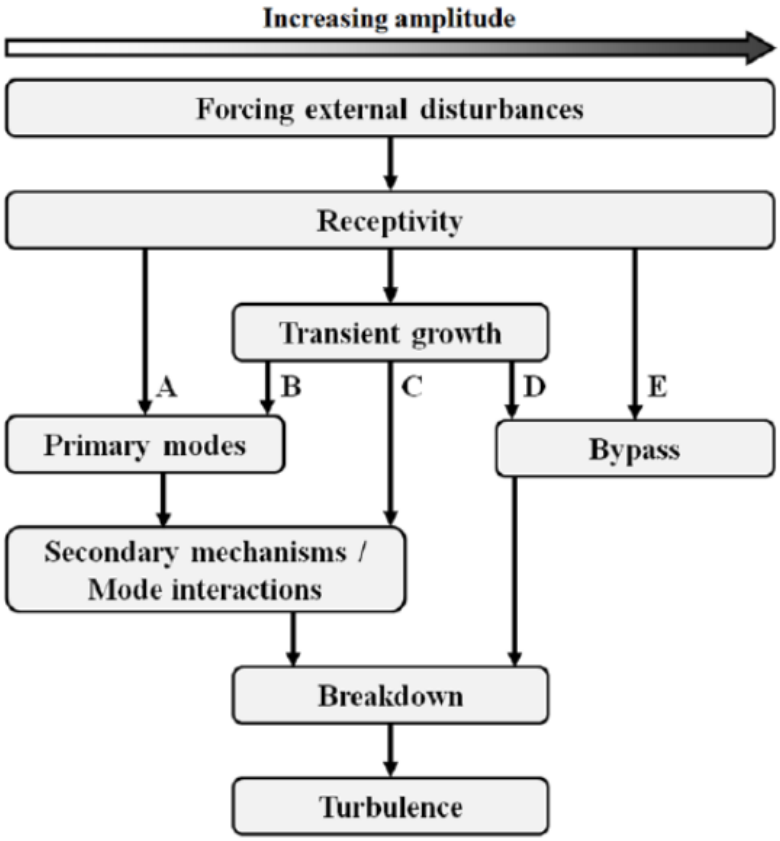

Figure 1.4: Pathways to transition (Reprinted with permission from [2]).

to breakdown. Path E is when the initial amplitude of the disturbance is sufficiently large to cause abrupt breakdown of the boundary layer [37][38].

1.3 Experimental background

1.3.1 Foundational experiments

Schubauer and Skramstad conducted one of the earliest boundary-layer instability experiments about 80 years ago that confirmed the presence of Tollmien-Schlichting waves, which had only been a theory until then [39]. Their experiment motivated several other studies of boundary-layer stability. Most of the early experiments were conducted at subsonic speeds and thus did not focus on the Mack modes. Eventually, hypersonic wind tunnels were built and experiments carried out. Before the discovery of the Mack modes, Demetriades conducted hypersonic boundary-layer

stability experiments on a flat plate [40][41]. Kendall was the first to document the Mack-mode instability in a supersonic boundary layer [42]. Demetriades documented the Mack-mode instability on a sharp 4° cone using hot-wire anemometry [43]. Kendall did experiments on a 5° cone at various Mach numbers between 1.6 and 8.5 and found the Mack-mode instability to be dominant at higher Mach numbers [44]. Demetriades did further experiments with wall cooling and found that lower wall temperatures resulted in higher amplification factors of the Mack-mode and earlier transition [45][46][47]. Stetson et al. did several experiments where several parameters (including wall temperature) were varied and showed good agreement with the predictions of Linear Stability Theory (LST) [48][49][50][51][52][53][54][55][56][57].

All the experiments mentioned previously were done in conventional wind tunnels where the freestream disturbance levels can be an order of magnitude (or more) higher that what is seen in flight due to the turbulent boundary layers on the nozzle walls radiating Mach waves into the flow [58][59]. Mack noticed discrepancies between transition predictions from theory and actual transition locations in experiments and concluded the freestream disturbances may be the cause [60][61]. The transition process is susceptible to receptivity and the higher noise environment can lead to transition much earlier than it would in flight. Schneider has written extensively on the need for "quiet" wind tunnel facilities for stability experiments [62][63]. Several such facilities were developed using various methods to mitigate boundary-layer transition on the nozzle walls to create a low-disturbance flow in the test area. One such facility was the Advanced Mach 6 Pilot Quiet Nozzle Test Chamber (M6NTC), the nozzle of which is used in the M6QT. After reliable operation was achieved, Lachowicz conducted experiments over a straight cone and flared cone with interchangable tips in this facility and showed that the Mack mode was the dominant cause of transition and increasing nosetip bluntness stabilized the boundary layer [64]. Lachowicz et al. studied a flared cone and showed that the amplification factors of the Mack-mode instability were within 5% of the predictions from LST [65]. The same flared cone was used by Doggett at an angle of attack and the Mack mode was observed to be destabilized on the leeward side and stabilized on the windward side [66].

Blanchard and Selby used the 91-6 flared cone with active cooling in the M6NTC to study the effects of higher Mack-mode frequency caused by lower wall temperature and the flare [67]. The N-factors were seen to increase as the wall temperature was decreased and agreed well with the predictions from LST. This same 91-6 model is being used for the current work. Their experiment serves as a baseline for the current experiment. In a way the experiment is being repeated but the difference is the advancement of technology and diagnostics. The original experiment relied on anemometry and thermocouple data. The current work makes use of several new diagnostics that were not available in the earlier experiments. Data acquisition has also come a long way since then and allows for higher resolution and bandwidth of data being collected.

The experiments in the M6NTC have been summarized by Wilkinson, he concluded that the Mack-mode instability dominated transition but the Görtler instability was a contributing factor as well [68]. The M6NTC facility was then shut down along with many others due to lack of funding and put in storage. In 2005, the key components of the M6NTC were moved to the National Aerothermochemistry Laboratory at Texas A&M University and the wind tunnel was resurrected as the Mach 6 Quiet Tunnel.

1.3.2 93-10 cone in M6QT

The 93-10 cone model used by Lachowicz and Doggett was brought to the NAL with the nozzle and other components of the M6NTC. Hofferth studied Mack-mode disturbances on the 93-10 cone in the M6QT [69][2][70]. The 93-10 cone has a 254 mm (10 inch) straight fore section with a 5° half-angle. The straight section is follwed by a 254 mm (10 inch) flared section with a radius of curvature of 2.36 m (93.071 inch) for a total length of 508 mm (20 inch). This model has a detachable tip so the tip radius can be varied. The development of the Mack-mode instability was studied at a unit Reynolds number of 10x10^6 /m using hot-wire anemometry and the focusing schlieren optical diagnostic. The Mack-mode instability was observed at 250 kHz < f_0 <310 kHz and exhibited substantial growth on the aft 20% of the cone. Focused schlieren data showed two additional harmonics of the Mack mode at $2f_0$ and $3f_0$. A bispectral analysis was used to identify the nonlinear interactions responsible for the development of these harmonics [71].

The 93-10 model was used for another testing campaign in the M6QT by Craig [8]. Boundary-layer transition does not occur on the 93-10 cone for the highest possible Reynolds number where the M6QT is still "quiet". Therefore discrete roughness elements were placed on the model to excite the instabilities and cause transition. The DREs used were of heights ranging from 10-30 μm and were not big enough to destabilize the flow.

1.3.3 7DC cone in M6QT

A sharp-tip 7° right-circular cone was designed by Craig to be used in the M6QT to study the crossflow instability [72]. The cone has a sharp detachable tip of length 155 mm (6.1 inch) and the total length is 430 mm (16.92 inch). The model was yawed 5.6° to induce crossflow on the surface. IR thermography was used to visualise the crossflow streaks and detect transition location. Hot-wire anemometry was used to map the mean flow and showed the structure of the crossflow vortices. A traveling crossflow wave was observed in addition to the stationary crossflow wave in a frequency band centered around 35 kHz. The boundary layer was not observed to transition and so distributed roughness was added to the tip. This caused the boundary layer to transition but not by exciting the crossflow instability, it appeared to be a different instability mechanism.

1.4 Research Objectives

The objective of this experiment is to better understand the transition process and how the Mack-mode disturbances lead to transitional flow. The boundary layer can be resolved using several diagnostics, to include hot film anemometry, focusing schlieren, and Focused Laser Differential Interferometry (FLDI). The Mack-mode disturbances were characterized and the effect of cooling the model studied by doing both cooled and uncooled testing. This being a previously studied case the new research adds to the understanding of how transition takes place on this geometry.

Sivasubramaniam and Fasel [73] studied nonlinear transition mechanisms of a boundary layer on a sharp cone at Mach 6 using Direct Numerical Simulations (DNS). Their computations were done to match the conditions in the quiet-flow Ludwieg tube at Purdue University which are

very similar to the flow parameters in the M6QT. Their computations show interaction between the streamwise Mack-mode (fundamental) and oblique modes in the form of a fundamental (or Klebanoff-type) resonance. These interactions result in azimuthal periodic modulation in the form of λ-vortex structures and streamwise streaks. The computations also showed evidence of the presence of an oblique breakdown mechanism in the non-linear transition regime. This would be a hypersonic equivalent of the experiments done by Klebanoff [74] to demonstrate the 3-D nature of breakdown of Tollmien-Schlicting waves in subsonic flow on a flat plate. The purpose of this experiment will be to closely match the computations and study the similarities and differences in results and explain them. The Mack-mode and Görtler vortices are present on the 91-6 flared cone and their interaction may result in an oblique breakdown similar to the Klebanoff study.

This experiment also aims to develop diagnostics. Diagnostics with higher resolution and bandwidth can be the difference between repeating old experiments and making new discoveries. The focusing schlieren diagnostic was in place at the NAL but was improved for this work. The Focused Laser Differential Interferometry (FLDI) technique is relatively new and has the potential to make multi-point non-intrusive measurements in the boundary layer when implemented in the M6QT [75].

The data collected for this work are also meant to serve as code-validation data for computational work. The documentation of conditions in the wind tunnel can serve as initial conditions for Parabolized Stability Equations (PSE) solvers. The initial conditions can have a large effect on the results of computations and thus it is important to have the right inputs. When the CFD solvers can show that the results match closely what is seen from experiments, they can then be used for flow conditions that may not be achievable in the wind tunnel and the results are more credible.

2. EXPERIMENTAL SETUP*

2.1 Facility

2.1.1 Wind tunnel

The Mach 6 Quiet Tunnel (M6QT) facility is installed at the TAMU National Aerothermochemistry and Hypersonics Laboratory where it shares pressure-vacuum infrastructure with several additional supersonic and hypersonic facilities. High pressure air is provided by a pair of CompAir 5442 (Fig. 2.1), each with a pumping capacity of 3.68 m^3/min. (130 SCFM) at 20.68 MPa (3000 psig). The compressed air is filtered with a pair of 99% efficient sub-micron particle filters and dried to a dew point of -40 °C by a twin-tower desiccant drier before being stored in a 23.2 m^3 (820 ft^3) tank at 17.24 MPa (2500 psig). The vacuum for the pressure-vacuum tunnels is generated using a two-stage Venturi air ejector (Fig. 2.2). This system uses approximately 20 kg/s of compressed air at 1033 kPa while in operation and is capable of supplying a back pressure of as low as approximately 500 Pa to the wind tunnels. This high mass-flow requirement is the dominant factor in determining the tunnel run time. The same compressed air reservoir supplies air for the tunnels. Prior to reaching the settling chamber, the air is heated by a 500 kW Chromalox electrical-resistance heater to achieve the desired total temperature (usually 430 K, maximum 533 K) and re-filtered using a 1 micron particle filter immediately prior to entering the tunnel. While in operation, the M6QT draws approximately 1 kg/s of compressed air through the test section. The air requirements of the ejector and nozzle combined result in a maximum runtime of approximately 40 seconds [8].

A conventional wind tunnel at hypersonic speeds often has a freestream environment with disturbances an order of magnitude higher than those observed in flight [62]. These disturbances can alter the growth of instability and possibly change the pathway to transition [76]. These disturbances come from the boundary layer on the nozzle wall transitioning and radiating noise into the

*Parts of this chapter are reprinted with permission from [2][4][5][6].

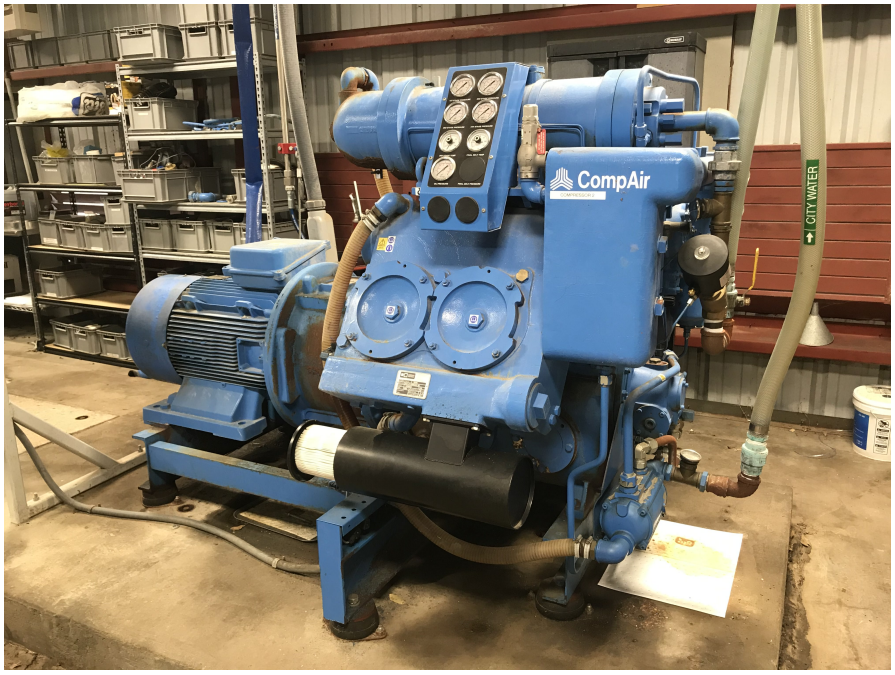

Figure 2.1: One of the two (soon to be three) CompAir 5442 compressors.

Figure 2.2: The two-stage Venturi air ejector that provides a vaccuum on the downstream end of the blowdown wind tunnels.

freestream thus making the flow "noisy" [77][58][78]. The difference between a conventional and quiet wind tunnel is visualized in Fig. 2.3. Much research was done at NASA Langley Research Center and the Advanced Mach 6 Pilot Quiet Nozzle in the Nozzle Test Chamber (M6NTC) was made which is the nozzle used in the M6QT [79]. The tunnel uses a long settling chamber with flow smoothing meshes to mitigate uneven flow coming into the nozzle. The nozzle has bleed slots that remove the boundary layer at the nozzle throat and a fresh boundary layer is formed as the flow travels down the nozzle which helps delay transition. The nozzle is a highly polished surface to mitigate roughness-induced transition. It is also a long expansion nozzle to delay the effects of the Görtler instability. All these steps result in quiet flow up to a unit Reynolds number of $10.7 \text{x} 10^6$/m. The freestream pressure fluctuations in the nozzle are 0.05% RMS along the centerline and gradually increase to 0.5% RMS at the nozzle exit [2].

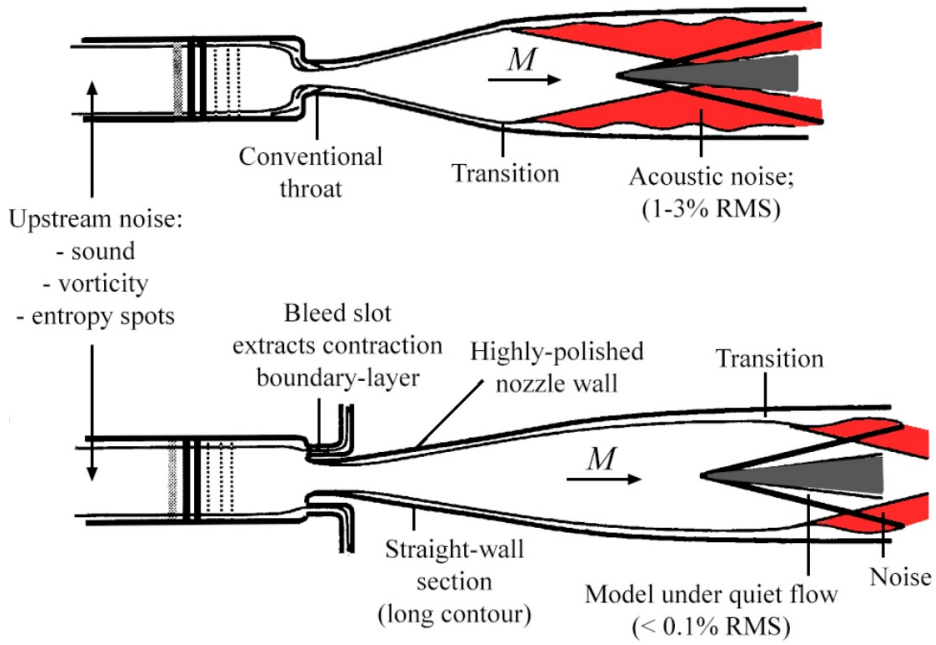

Figure 2.3: Schematic showing the general differences between conventional and quiet wind tunnels (Reprinted with permission from [2]).

The test section for the M6QT is an enclosed free-jet test section. The test section has an

interior height and width of 0.81 m and contains the nozzle and diffuser bell mouth. The test section has room for any instrumentation and/or model mounting apparatus required. The test section also has doors on four sides and the doors have 8-inch windows providing optical access to the test area.

2.1.2 Traverse

The M6QT had utilized a probe traversing mechanism that worked in 2-D Cartesian coordinates and this was utilized extensively by Jerrod Hofferth [2] after the tunnel was installed and operational at the National Aerothermochemistry Laboratory (NAL) at Texas A&M University. The traverse was a commercial unit from Aerotech Inc. and provided 400 mm of travel in the axial direction and 200 mm of travel laterally. This traverse was used to characterize the freestream of the wind tunnel and worked well but was not ideal due to the axisymmetric nozzle and models that were to be studied.

A new 3-D traverse was designed and built by Alex Craig [8] to make 3-D measurements and a cylindrical (r, θ,and z) coordinate system was chosen to better fit the axisymmetric nozzle and cone-shaped models that were to be studied. This traverse consists of a carriage with axial and radial motion stages moving on a ring using a rack-and-pinion gear system. The r and θ axes are in the plane parallel to the nozzle exit plane and the z-axis is streamwise, as seen in Fig. 2.4. Each axis has a specific range, minimum step size, and associated accuracy, these are summarized in Table 2.1.

Table 2.1: Specifications of the azimuthal traverse system [8].

Axis	**Range**	**Min. step**	**Accuracy**
r	100 mm (max.)	2.5 μm	$\pm$1.22 μm
θ	220°	3°x10^{-4}	$\pm$3°x10^{-4}
z	130 mm	2.5 μm	$\pm$1.22 μm

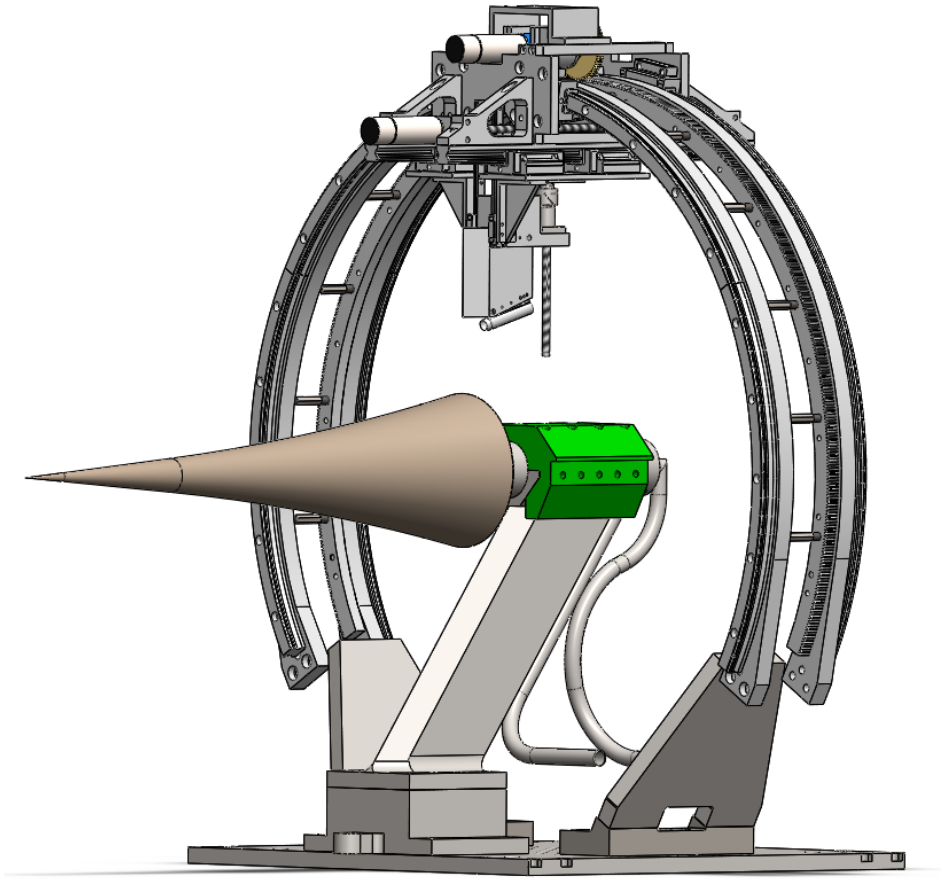

Figure 2.4: The 3-D traverse mechanism, shown here with the 91-6 cone model.

2.2 Model

2.2.1 91-6 cone

The model used is the 91-6 cone originally made by NASA. The model has a sharp detachable tip with a radius of 63.5 μm (0.0025 in) and length 38.1 mm (1.5 in). The first 152.5 mm (6 in) of the model is straight with a 5º half-angle. After the straight section the model has a constant flare of radius 2322.7 mm (91.44 in) for 12 in. The total length of the model is 457.2 mm (18 in). The model is named the 91-6 cone for the 91.44 in flare and 6 in straight section, consistent with the naming of other similar models, such as the 93-10 cone [71]. The model has a 2.032 mm (0.08 in) thick Ni shell. On the inside is a coolant inlet that runs in the streamwise direction to just downstream of where the tip screws in. The coolant then travels between the coolant inlet passage

and the model shell to the aft end of the cone where it goes out an exit. The coolant is continuously circulated by a recirculating chiller outside of the test section. Fig. 2.5 shows a diagram of the cone. The original documentation with structural calculations and drawings used to manufacture the cone are available and more details are in Appendix A.

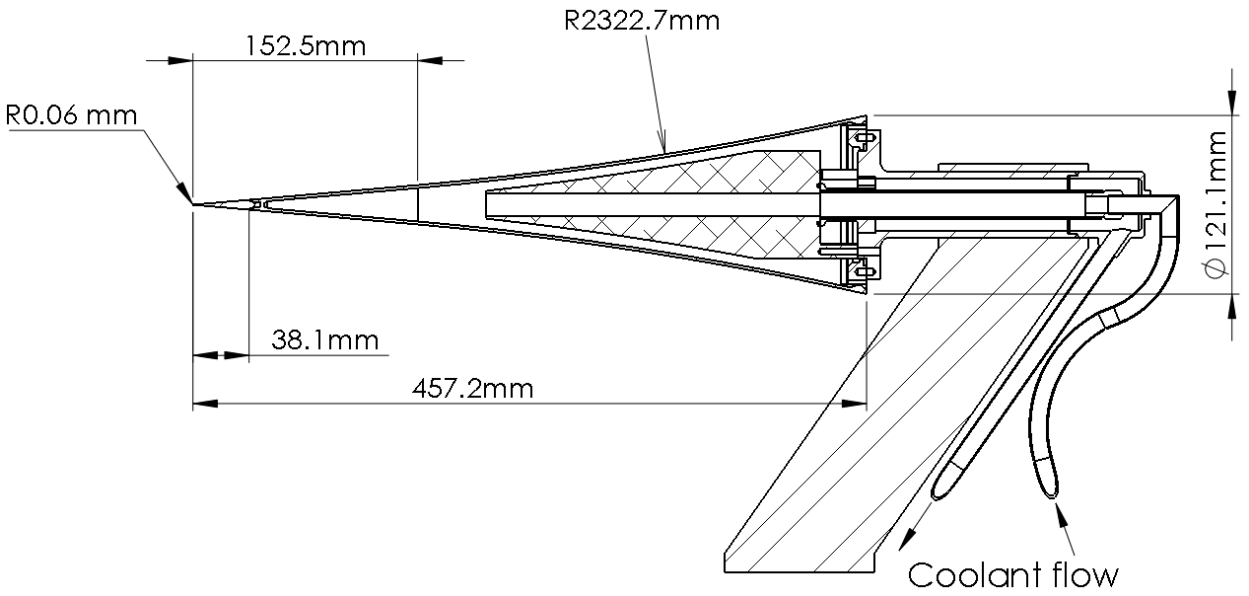

Figure 2.5: Diagram of the 91-6 cooled flared cone.

Model installation and extraction is a delicate task in the M6QT due to the lack of space between the nozzle and diffuser. The highly-polished nozzle is fragile and can be easily damaged by a model, this can happen if care is not taken as most models are placed partially inside the nozzle. Instrumentation attached to the model makes this task even more cumbersome, and the 91-6 cone adds coolant tubing to the mix. Hofferth wrote a guide to installing and extracting models in the M6QT named, "Procedures & Guidelines for Model Installation & Extraction". This guide is part of the "Facility Configuration & Model Change Log" which is stored in the control room of the NAL with the rest of the M6QT documentation. It is recommended that the guide be consulted every time a model is installed or extracted and the condition of the nozzle documented in the log before and after every procedure. A special plate was designed for the coolant to flow in and out

of the test section with steel tubing connections to the chiller and braided hoses to the cone so the model could be moved on the rails in the test section. Also included in the plate is an opening for the thermocouples and control wiring for the traverse to come out of the test section. The wires would be passed through, taped up, and RTV UHT silicone sealant used to seal the opening.

This cone was one of several models used in the M6NTC at NASA Langley to study hypersonic boundary-layer stability. This cone specifically studied the effect of wall cooling on the boundary-layer stability. Linear Stability Theory (LST) suggests the Mack-mode frequency increases with wall cooling. Mack observed that the first linear-instability mode was stabilized by wall cooling and the Mack-mode was destabilized. The boundary layer shrinks due to the density increase as temperature decreases. Mack-mode disturbances are acoustic waves that travel between the surface and the relative sonic line. As the temperature decreases the local speed of sound decreases thus increasing the local Mach number which increases the frequency of Mack-mode disturbances. Blanchard and Selby [67] carried out the experiment in the M6NTC with the 91-6 cooled cone. The linear growth of Mack-mode disturbances, saturation and breakdown into developing turbulent flow was studied. That experiment serves as background for the current experiments. The data recorded were checked against the previous data to verify and give a starting point for experiments. Wilkinson [68] reviewed three separate experiments carried out in the M6NTC at NASA Langley to study low freestream disturbance stability. The cooled 91-6 cone was one of these studies. The conclusion was that the Mack mode dominated transition.

2.2.2 Chiller

The cone and chiller had been in storage for a few years after NASA stopped using them, they were then loaned to Purdue University for testing but not used there. They were then sent to the NAL at Texas A&M University to be used in the M6QT. The chiller is a FTS Sytems Inc. RC211 model. Initially the chiller was tested to ensure it operated as expected. After getting it running coolant pressures were tested and compared to specifications in the manual and the chiller was confirmed to be operating as designed. The chiller works as a cascade refrigeration system with two loops to remove heat from the coolant, the high temperature loop is in contact with the

coolant and then the high temperature loop is cooled by the low temperature loop. Since the chiller was over two decades old the refrigerants used were not available and the decision was made to not check refrigeration pressures as it would entail the risk of losing refrigerant that may not be available to refill with. Instead some tests were done with ethanol as the coolant to observe how fast and to what temperature the chiller could do, the results were good with the coolant quickly dropping in temperature to -60 °C. Ethanol was decided on as the coolant of choice after careful deliberation. The manual for the chiller lists suggested coolants and their maximum and minimum temperatures, obviously the lowest possible minimum temperature was desired but the maximum temperature needed to be high enough in case the chiller failed for any reason and the hot air in the wind tunnel heated the coolant in the cone. Of the easily available coolants, ethanol fit the requirements best and was used for all the tests thereafter. There are also specialty coolants that are designed for such applications; they cool better, are less likely to leak and have higher maximum temperatures and lower minimum temperatures than the easily available coolants. One such coolant is Fluorinert FC-72 by 3M and a sealed 5-gallon container of it is available at the NAL as of this writing, it is recommended for future work to use this coolant. It was not used for the current work since ethanol was used from the beginning and maintaining consistency between all data collected was deemed more important than any potential gains in cooling.

2.2.3 Distributed Roughness Elements (DREs)

Initial data showed a periodic variation in the mass flux, this was confirmed using CFD work showing that these variations may be caused by Görtler vortices. Spatially-periodic Distributed Roughness Elements (DREs) were used to enhance and regulate the 3-D modulations of the boundary layer and study how they interact with the flow characteristics that are present to begin with. Their application had nothing to do with laminarisation which is what DREs have traditionally been used for.

The challenge was to put on small and precise DREs without hurting the expensive and delicate model. Since this is a cooled model and has a cavity for coolant under the surface, machined roughness elements were not an option. DREs had to be applicable to the surface. Previously,

water-slide decals were used but even with multiple layers there was no appreciable effect on the boundary layer, this was chalked up to the height of DREs ($\sim$ 10 μm) being insufficient. Most conventional ways of making decals were not precise enough and the water slide decals were not thick enough. A new method was devised to place DREs on the cone. The DREs were made by laser cutting them out of a strip of Kapton tape with thickness 0.051 mm (0.002 inch) that was adhered on to a Mylar sheet of thickness 0.178 mm (0.007 inch), the objective was to cut through the Kapton but not the Mylar, this precision laser cutting was done by A-Laser, a division of FCT Assembly, in Milpitas, CA. The strip of DREs was cut to a suitable size for application to the model and then high-viscosity super glue applied to the strip. The tape was quickly pulled off the Mylar sheet leaving the DREs in place with adhesive on them and the Mylar was very carefully applied to the model at the desired location and then pulled off leaving the DREs on the model. The placement of the DREs was decided by finding the neutral line from computations which is where the flare of the cone starts, at 152.4 mm from the tip. The DREs were placed at a wavenumber of 90 to interact with the observed fluctuation in mass flux at that wavenumber. A laser profilometer was used on flat plates and the blockage model to obtain the height and diameter of the DREs. They are 81$\pm$3.6 μm in height and the diameter and spacing are equal at 465$\pm$7.6 μm. Data were collected again after putting DREs on the model to compare with the results seen on the smooth cone. The DREs applied to the 91-6 cone can be seen in Fig. 2.6.

The exact process used to apply the DREs is outlined below. This process was refined over several applications on the blockage model. It is recommended to always practice on blockage models till the process is consistently working before application to the original delicate model.

1. Cut DRE strip from Mylar sheet.

2. Soak in Acetone bath for 1 hour, this made the DREs come off the Mylar sheet better when applying to the model.

3. Remove from Acetone and let dry.

4. Remove tape off 12 mm on one side for clamp and 12 mm off other side for fingers to hold

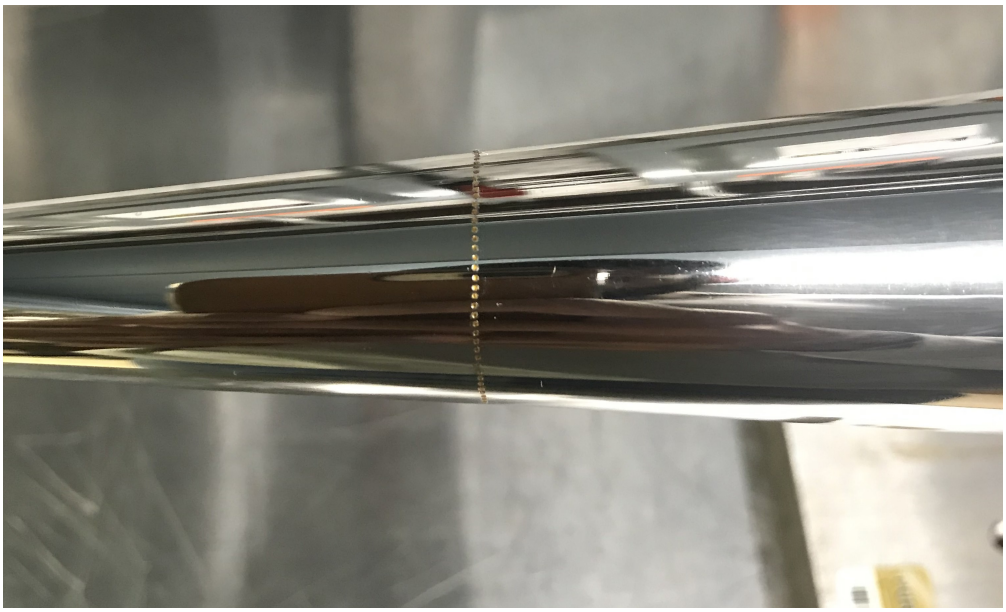

Figure 2.6: DREs on the 91-6 cone.

when peeling.

5. Clamp strip to table.

6. Apply adhesive (thick super glue) to strip making sure all DREs are covered.

7. Quickly, holding strip down on the end opposite the clamp, remove the tape in one fluid motion. DREs should stay on the Mylar strip.

8. Quickly, apply strip to the model, holding tight for 10 seconds.

9. Remove strip and hope all DREs are on the model and aligned as desired.

2.3 Diagnostics

2.3.1 Instrumentation

The cone itself has embedded instrumentation that provides data during a run. The cone has 51 type-T thermocouples that are on the port side of the model along a streamwise line. There are 30 pressure ports on the starboard side also along a streamwise line. The thermocouples were used to

track temperatures along the cone, since the model and tunnel are axisymmetric the temperature can be assumed to be the same all around the cone at the streamwise point where the thermocouple is reading data. The pressure ports were not used. The type-T thermocouples were guided out of the tunnel through a hole in a base plate that was machined specifically for these experiments, the plate also had the coolant inlet and outlet hoses running through it. The hole had a pipe nipple threaded through it so the wires could be taped together and then high-temperature RTV silicone used to seal the gap between the taped wires and the inside of the pipe nipple. Each thermocouple has two wires so there is a total of 102 wires, the two wires of each thermocouple are taped together and numbered, it is essential for these tags to stay on and they must be replaced if they come off as this keeps track of the streamwise location of the thermocouple on the model. The thermocouples are wired into two National Instruments SCXI-1303 32-channel isothermal terminal blocks. The blocks are plugged into a National Instruments SCXI-1001 chassis which can hold 12 such modules and provides a low-noise environment for signal conditioning, supplying power, and control circuitry for the modules. The chassis and modules are located underneath the M6QT test section as of this writing. The chassis also transmits data to a data acquisition (DAQ) card in the computer with the LabView program that collects data during experiments.

2.3.2 Constant Temperature Anemometry

Hot-wire anemometry originally developed as a technique to measure flow velocities. A standard sensor consists of two probes with a thin wire stretched between them. The wire is usually made of tungsten, platinum, or platinum-alloy. The general mode of operation of an anemometer is for the wire to be heated by an electric current and when placed in fluid flow the wire is convectively cooled, there are several ways to then obtain flow properties. Using a sufficiently small wire (5-10 μm diameter) and a high-frequency feedback circuit the wire can be used to provide data with a frequency response on the order of 10^5 Hz. Anemometry can be implemented by holding constant the temperature, voltage or current. Constant Voltage Anemometry (CVA) and Constant Current Anemometry (CCA) utilize open-loop amplifiers and this complicates the process for boundary layer studies, Constant Temperature Anemometry (CTA) on the other hand

uses a closed-loop feedback circuit which is preferable. Kegerise and Spina [80][81] did a detailed analysis of the static and dynamic responses of the three different systems and is a good resource for anyone deciding what kind of system to choose for a certain experiment. The wire can be placed normal to the flow to get streamwise measurements or it can be angled for transverse velocity measurements.

2.3.2.1 Theory

Constant Temperature Anemometry (CTA) is used with hot films for the present work, the thermal resistance of the film and convective heat transfer from the flow over it is used to measure flow properties. The films provide a spatial resolution of $\sim$0.1 mm and frequency response of $\sim$100 kHz. The film is heated by applying a voltage to it by the CTA system. Air flowing over the wire convectively cools it and the voltage required to maintain the set operating resistance increases. The heat transfer relationship in a general compressible flow is given by the Nusselt number,

$$Nu = f(Re_d, Pr, M, \tau, l/d) \tag{2.1}$$

where *Nu* is the Nusselt number, Re_d is the sensor diameter Reynolds number, *Pr* is the Prandtl number, *M* is the Mach number, $\tau = (T_w - \eta T_t)/T_t$ is the temperature loading factor[82], T_w is the operating temperature, T_t is the total temperature, $\eta = T_e/T_t$ is the recovery factor, and T_e is the film's equilibrium (or recovery) temperature. For supersonic flows the dependence on Mach number is negligible [82]. For large *l/d* and assuming constant Prandtl number,

$$Nu = f(\rho U, T_t, \tau) \tag{2.2}$$

Smits et al. [83] showed that for sufficiently high τ the response is dependent solely on ρU and dependence on T_t becomes negligible. Thus, the hot-film measurements in the form of fluctuating anemometer voltages can be seen as fluctuating mass-flux measurements. Mean and dynamic mass-flux measurements can be made using hot films and the boundary layer resolved. Hot films are being used to acquire well-resolved mean flow and instability profiles.

2.3.2.2 Hardware

The anemometer used is a A.A. Lab Systems AN-1003 hot-wire anemometry system, as shown in Fig. 2.7. The AN-1003 is a manual system with 10 analog channels that can be used simultaneously. Each channel has a built-in signal conditioner, filter, and a probe-protection circuit, making it suitable for very small and delicate wires. The system is completely manual with no computer controls which reduces the noise in the data collected. The probe used is a TSI 1220 model, a high-temperature straight probe. The probe attaches to a TSI 1150 standard probe support which outputs to a BNC cable. The 1220 probe can be ordered with different wires and films attached to it. Originally wires were used to achieve higher frequencies when analyzing spectral data, the -PI2.5 was used which is a platinum-iridium alloy with a thickness of 6.3 μm (0.00025 inch). The probes with wires worked well at first but eventually after a few tunnel runs the forces of tunnel start and unstart caused them to break even though efforts were made to hide the wire outside of the flow. After repairing quite a few wires the decision was made to switch to hot films as the highest frequency attainable with the wires was ∼250 kHz and the Mack-mode instability was expected to be higher than that. Films were used as a tool to quantify the mass flux in the boundary layer instead. The film used was the -20 available from TSI which is still a sensor between two prongs as opposed to a traditional film that is adhered to a surface and uses the same TSI 1220 probe and TSI 1150 probe support. The diameter of the -20 film is 50.8 μm (0.002 inch) and this results in the highest detectable frequency being ∼100 kHz. The films proved durable (not one film broke during tunnel runs), and fulfilled their purpose of collecting data that could be approximated to be mass flux in the boundary layer.

2.3.2.3 Operating procedure

All wind-tunnel runs with anemometry data collection were done with a very specific procedure designed to extend the life of the hot wires/films. The wire was in idle mode and hidden outside of the nozzle during preheat and before the tunnel run. When the tunnel started and hypersonic flow was established the anemometer operator would quickly initiate the preprogrammed traverse

Figure 2.7: A.A. Lab Systems Inc. AN-1003 anemometer.

motion sequence and activate the sensor. This way the sensor was inactive going through the nozzle shear layer and would only turn on in the low density hypersonic flow. The operator would then watch for the end of the data acquisition on the LabView VI and deactivate the sensor before it moved back to its hiding place outside the nozzle. The tunnel operator was then given a signal by the anemometer operator indicating that the sensor was safe and the tunnel operator would then shut the ejector off, thus ending the hypersonic run. This procedure prolonged the life of the hot wires and hot films considerably. For future experiments it may be easier to hide the sensor behind the model but that was not possible for these experiments owing to the myriad of wires and tubes that exit the cone. It would also be beneficial to design model-and-sting interfaces in such a way that there is a hiding space for the sensor if possible. The hot-film probe and cone model are shown in Fig. 2.8.

The very first time a sensor is used it has to be tuned for the flow in the wind tunnel. The manual for the AN-1003 anemometer has a detailed explanation of how to tune the wire and should be followed, it involves monitoring the response to a square wave and adjusting damping and ferric

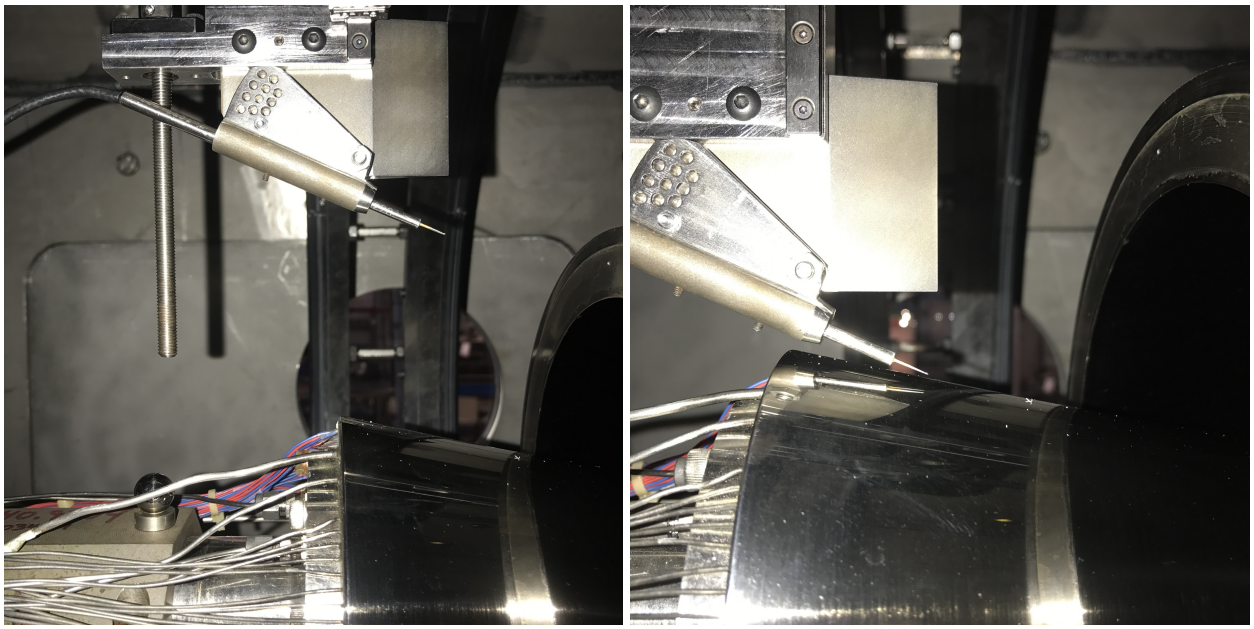

Figure 2.8: Hot film probe over the 91-6 cone. The model has been pulled out of the nozzle for these pictures.

screws. Since a tunnel run only affords about 30 seconds to tune the sensor it was tuned to a "safe" level in quiescent air first and then fine tuned during a dedicated tunnel run. The anemometer settings were then left untouched till the sensor broke or the campaign ended. This process was repeated every time a new sensor was used. The overheat ratio was set to be 0.6, this means the temperature would be 1.6 times the tunnel stagnation temperature, as this was just under the maximum temperature the film was rated for. The data were acquired at three channels:

1. The amplified output from the anemometer low-pass filtered at 200 kHz by an 8-pole Bessel filter element in a Krohn-Hite chassis.

2. The output from 1 was AC coupled, filtered (300 Hz - 300 kHz), and gained (x5) by a Stanford Research Systems SR560 low-noise preamplifier and filter.

3. The raw bridge voltage output from the anemometer.

The BNC outputs for each channel were sent to a NI USB-6366 DAQ system which has 8 channels capable of sampling at 2 MHz. The DAQ interfaces with a DAQ card installed in a

computer which enables a LabView VI to read the data and saves it as a file to be processed in MATLAB.

2.3.3 Focusing Schlieren

2.3.3.1 Background

Schlieren diagnostics have been used for aerodynamic studies for a very long time. Schlieren enables users to visualize density gradients in flow as light and dark areas. It works by cutting off light rays bent by the changes in refractive index in a certain direction and letting through the light rays bent in the opposite direction. A classical schlieren system is simple but picks up any changes in the flow field in the path of light. This can include disturbances outside of the tunnel and in case of a free-jet test section, as is the case for the M6QT, shear layers exiting the nozzle. These can serve to blur details that may be present. Focusing schlieren is a more complex variant, the system is only sensitive in a narrow plane of interest and this eliminates the integration of flow field. There are several ways that this can be achieved but the system used is a lens and grid type focusing schlieren system.

2.3.3.2 Design and Hardware

Weinstein [84] was used as a guide when designing the focusing schlieren system. The initial design of the system was done by J. Hofferth *et al.* [4] and further design details can be found in Craig *et al.* [71]. Fig. 2.9 shows the schematic of the focusing schlieren setup and Fig. 2.10 shows the components setup around the M6QT. The constant light source is a Bridgelux C8000LM with an array of LEDs totaling 8000 lumens mounted to a heat sink and with a reflector to point light towards the Fresnel lens. The light source was driven by 2.2 A current at 36 V using a 80W Extech Instruments (M/N: 382260) DC power supply. A diffuser was added after the light source for the present work to homogenize the light as previously faint details of the array of LEDs could be seen all along the path. The light then travels through a Fresnel lens of diameter 317 mm and focal length 213 mm, the Fresnel lens improves the image brightness as found by Boedeker [85]. Classically source and cutoff grids were made from photographic film with one of them being the

negative of the other but for this system originally the grids were made by printing on transparency film. This worked to some extent but the image quality was not ideal, attempts were made to stack multiple printed source grids on top of each other and this helped increase opacity of the grids but reduced the image quality due to the stacked grids not being perfectly aligned. The cutoff grid was too fine to stack and was left as a single layer. A new method of producing grids was used for the present work. FineLine Imaging in Colorado Springs, CO is a company that specializes in laser photoplot films and photomasks. They were commissioned to "print" the source and cutoff grids with a laser plotter on PET substrate. The optical density achieved using this method averaged $\sim$4.5 (0.00316% transmission) for the opaque areas and less than 0.05 (>90% transmission) for the clear areas. The resolution was 10k dpi which made for much sharper lines than the transparencies previously used. The new grids made for much sharper images and improved the quality of the diagnostic. The lens used is a three-element achromat with a diameter of 155 mm and focal length of 195 mm.

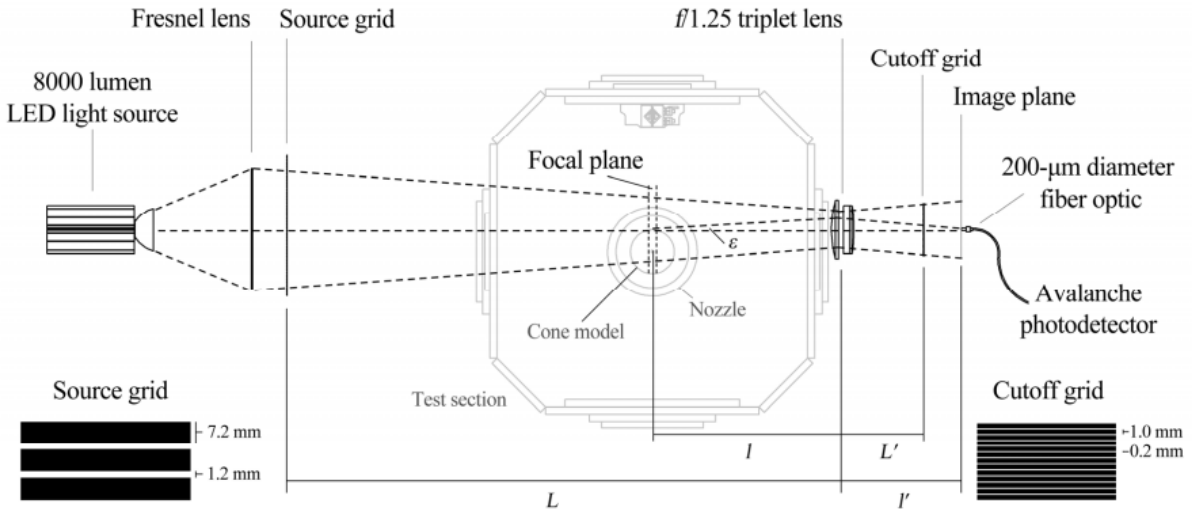

Figure 2.9: Schematic of the lens-and-grid type focusing schlieren system used in the present study (Reprinted with permission from [4]).

The system was designed specifically for the M6QT with special consideration for the width

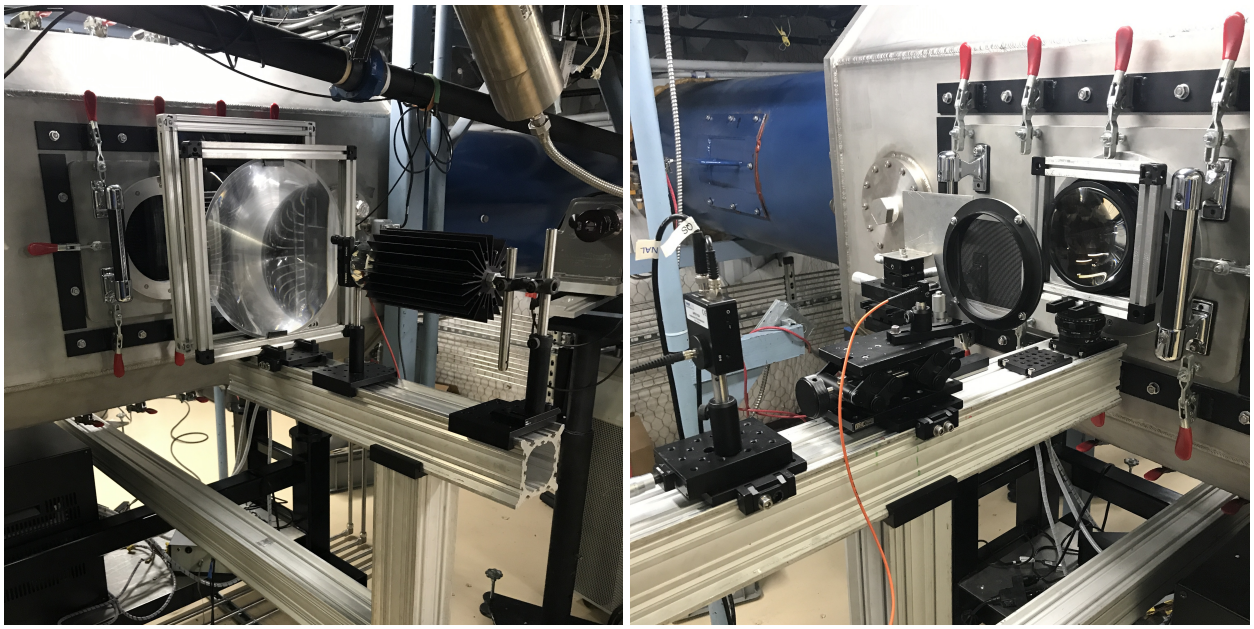

(a) Light source side (b) Detector side

Figure 2.10: The focusing schlieren system setup on the M6QT with the fiber optic and photodetector.

Table 2.2: Specifications of the focusing schlieren system [2].

Parameter	Description	Value
A	Lens aperture diameter	155 mm
f	Lens focal length	195 mm
L	Distance from lens to source grid	1444 mm
L'	Distance from lens to cutoff grid	221 mm
l	Distance from lens to object plane	530 mm
l'	Distance from lens to image plane	308 mm
DS	Depth of sharp focus	0.97 mm
DU	Depth of unsharp focus (for 3 mm structure)	21 mm

of the test section and to keep the depth of focus inside of the nozzle shear layers. The distances between components are marked in Fig. 2.9 and listed in Table 2.2. The depth of focus definition as stated in Weinstein [84] is

$$DS = 2\frac{l}{A}w \tag{2.3}$$

where l is the distance from the lens to the object plane, A is the lens aperture diameter, and w is the resolution limit of the image (calculated from image magnification and grid sizing). The length scale w can be replaced by the wavelength of the Mack-mode instability ($\sim$ 3 mm) to obtain the depth of unsharp focus as

$$DU = 6\frac{l}{A} \tag{2.4}$$

2.3.3.3 Implementation

This system was used to study Mack-mode disturbances on the 93-10 cone [2]. It was revived for the current work to be used as a flow visualisation tool at first. A Photron FASTCAM SA-Z high speed camera was placed at the image plane to visualise flow features. The camera settings were set to 1500 fps with a 0.16 μs shutter, the shutter time is the shortest the camera is capable of and the frame rate was set so the camera memory wouldn't run out over the course of a wind tunnel run. It is possible to increase the frame rate but the time acquired gets shorter and high frame rates were not required for simple flow visualisation. The camera was placed such that the field of view was on the aft end of the model that is not in the nozzle.

Eventually the camera was replaced with a small-aperture (200 μm) fiber optic cable (Thor Labs M38L01) to make measurements at a point in the boundary layer and to analyze the spectral content. The fiber optic cable was connected to an avalanche photodetector (Thor Labs APD110A) with a bandwidth of 50 MHz. The signal from the photodetector was bandpass filtered from 1 kHz to 1 MHz and amplified by a factor of 50 by a Stanford Research Systems SR560 signal conditioner. The data were sampled at 2 MHz as this is the upper limit of the DAQ system. Welch's method was used to extract spectral data from the high-frequency voltage measurements.

The camera and fiber optic were both placed on translation stages so the focal point could be adjusted. Note that the focal plane moves as the image plane moves, this is very helpful on a flat plate model as measurements can be taken at any point on the plate. This system was used on a wedge model in the ACE tunnel by Leidy [86] where the camera was moved during a tunnel run

to study interaction between a shock wave and the boundary layer. For a cone model, as is the case for this experiment, the focal plane simply has to be placed at the center of the model/nozzle. This was achieved by placing a plastic bolt on the model as shown in Fig. 2.11 and moving the camera/fiber optic till the threads of the bolt came into sharp focus, this method is generally used to focus regular schlieren systems as well.

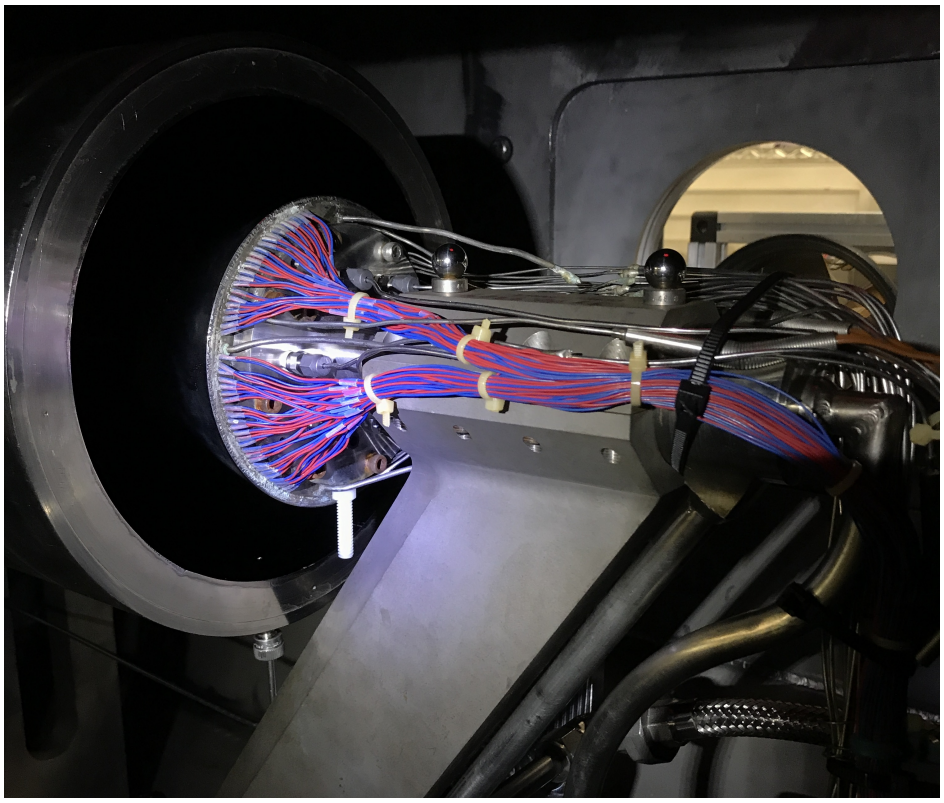

Figure 2.11: 91-6 cone with plastic bolt attached to underside to set imaging plane of focusing schlieren system in the region of interest.

2.3.4 Focused Laser Differential Interferometry

2.3.4.1 Background

Laser Differential Interferometry (LDI) was pioneered by Smeets and George [87][88][89][90] in the 1970's. Their system went through several iterations and was sensitive in changes to optical

path lengths that are related to changes in density of the flow. Density profiles of laminar and turbulent boundary layers were created using this technique [90]. Laderman and Demetriades [91] used LDI to detect boundary-layer transition in supersonic flow by looking at the RMS fluctuations in the boundary layer and equating an increase in fluctuations to transition. Azzazy *et al.* [92][93] used LDI as a transition-detection tool at transonic and supersonic speeds with some success. LDI was compared to other methods of transition detection in Tunnel B at Arnold Engineering Development Center (AEDC) in a hypersonic (Mach 8) boundary layer and showed good agreement [94]. They were able to obtain spectral data and observed content that could be the Mack-mode instability, though the frequencies were lower ($\sim$150 kHz) owing to the thickness of the boundary layer. LDI is a path-integrated measurement and thus includes all fluctuations in the path of the laser including any boundary layers over tunnel windows or shear layers coming off nozzles. This results in a low signal-to-noise ratio (SNR).

Building on the work done by Smeets [95], Parziale *et al.* [96] developed a focusing variant of LDI, aptly naming it Focused Laser Differential Interferometry (FLDI). FLDI does not integrate over the entire path but instead is sensitive only in the region around the focal point, which results in much higher SNR than regular LDI. Parziale *et al.* used FLDI to measure freestream disturbance levels [97] and the Mack-mode instability [98]. Hameed *et al.* [99] used several Wollaston prisms to split the laser beam several times to create four beam pairs at the focus, thus simultaneously collecting data at four points in the boundary layer. Gragston *et al.* [5] used a diffractive optical element (DOE) to split the beam into 6 beams and collected data simultaneously at six points. Probing multiple points in the flow has the benefits of being able to track what is happening at multiple points and also be able to do some correlation studies by which velocities and other parameters can be quantified.

2.3.4.2 Theory

Conventional FLDI would be something similar to what was first setup by Parziale *et al.* at Caltech [97]. Fig. 2.12 shows the single beam-pair setup. A continuous-wave laser is sent into a diverging lens to expand the beam. As the beam expands it passes through a polarizer and then a

Wollaston prism that splits the beam in two orthogonally polarized beams with a certain separation angle (1-5 arcminute) between them. The beam pair is then focused by a converging lens to two points separated by a distance, this is called the beam-pair spacing. The beams then expand till they get to another focusing lens which is identical to the first one and get focused. The beam pair goes through a Wollaston prism that recombines the beam pair into one beam and then a polarizer that aligns the axes of polarization thus creating an interference fringe pattern. Like any other interferometer, the difference between the optical paths is what affects the fringe pattern. FLDI adds the focusing component by which the two beams share the same optical path except in the region where the beams focus to a point, thus making the system sensitive only in that region. This is very useful for measuring instabilities in a wind tunnel where there can be boundary layers on the tunnel walls or shear layers coming off the nozzle in a free-jet test section, like in the M6QT.

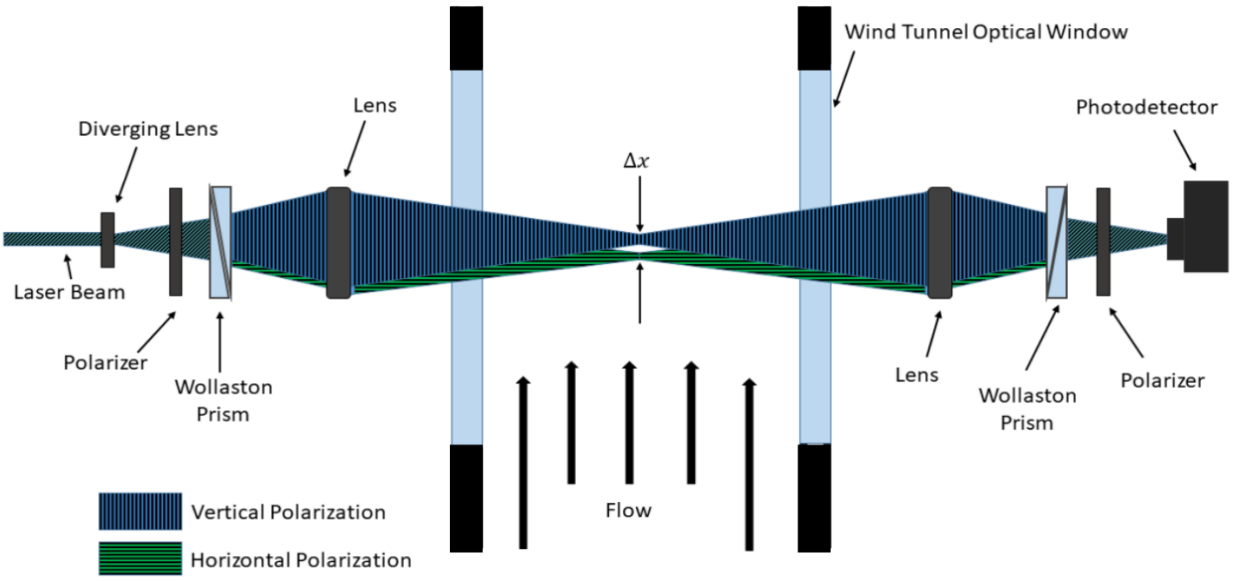

Figure 2.12: A basic single beam-pair FLDI setup (Reprinted with permission from [5]).

The index of refraction and density of a gas are related by the Gladstone-Dale relationship [100],

$$n - 1 = K\rho \tag{2.5}$$

where *n* is the index of refraction, *K* is a constant, and ρ is density. The optical path length difference (ΔOPL) between the two beams can be calculated,

$$\Delta OPL = \int_{s_1} n_1 \, ds \; - \int_{s_2} n_2 \, ds \tag{2.6}$$

where n_1, n_2 are indices of refraction and s_1, s_2 are the optical paths. The phase difference can then be defined and the Gladstone-Dale relation used to link the phase difference to the densities,

$$\Delta\phi = \frac{2\pi}{\lambda}(\Delta OPL) \tag{2.7}$$

$$\Delta\phi = \frac{2\pi}{\lambda}(\int_{s_1} n_1 \, ds \; - \int_{s_2} n_2 \, ds \;) \tag{2.8}$$

$$\Delta\phi = \frac{2\pi K}{\lambda}(\int_{s_1} \rho_1 \, ds \; - \int_{s_2} \rho_2 \, ds \;) \tag{2.9}$$

The last polarizer interferes the two beams along its transmission axis. The electric fields of the two beams can be defined,

$$E_1 = A_1 exp(j(kz - \omega t + \phi_1)) \tag{2.10}$$

$$E_2 = A_2 exp(j(kz - \omega t + \phi_2)) \tag{2.11}$$

where *A* is amplitude, *k* is wavenumber, ω is frequency, and ϕ is phase. The electric fields can be superimposed ($E = E_1 + E_2$) to find the irradiance at the photodetector (I_d) due to change in phase,

$$I_d = \langle EE^* \rangle = \langle (E_1 + E_2)(E_1 + E_2)^* \rangle \tag{2.12}$$

$$I_d = A_1^2 + A_2^2 + 2A_1A_2cos(\phi_2 - \phi_1) \tag{2.13}$$

$$I_d = I_1 + I_2 + 2\sqrt{I_1 I_2}cos(\Delta\phi) \tag{2.14}$$

The voltage output from the photodetector is proportional to the irradiance received by the sensor, $V = \eta I_d$, where η is a constant having to do with response time and resistive load. Thus Equation 2.14 can be written in terms of output voltage. The interferometer is set to the most linear part of the fringe to avoid phase ambiguity as shown in Fig. 2.13 which adds a phase shift of $\pi/2$. When setting up FLDI this can be set by translating the recombination Wollaston prism perpendicular to the optical axis. The beams can be assumed to be evenly split ($I_1 = I_2 = I$), this gives a max intensity of 4*I* and intensity at reference point of 2*I*. Thus the voltage can be written,

$$V - V_{ref} = V_{ref}cos(\Delta\phi) \tag{2.15}$$

where V_{ref} is the voltage at the reference point. The phase difference is adjusted to include the $\pi/2$ starting point and gives,

$$V = V_{ref}[1 - sin(\Delta\phi)] \tag{2.16}$$

The phase difference in Eq. 2.9 and Eq. 2.16 can then be equated to give,

$$sin^{-1}(1 - \frac{V}{V_{ref}}) = \frac{2\pi K}{\lambda}(\int_{s_1} \rho_1 \, ds \; - \int_{s_2} \rho_2 \, ds \;) \tag{2.17}$$

The beams traverse the same optical path throughout the system except for a characteristic length L near the focal point of the beams and so the equation can be simplified and written in

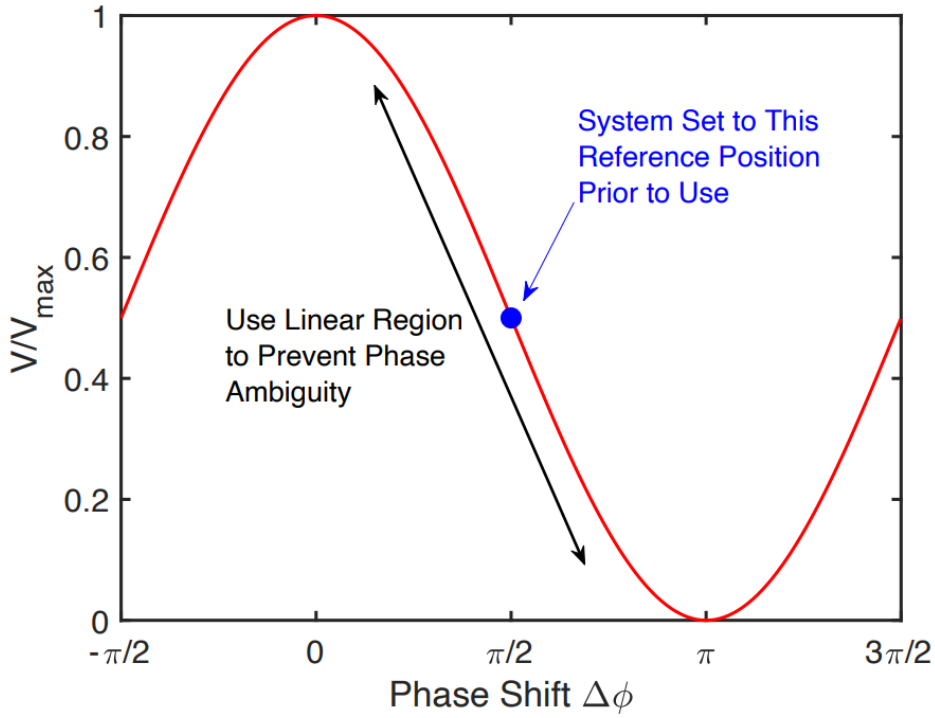

Figure 2.13: Photodetector voltage output and its relation to fringe intensity (Reprinted with permission from [5]).

terms of the densities,

$$\rho_2 - \rho_1 = \frac{\lambda}{2\pi KL} sin^{-1}(\frac{V}{V_{ref}} - 1) \tag{2.18}$$

This can also be written in terms of mean and fluctuation densities showing that the FLDI system is a useful tool to measure density fluctuations in the flow,

$$\frac{\rho'}{\langle\rho\rangle} = \frac{\lambda}{2\pi KL\langle\rho\rangle} sin^{-1}(\frac{V}{V_{ref}} - 1) \tag{2.19}$$

2.3.4.3 Implementation

Experiments were done with a few different configurations as this system evolved over time. The system initially used was developed by Gragston *et al.* at UTSI [5][101], a Diffractive Optical Element (DOE) (Holo-Or #MS-474-P-Y-A) was used to split the laser beam into a 1x6 array. The

technique was named Linear Array-Focused Laser Differential Interferometry (LA-FLDI) as 1-D or 2-D arrays of linearly-spaced FLDI beam pairs can be created using this approach [5]. Fig. 2.14 shows the setup around the M6QT.

A 10 mW HeNe 633 nm laser beam (Edmund Optics Lumentum) is diverged using a f=-12 mm plano-concave lens and then split into six beams by the DOE with a 0.71° separation angle. The beams then pass through a polarizer and are split into beam pairs by a Wollaston prism (United Crystals) with 5-arcminute separation angle. A plano-convex lens with f=250 mm is used to focus the beam pairs on top of the cone. Another identical convex lens focuses the beam onto another 5-arcminute Wollaston prism which recombines the beam pairs. The six beams then pass through a polarizer again to get the interference fringe. An f=-30 mm plano-concave lens then collimates the beams before they travel into the collection optic, which is an array of six fiber optic cables (Thorlabs M35L01). The fiber optic cables are coupled to photodetectors (Thorlabs PDA36A2) that feed into a NI PXI Data Acquisition (DAQ) system (NI PXI system with components NI PXIe-8381, NI BNC-2110, and NI PXIe-6368) which samples each channel at 2 MHz [75].

A MATLAB code was written to use geometrical optics to predict beam-pair spacing and size optics suitable for the setup. This code helps design the setup as tunnel constraints can be accounted for, like the wide free-jet test section, and perhaps other obstacles outside of the test section. The code also helps order optics in the right size as the spread of the beams is predicted. To be safe bigger optics were ordered than necessarily needed. The first campaign used 5-arcminute Wollaston prisms, the ray trace diagram and close-up of beam pairs is shown in Fig. 2.15. The close-up of the beam pairs shows a predicted beam-pair spacing of 374 μm and spacing between beam pairs of 939.2 μm.

A beam profiler (Ophir-Spiricon SP90425) was placed inside the test section very carefully with the model pulled back and beam profiler suspended over it to characterize the beam pairs at the focal point. Fig. 2.16 shows the beam pairs as observed with and without the diffractive optic. The beam-pair spacing was measured to be 375 μm and distance between beam pairs was measured to be 933 μm. A slight smearing effect is observed in the beams furthest away from

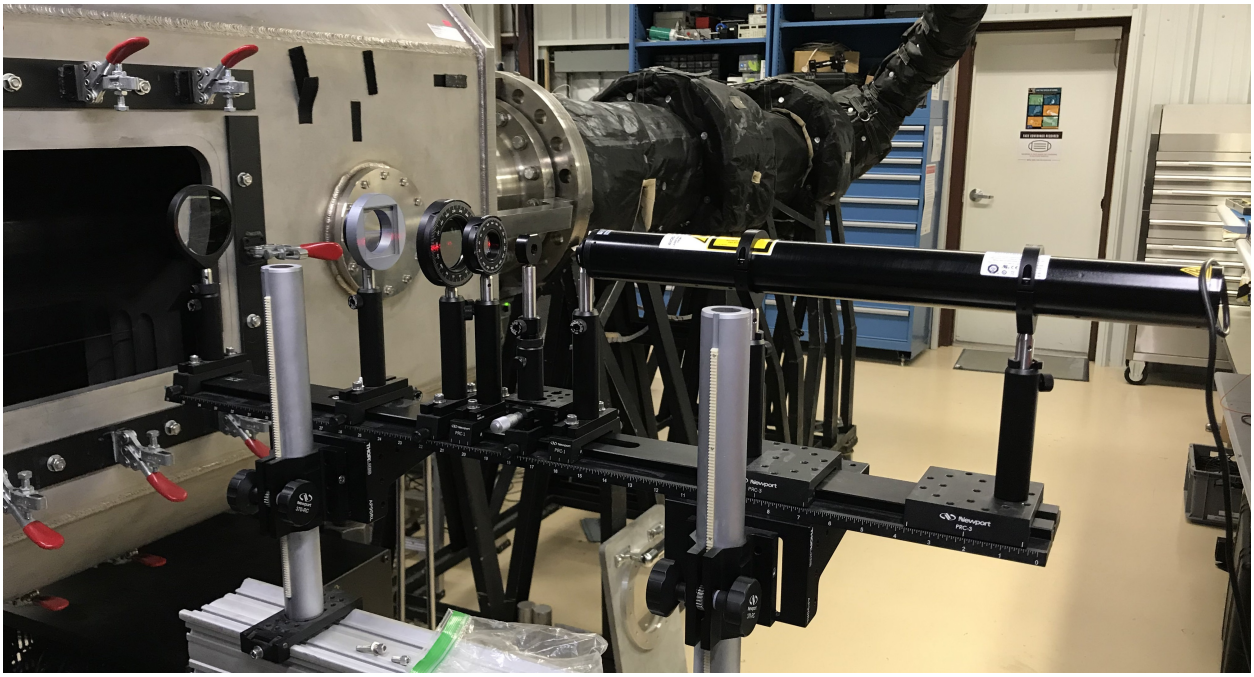

(a) Laser side

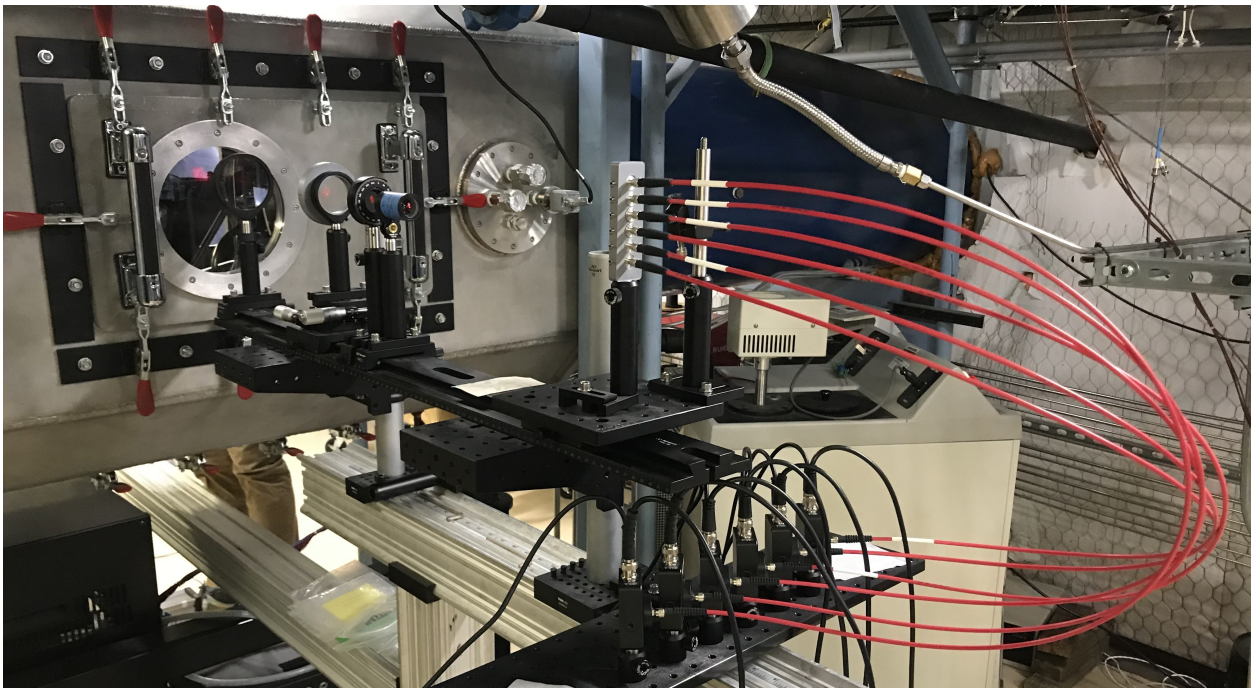

(b) Detector side

Figure 2.14: The LA-FLDI system setup on the M6QT.

center due to the beams approaching the focus at an angle. Note that the beams are shown in a horizontal line but were angled to match the slope of the cone at the measurement location. The

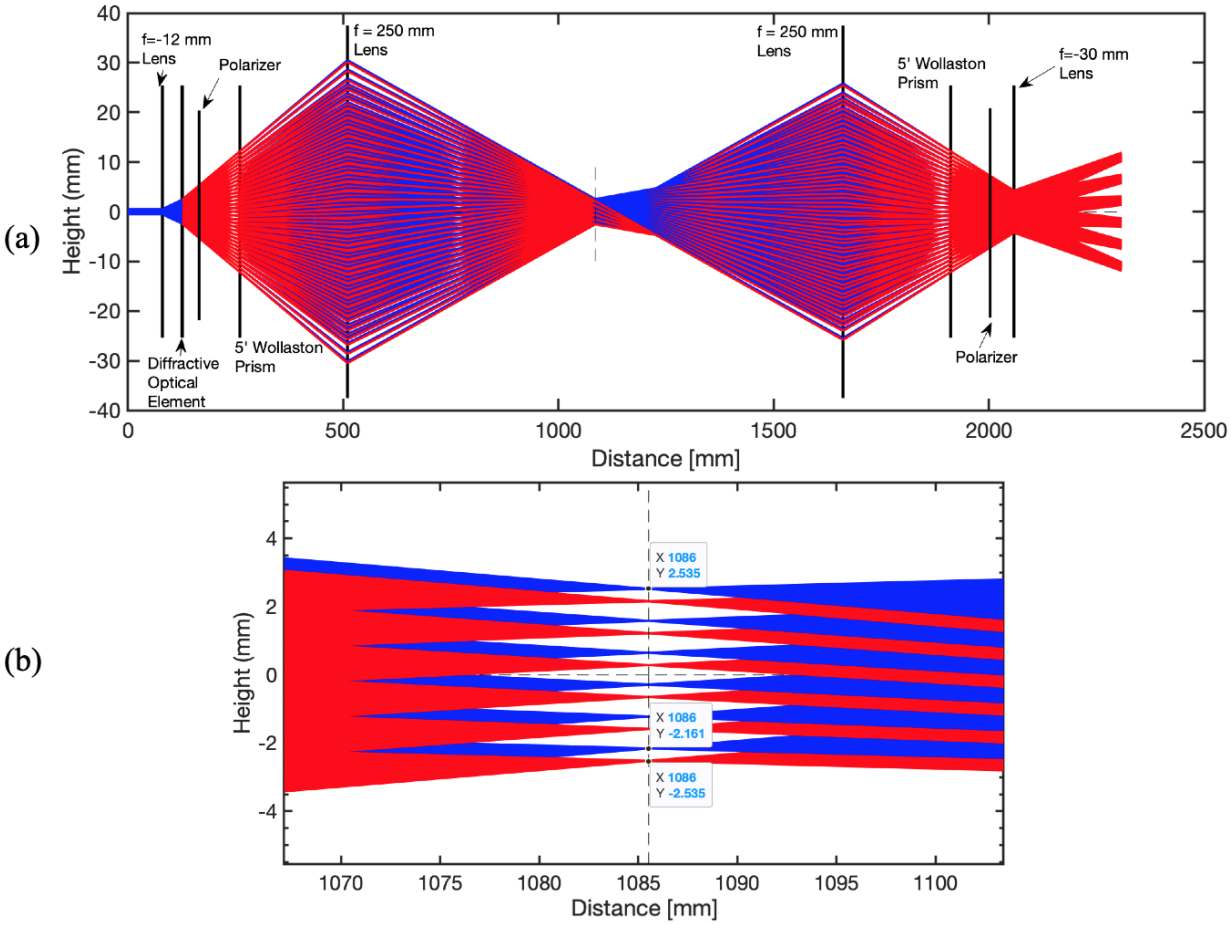

Figure 2.15: (a) A ray trace diagram of the LA-FLDI system with 5-arcminute prisms, (b) A close-up of the focus region showing the six beam pairs (Reprinted with permission from [6]).

measurement location was such that the most downstream beam was 25.4 mm from the end of the cone and 1.2±0.5 mm from the surface.

The 5-arcminute Wollaston prisms were replaced with 1.5-arcminute Wollaston prisms to reduce the beam-pair spacing for the second campaign. Fig. 2.17 shows the prediction from the ray-trace diagram and a close-up of the beam pairs. The close-up of the beam pairs shows a predicted beam-pair spacing of 114 µm and spacing between beam pairs of 1085 µm. The beam profiler (Ophir-Spiricon SP90425) was used again to characterize the beam pairs at the focal point. Fig. 2.18 shows the beam pairs as observed with the diffractive optic. The beam-pair spacing was measured to be 130 µm and distance between beam pairs was measured to be 1070 µm. The differ-

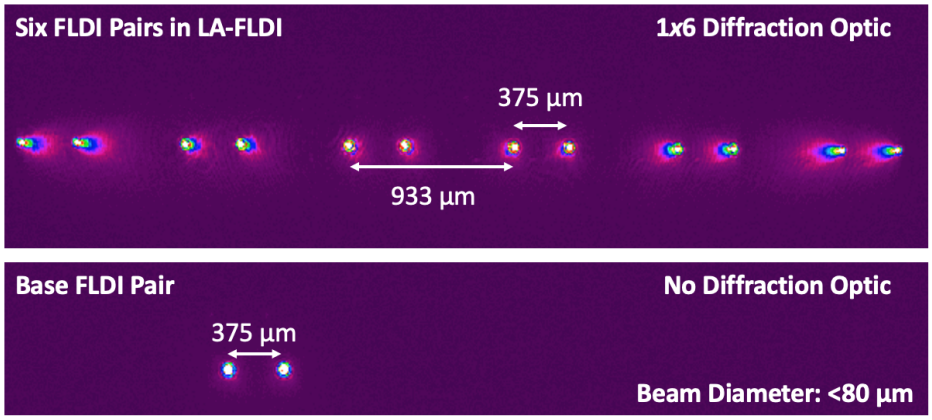

Figure 2.16: Beam pair characterization with a beam profiler for the setup with 5-arcminute prisms, shown with and without the DOE (Reprinted with permission from [6]).

ence in the predicted and measured values of beam spacing can be attributed to the uncertainty in placement of the DOE as this affects the beam pairs and their spacing. The beam pairs were angled to match the slope of the cone at the measurement location which was with the most downstream beam approximately 25.4$\pm$0.5 mm from the end of the cone and 1$\pm$0.5 mm from the wall in the wall-normal direction.

(a)

(b)

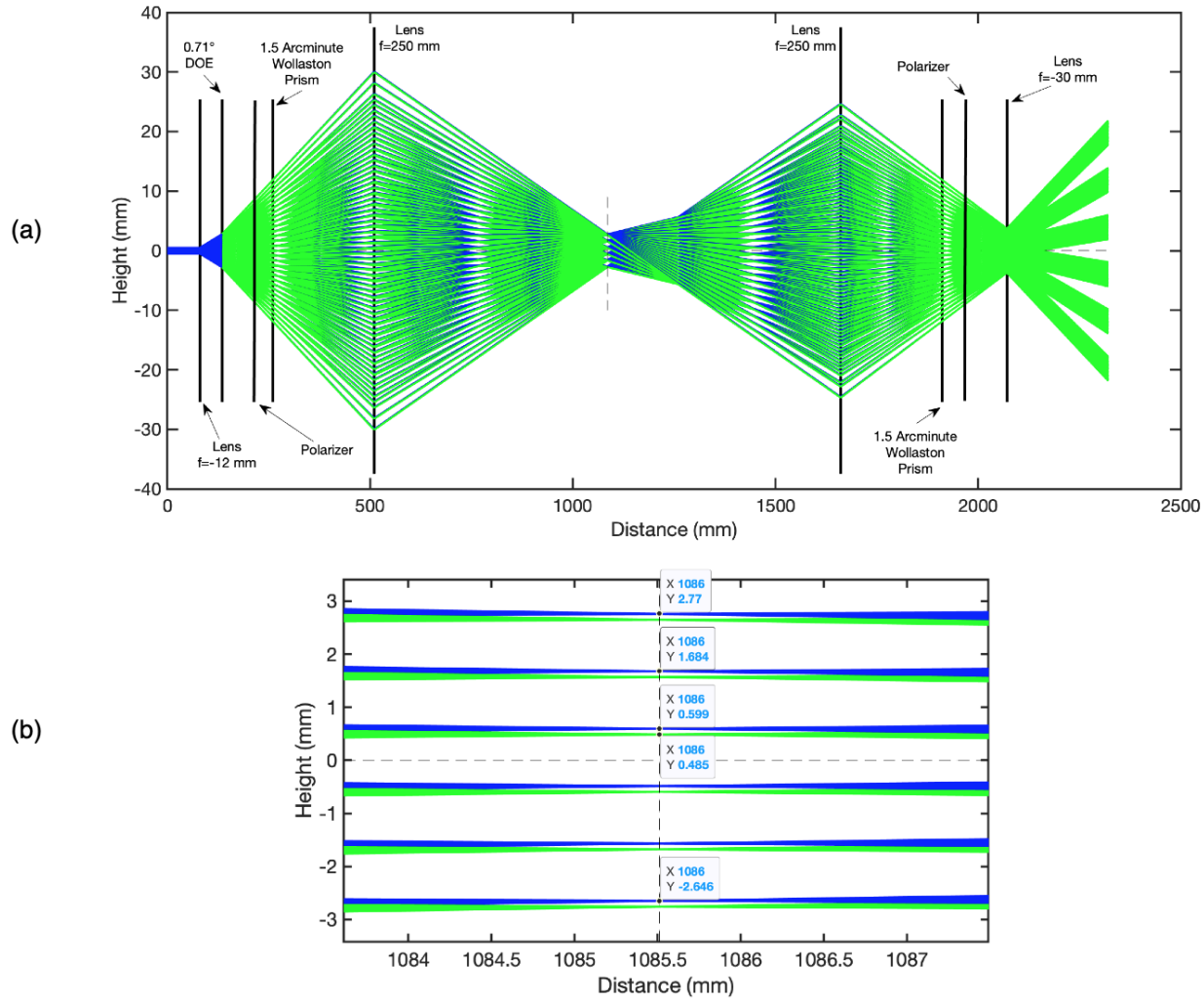

Figure 2.17: (a) A ray trace diagram of the LA-FLDI system with 1.5-arcminute prisms, (b) A close-up of the focus region showing the six beam pairs.

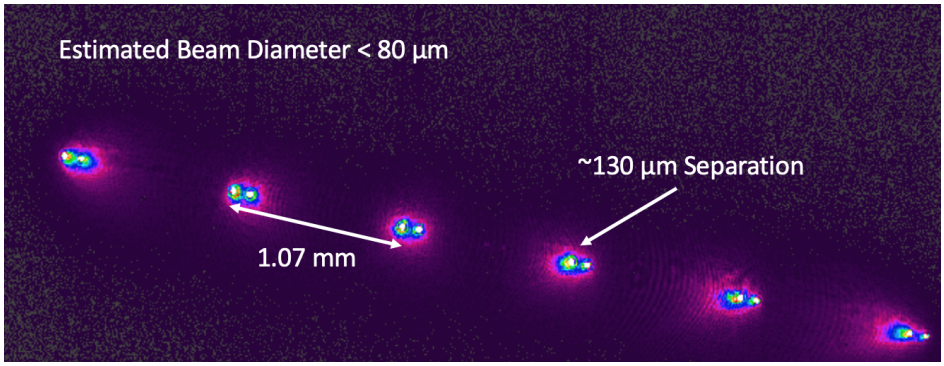

Figure 2.18: Beam pair characterization with a beam profiler for the setup with 1.5-arcminute prisms.

3. RESULTS*

3.1 Blockage model

A blockage model was machined to test diagnostics and do shakedown runs without putting the very delicate 91-6 cone model at risk. The blockage model was also much easier to install and remove from the M6QT test section owing to the lack of instrumentation and coolant tubing, thus posing less risk to the delicate nozzle of the tunnel. The blockage model was machined from a solid cylinder of 6061 Aluminum and designed to be the exact shape as the 91-6 cone. The blockage model was simply machined on a lathe and not polished further, it also had a larger-diameter nose tip than the original 91-6 cone.

The blockage model was used to do several wind tunnel runs and determine how far into and out of the nozzle the cone could be pushed and the tunnel still be started. Tunnel "start" is when the flow in the test section goes hypersonic. Due to the unique characteristics of the nozzle and the diffuser there are positions where certain models will not allow the tunnel to start. This can be caused by various interactions between shocks created by the model and nozzle and how these shocks interact with the diffuser. After several wind tunnel runs the ideal position for the 91-6 cone was found to be with the aft end of the cone 38 mm out of the nozzle exit. At this position the wind tunnel started reliably and left enough of the model outside the nozzle for optical diagnostics to be used. For longer models care must be taken to make sure the model does not interfere with the last characteristic coming from the nozzle throat which is approximately halfway down the nozzle.

The blockage model was also used as a platform to test distributed roughness elements (DREs) when they were being brainstormed and designed, and to refine the application process, see Fig. 3.1. A few variations were tested on the blockage model and profilometry measurements carried out to ascertain how DREs made with material of different thicknesses measured after being applied, as seen in Fig. 3.2. The durability of the DREs was also tested by applying and removing them. Using the blockage model for all of this work kept the original model safe while techniques

*Parts of this chapter are reprinted with permission from [7].

were perfected and DREs were applied without causing any damage to the delicate model.

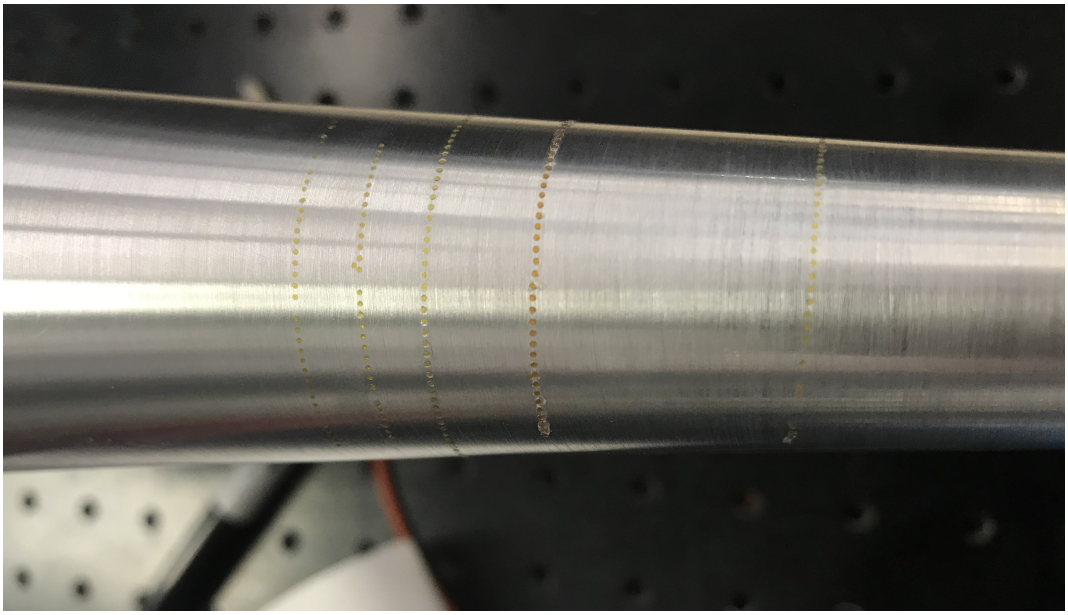

Figure 3.1: Multiple strips of practice DREs on the blockage model.

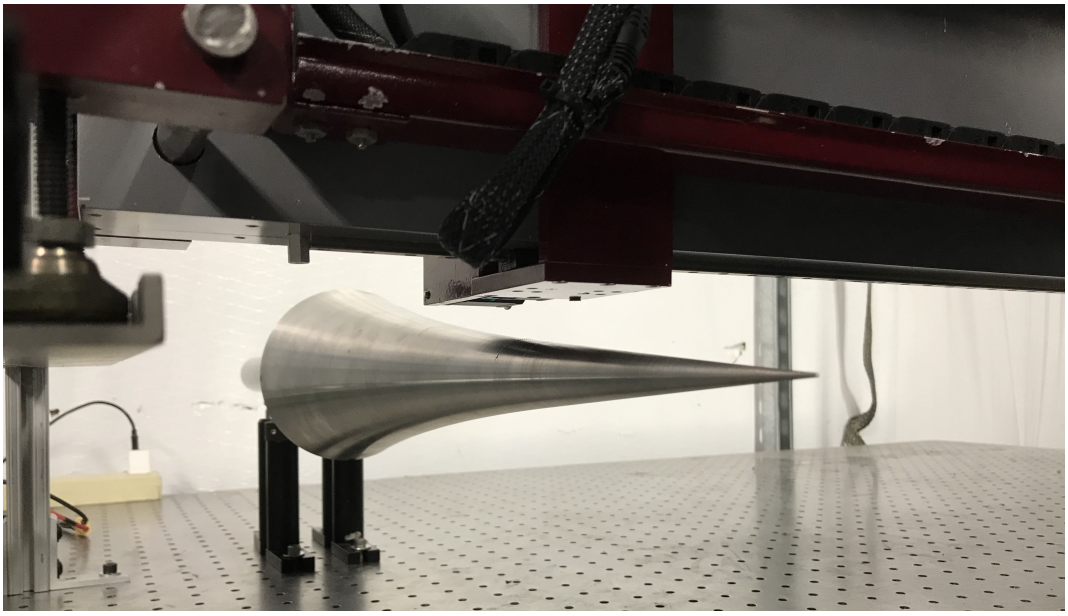

Figure 3.2: DRE characterization using a laser profilometer on the blockage model.

3.2 Smooth cone

The smooth cone refers to the original cone as designed without any roughness added throughout this work. The model was used as received from Purdue University initially but after an incident with the tip it was sent to Modern Machine & Tool Co., Inc. in Newport News, VA where a new tip was machined and installed. The tip was manufactured to the specifications outlined in the original model drawings from NASA in 1993, more details in Appendix A. The entire model was also polished and an extra tip machined in case another incident were to happen. As of this writing, the extra tip has not been used and resides in the same box as the cone.

3.2.1 Temperature profiles

The embedded thermocouples in the 91-6 flared cone provide a consistent diagnostic in terms of temperature profiles. There are 51 type-T thermocouples and they form a streamwise line along the port side of the model starting at 50.8 mm from the tip and ending at 444.5 mm from the tip. The first five thermocouples are spaced 25.4 mm apart, presumably due to spatial constraints in the narrow fore section of the model. The other forty-six thermocouples after the first five are spaced 6.35 mm apart. The temperature profiles can be studied over several runs to ascertain the state of the boundary layer. The recirculating chiller was set to coolant set points 20 °C, -20 °C, and -60 °C. Fig. 3.3 shows the typical temperature profiles that are seen for the different coolant set points. There is a distinctive shape to the temperature profile caused by how the coolant flows through the model. The coolant enters the model in a tube in the centre and recirculates to the back before exiting the model, this causes the shape of the temperature profile in addition to higher heating near the nose tip as the detachable tip does not get cooled. There was some concern that the pattern was caused by the nozzle shear layers interacting with the boundary layer on the model. To alleviate these concerns the model was moved as far into and out of the nozzle as possible while the temperature profiles were observed. The profiles stayed consistent and did not change with the position of the model.

For all temperature cases an increase in heating is observed followed by a plateau, this can be

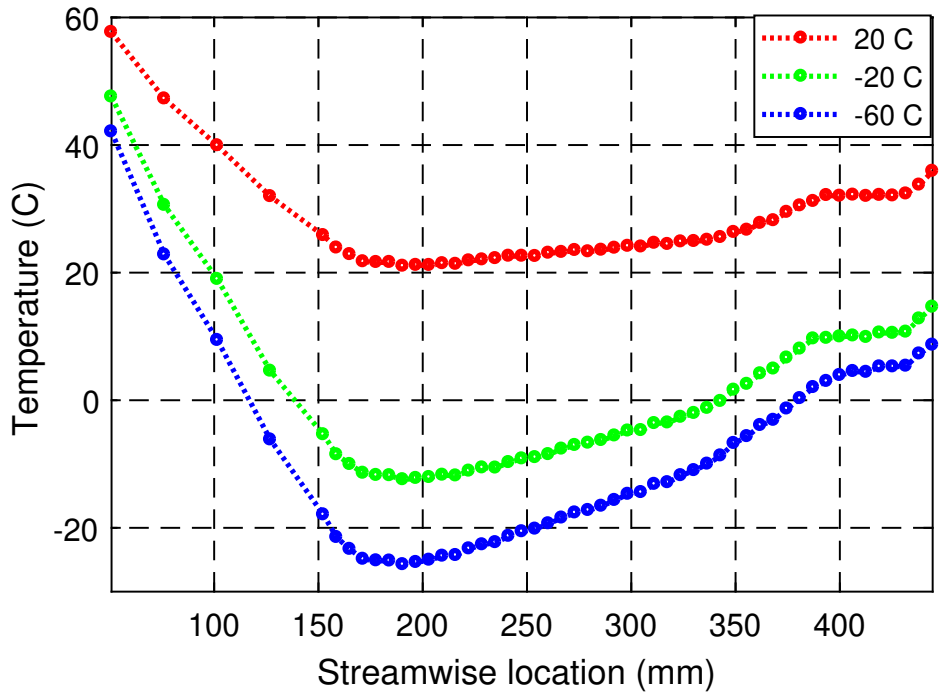

Figure 3.3: Temperature profiles at three coolant set points of 20 °C, -20 °C, and -60 °C on the smooth cone at unit Reynolds number of 9x10^6 /m.

attributed to the boundary layer starting to transition (increased heating). Qualitatively it can be said that the increase in heating happens earlier for the colder wall cases. This can be quantified by drawing straight lines on the temperature profiles and using the intersection points as locations of start of transition as shown in Fig. 3.4. The transition onset location moves from 342.9 mm from the tip for the 20 °C case to 330.2 mm for the -20 °C case and then to 317.5 mm for the -60 °C case. The earlier onset of transition is caused by the boundary layer thickness decreasing and moving the sonic line closer to the surface, thus increasing the Mack-mode frequency and increasing its destabilizing effect [75].

The unit Reynolds number was swept from 8x10^6 /m to 11x10^6 /m by steadily increasing the pressure in the settling chamber over the course of a wind tunnel run. The same three coolant set points of 20 °C, -20 °C, and -60 °C were used again. The objective was to observe the temperature profiles as the boundary layer destabilizes from laminar to transitional and eventually becomes fully turbulent. The temperature profiles at unit Reynolds numbers of 8, 9, 10, and 11 x10^6 /m

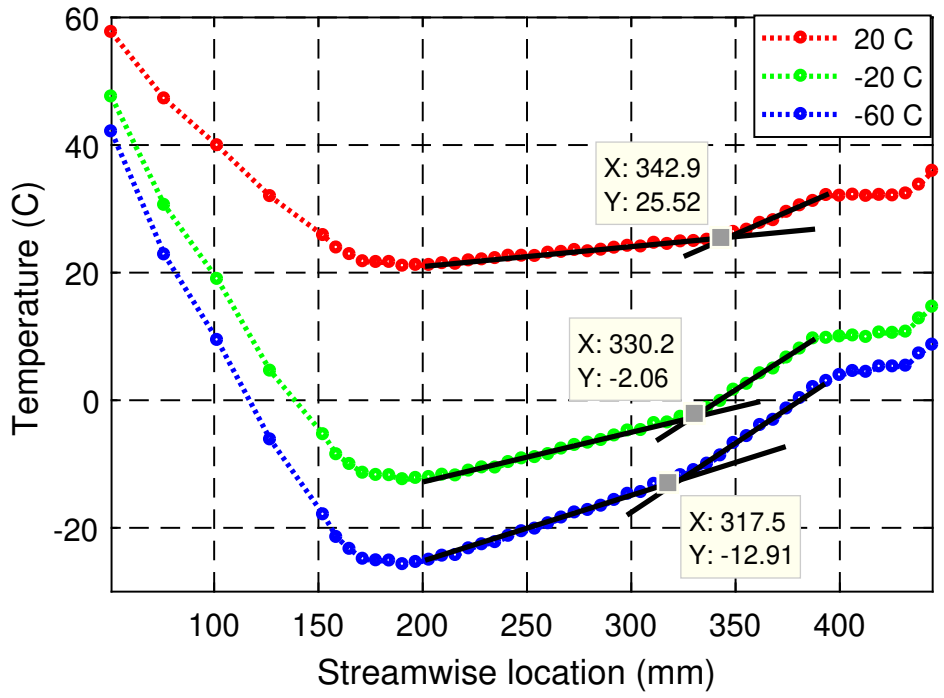

Figure 3.4: Temperature profiles on the smooth cone at unit Reynolds number of 9x10^6 /m with quantification of transition onset location.

have been plotted for each coolant set point. Fig. 3.5 shows the temperature profiles from the smooth cone at coolant set point 20 °C. The onset of transition moves upstream as the Reynolds number increases and the heating also increases as the Reynolds number is increased. The locations can be quantified but drawing that many lines leaves the image hard to decipher and so the data have been presented qualitatively here. The temperature profiles at the aft end of the cone are very similar for the 8x10^6 /m and 9x10^6 /m profiles but an increase is observed for the 10x10^6 /m profile. The 11x10^6 /m profile shows a significant increase in temperature compared to the lower Reynolds numbers, indicating a fully turbulent boundary layer.

Fig. 3.6 shows similar behavior for the -20 °C case. The transition onset location moves upstream with higher Reynolds number. The temperature profiles are seen to again be similar for the 8x10^6 /m and 9x10^6 /m unit Reynolds number profiles. The profile at unit Reynolds number 10x10^6 /m is significantly higher at the aft end of the cone than that seen for the 20 °C case, this signifies greater destabilization with wall cooling. The 11x10^6 /m profile shows higher heating

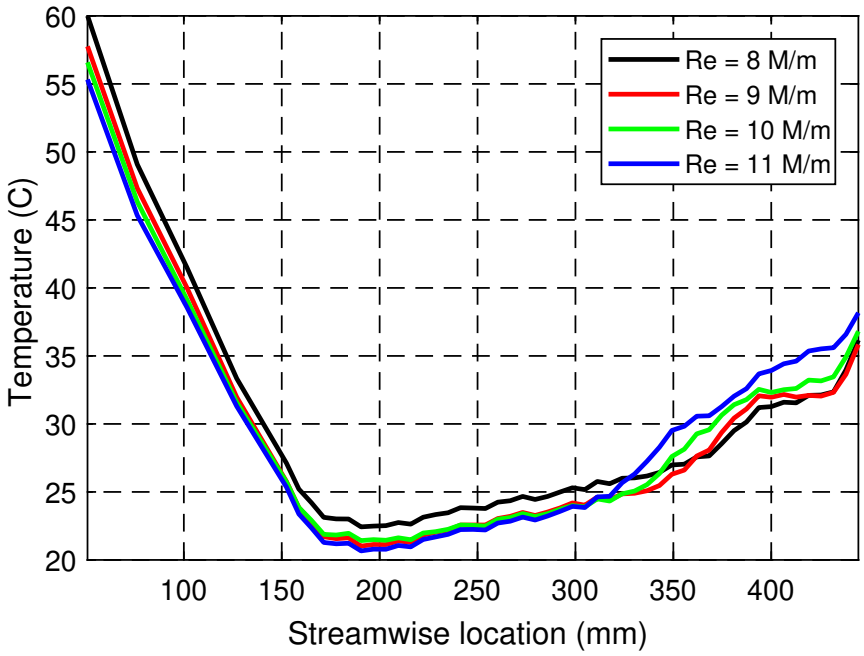

Figure 3.5: Temperature profiles over Reynolds number sweeps for the smooth cone at 20 °C coolant set point.

again and signifies a fully turbulent boundary layer.

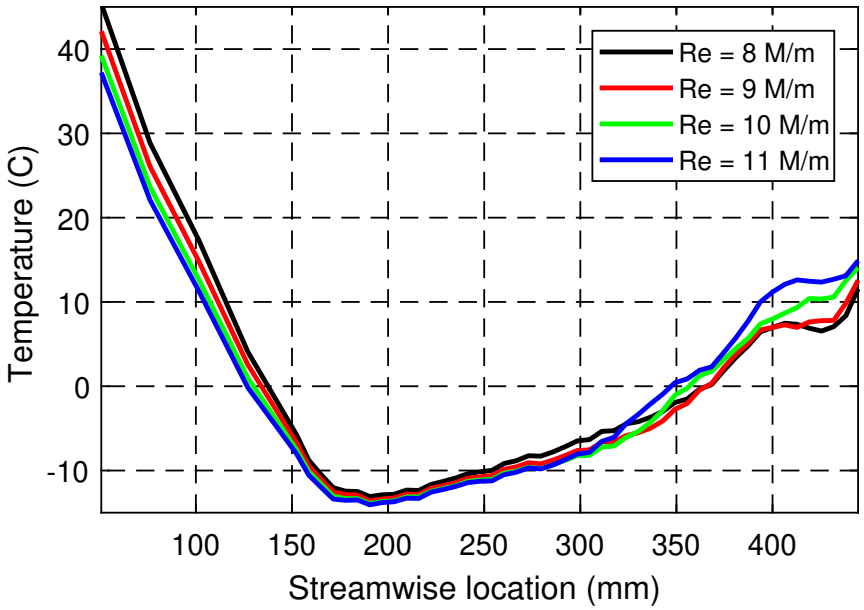

Figure 3.6: Temperature profiles over Reynolds number sweeps for the smooth cone at -20 °C coolant set point.

Fig. 3.7 shows the temperature profiles over the course of a Reynolds number sweep for the -60 °C coolant set point case. Similar trends to the two previous cases are observed with the transition onset locations moving further upstream as the Reynolds number is increased. The $8x10^6$ /m and $9x10^6$ /m unit Reynolds number profiles are observed to be very similar and the $10x10^6$ /m profile shows increased heating at the aft end. The $11x10^6$ /m unit Reynolds number profile shows even higher heating as expected.

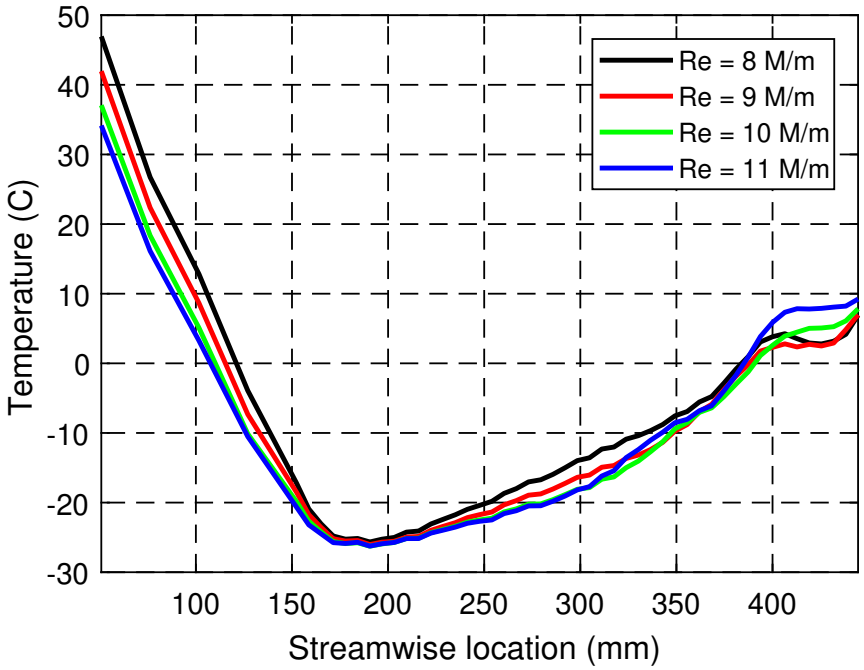

Figure 3.7: Temperature profiles over Reynolds number sweeps for the smooth cone at -60 °C coolant set point.

3.2.2 Mack-mode instabilities

The Mack-mode instability has been identified as the the dominant cause of boundary-layer transition and is the focus of this study. The Mack mode was studied using the focusing schlieren technique to visualize the Mack-mode "rope-like" structures using a camera. Then point measurements were taken with a fiber-optic coupled photodetector to analyze spectral content in the boundary layer.

3.2.2.1 Focusing Schlieren

The focusing schlieren system was setup with a Photron FASTCAM SA-Z. The camera is capable of a frame rate of 2 MHz and shutter time of 0.16 µs. Using a frame rate of 2 MHz decreases the field of view to a small area and reduces how many frames can be recorded owing to limitations of the camera's on-board memory. Due to those limitations the camera settings were set to a frame rate of 1500 fps and a shutter time of 0.16 µs, this provides for the field of view to capture the entirety of the cone that is outside the nozzle and enough data storage to record the full wind tunnel run. This way Reynolds number sweeps can be carried out and the boundary layer observed as it goes from laminar to turbulent. Fig. 3.8 shows the Mack-mode instability on the aft end of the model as visualized using the focusing schlieren diagnostic. The wavelength of the waves seen equate to a frequency of $\sim$300 kHz as expected for the Mack mode. The boundary layer was seen to decrease in thickness as the Reynolds number was increased and intermittently lose structure. The intermittency of the breakdown increased as Reynolds number increased till eventually there was no more structure and the boundary layer was fully turbulent. Quantifying transition onset is difficult from these data as some arbitrary definition of transition dependent on intermittency level would have to be made. Instead the data collected using the camera were used as a qualitative measurement showing presence of Mack-mode waves and confirming the trends seen in the data from the other diagnostics.

The camera was replaced with a fiber-optic coupled photodetector and the wind tunnel runs repeated. The time-domain voltage data from the photodetector were acquired by the DAQ at a sampling rate of 2 MHz as this is the maximum the DAQ was capable of. It should be noted that the photodetector is capable of far higher frequencies and the DAQ is the limiting factor. There are DAQs capable of sampling at 8-10 MHz on the market now and it would be worthwhile to repeat these experiments with a higher-spec DAQ. The time-domain data were converted to frequency domain using Welch's method where segment size was 2^8 and overlap was 50%. This gives us data in the frequency domain to 1 MHz with a resolution of 7.8 kHz. Thus there is an uncertainty of $\pm$3.9 kHz in these data. The fiber optic was positioned to take data at a point in the boundary layer

Figure 3.8: Focusing schlieren image showing Mack-mode structures on the smooth cone at coolant setpoint -60 °C.

25.4 mm from the aft end of the cone.

The focusing schlieren diagnostic with the photodetector was used as an alignment tool to zero the angle of attack of the model. Hofferth [2] observed a variation in the frequency of the Mack mode with angle of attack on the 93-10 cone. A study was conducted with the angle of attack changed and runs repeated and showed that the Mack-mode frequency changed by 84 kHz for 1° change in angle of attack. Kocian [7] carried out LPSE computations for the 93-10 cone and found the Mack-mode frequency to vary by 73 kHz per 1° angle of attack. Fig. 3.9 shows the experimental and computational results. Thus the Mack-mode frequency is very sensitive to angle of attack. Since the 91-6 cone is a very similar geometry to the 93-10 cone, we can assume it is also highly sensitive. This sensitivity can be used to align the model by changing the angle of attack and placing the focusing schlieren system on top and bottom of the cone (at the same streamwise location) in subsequent runs and quantifying the difference in frequency at the same wind tunnel conditions. This is repeated till the frequencies match. For the 91-6 cone this was accomplished by using shims between the model sting and the mounting plate in the M6QT. This procedure was

repeated every time the 91-6 cone model was installed, the total shim thickness required to zero the angle of attack using this method was found to be repeatable.

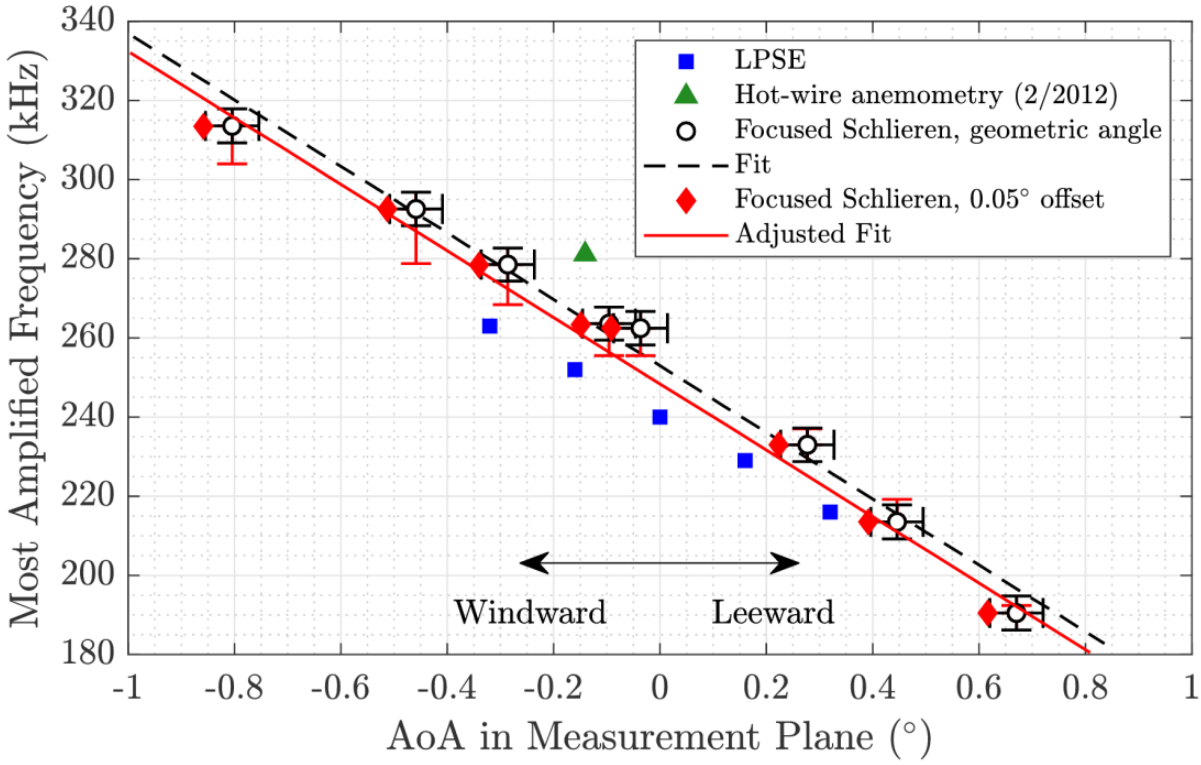

Figure 3.9: Variation of Mack-mode frequencies as seen from experiments and computations on the 93-10 cone (Reprinted with permission from [7]).

The unit Reynolds number was steadily increased from 8x10^6 /m to 11x10^6 /m for the three coolant set points. Fig. 3.10 shows the data for the coolant set point 20 °C case. The Mack-mode peak is seen to have a frequency of 289.1±3.9 kHz at a unit Reynolds number of 8x10^6 /m and as the Reynolds number increases the frequency is seen to increase as well. The spectral energy away from the peak stays the same up to a unit Reynolds number of 9.2x10^6 /m and after that the spectral energy increases and the peak gets smaller. This increase in spectral energy is thought to be the onset of transition and further breakdown as it keeps increasing. Eventually the spectral energy and peak come together to form a line at unit Reynolds number of 10.5x10^6 /m, at this point the

boundary layer is thought to be fully turbulent.

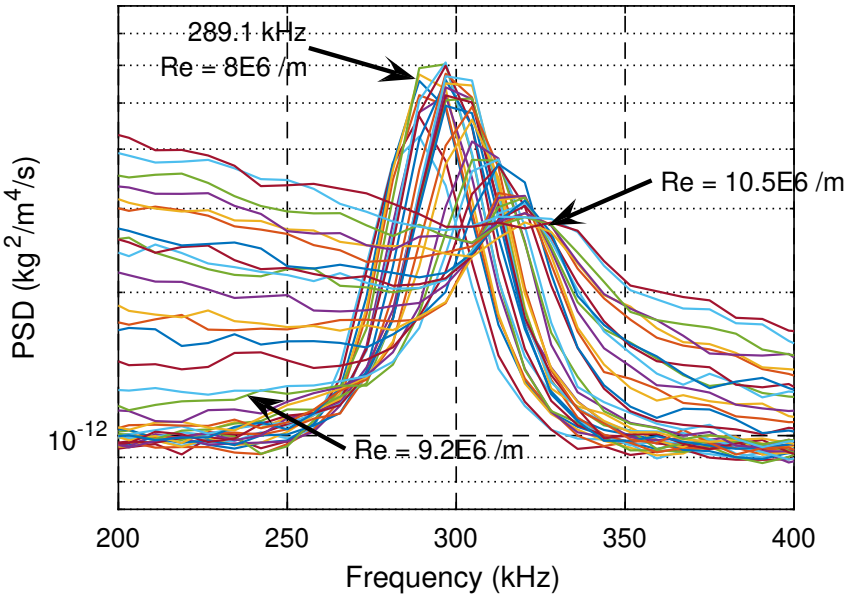

Figure 3.10: Spectral data from focusing schlieren on the smooth cone at coolant setpoint 20 °C.

Fig. 3.11 shows the spectral data for the -20 °C coolant set point case. The frequency of the Mack mode at a unit Reynolds number of $8\text{x}10^6$ /m is seen to be 296.9±3.9 kHz. This is higher than that seen for the 20 °C case, this increase can be attributed to the decrease in boundary-layer height from wall cooling. The increase in frequency has a destabilizing effect, the spectral energy increases at a unit Reynolds number of $9\text{x}10^6$ /m and the boundary layer is turbulent at $9.8\text{x}10^6$ /m.

Fig. 3.12 shows the spectral data for the -60 °C coolant set point case. The frequency of the Mack-mode peak is seen to be 296.9 kHz at a unit Reynolds number of $8\text{x}10^6$ /m. This is perplexing at first as it is the same as that seen for the -20 °C case but there is an uncertainty of ±3.9 kHz on these values so it is possible that the frequency is higher for the colder wall case. The destabilizing effects of wall cooling are observed again with the spectral energy increasing at a unit Reynolds number of $8.8\text{x}10^6$ /m and the boundary layer fully turbulent at a unit Reynolds number of $9.5\text{x}10^6$ /m.

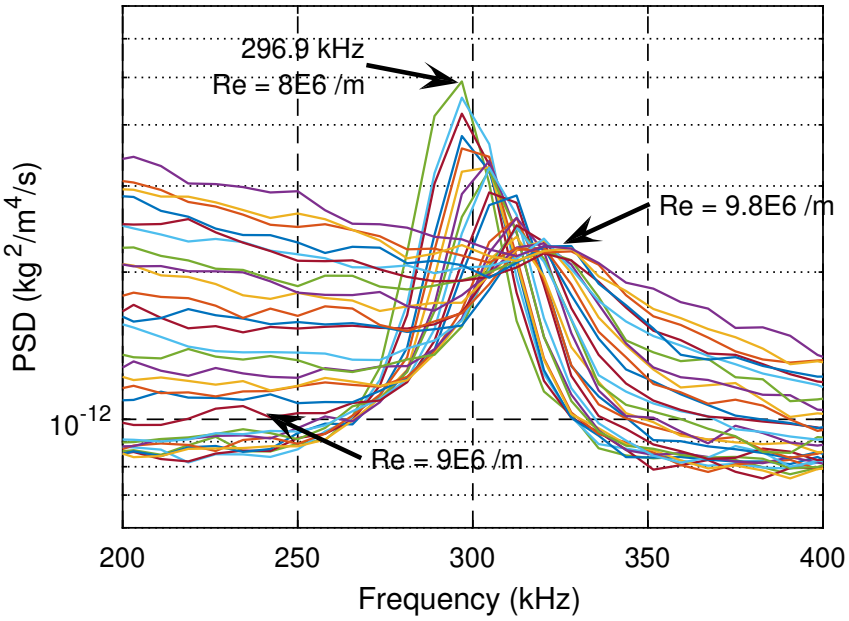

Figure 3.11: Spectral data from focusing schlieren on the smooth cone at coolant setpoint -20 °C.

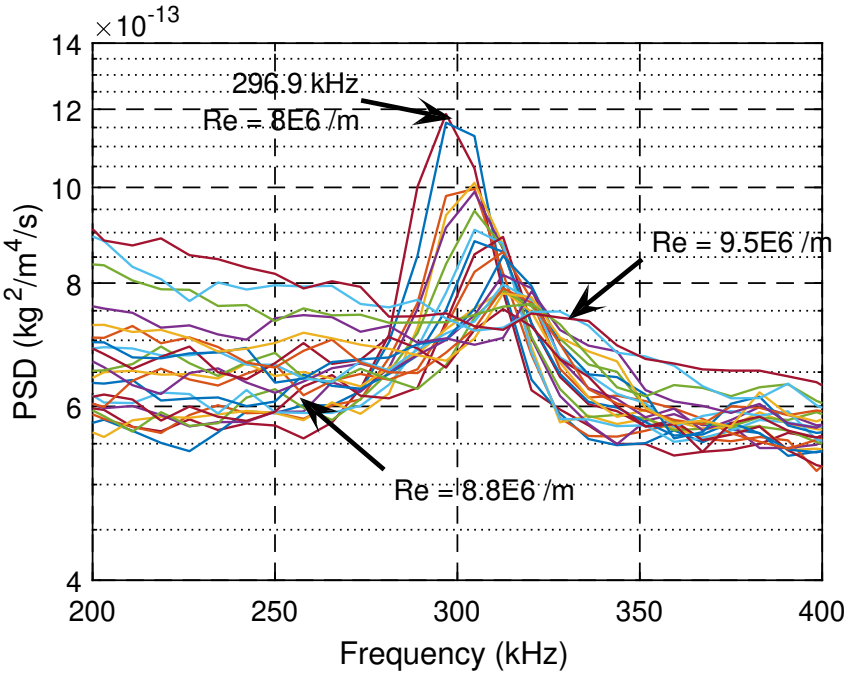

Figure 3.12: Spectral data from focusing schlieren on the smooth cone at coolant setpoint -60 °C.

3.2.3 Görtler instabilities

The Görtler instability is caused by curvature and is a 3-D structure in the boundary layer. It destabilises the boundary layer and is a contributor to boundary-layer transition and therefore is being studied here. The Görtler instability cannot be studied very well by diagnostics that take axial measurements along a streamline like the focusing schlieren and FLDI techniques. The boundary layer has to be studied with spanwise surveys to map the Görtler vortices.

Constant Temperature Anemometry (CTA) was used with a hot-film probe to probe the boundary layer and the voltage output was mapped to study the mass-flux variation. As discussed in Sec. 2.3.2.1, the bridge voltage from the anemometer can be used to represent the mass flux to qualitatively look at mass-flux variations in the boundary layer. The hot film location was 35 ± 0.5 mm from the aft end (422.2 ± 0.5 mm from the tip) of the cone. The raw voltage and filtered/amplified voltages (as discussed in Sec. 2.3.2.3) were sampled at 500 kHz for 100 ms at each measurement point. Azimuthal sweeps were performed from 80° to 100° with a standard coordinate system where 0° is the streamline along the port side. Only two sweeps could be completed during one wind tunnel run so multiple wind tunnel runs had to be carried out to map the boundary layer. The distance from the surface was estimated by placing the hot-film sensor in its probe holder very close to the surface as it would be during a wind tunnel run and taking pictures. The pictures were then used to measure wall-normal distance from model surface to the sensor using ImageJ software and also measuring known quantities like the length and width of the sensor holder. These measurements were then used to recover the distance from the sensor to the model. Another approach to calibrate this distance is to use a probe with a second contact probe at a known distance from the sensor, this can then be touched to the model to ascertain the distance of the sensor, but this approach is not suitable for delicate models like the 91-6 cone and was not used.

Fig. 3.13 shows the voltage variation (representative of mass-flux variation) maps created from wind tunnel runs where hot films were traversed through the boundary layer to collect data. Fig. 3.13a is for the 20 °C coolant set point case and does not show strong structure but some periodic variation is seen. In Fig. 3.13b the structures get more defined and definite peaks are seen, five

peaks can be discerned which on average over a 20° span equates to a wavenumber of 90. Fig. 3.13c shows the data collected for the -60 °C coolant set point case and shows a reduction in the boundary-layer height as expected when the model wall is cooled and the same peaks observed earlier with more structure. Overall it can be concluded that the wall cooling caused the boundary-layer height to decrease and made the Görtler vortices more prominent. Computational work supported these measurements by showing the Görtler instability to have a wavenumber of 90.

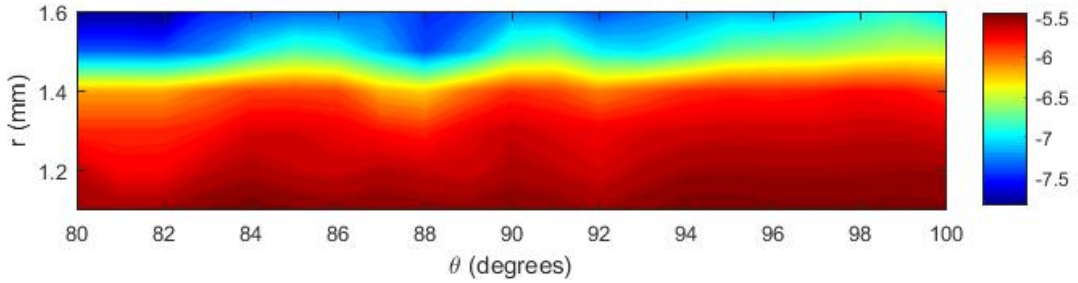

(a) Coolant set point 20 °C

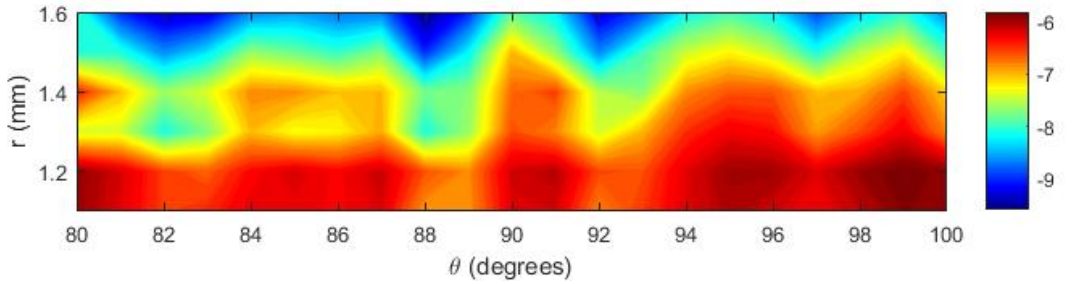

(b) Coolant set point -20 °C

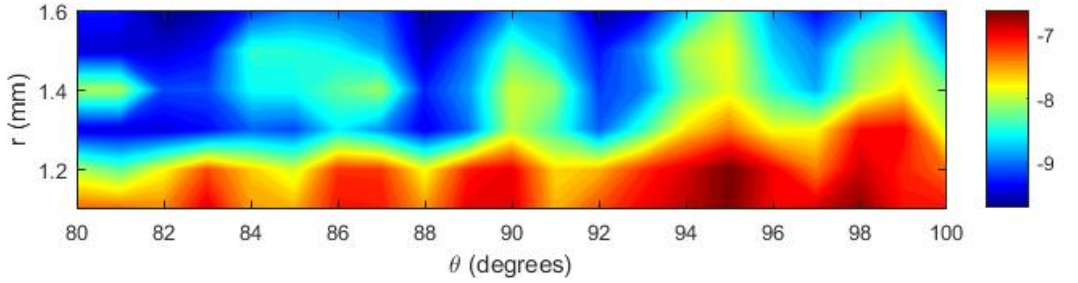

(c) Coolant set point -60 °C

Figure 3.13: Hot-film voltage variation over a 20° azimuthal sweep on the smooth cone at a unit Reynolds number of $9x10^6$ /m.

3.3 Cone with DREs

After all the available diagnostics were used on the smooth cone, periodic spanwise (azimuthal) distributed roughness elements (DREs) were added. The DREs are meant to further destabilize the flow so the transition process can be observed on what is essentially a modified model. The spacing was chosen to be the same wavenumber as that of the Görtler vortices seen from hot-film anemometry and confirmed by computations. The DREs were made circular with the same diameter as the spacing. The height was measured by a profilometer to be 81$\pm$3.6 μm and the diameter (and spacing) measured to be 465$\pm$7.6 μm. The streamwise location was decided from the computations as being where the flare starts, 152.4 mm from the tip, as this is where the Görtler instability starts. All the diagnostics used on the smooth cone were used again on the cone with DREs with the addition of Focused Laser Differential Interferometry (FLDI) which was not used on the smooth cone as it has only recently been implemented at the NAL.

3.3.1 Temperature profiles

As for the smooth cone, the thermocouples embedded in the model provided a diagnostic via temperature profiles. To reiterate, there are 51 thermocouples in a streamwise array along the port side of the model. The first point is at 50.8 mm from the tip and the last point is at 444.5 mm from the tip. The first five are spaced 25.4 mm apart and the other forty-six are spaced 6.35 mm apart. The recirculating chiller was set to 20 °C, -20 °C, and -60 °C again and the temperature profiles observed.

Fig. 3.14 shows the temperature profiles for the three coolant set points. The distinctive shape of the temperature profile is due to the way coolant flows in the shell. The temperature is highest near the tip as the tip is detachable and the cavity for the coolant does not extend into it. Moving backwards from the tip the temperature decreases as the coolant is able to cool the cone, and after a certain point the temperature rises as the coolant warms up on its way to the exit channel. The temperature is linear to a certain point where the slope changes, this point is thought to be where the boundary layer starts to transition. This point is termed the transition onset location and after

this the temperature plateaus and then has a final uptick. The plateau and uptick are thought to be from the way the coolant flows through the cone as well, the final uptick is likely from heat conducting forward from the hot sting assembly. Blanchard and Selby [67] marked the point where the temperature profile plateaued to be the transition location but other diagnostics used for this work show that the boundary layer is not fully turbulent at low Reynolds numbers (where the plateau is also seen) and so their conclusion is not accurate.

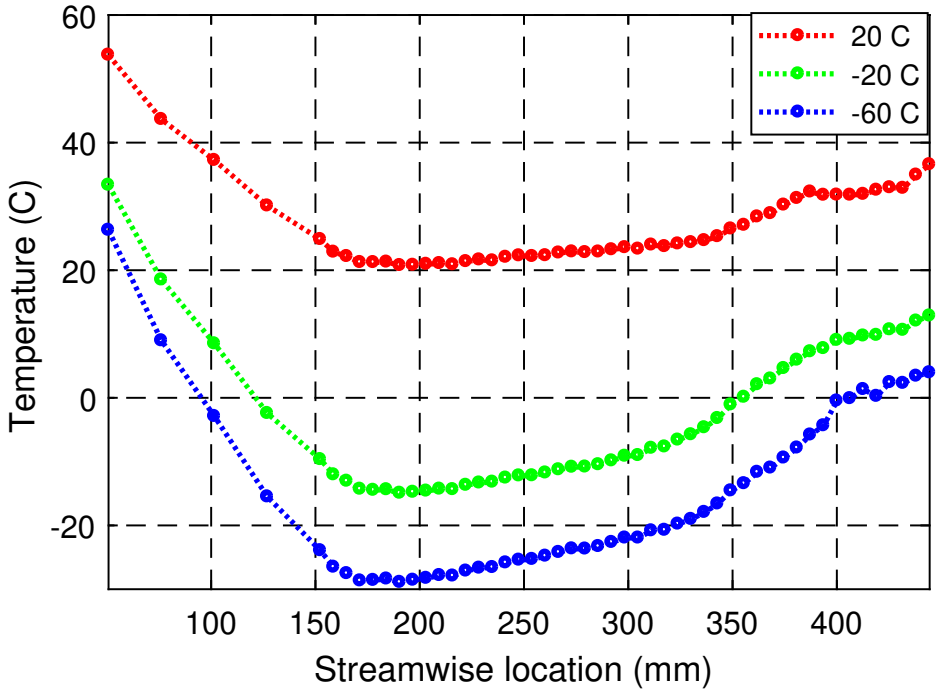

Figure 3.14: Temperature profiles at three coolant set points of 20 °C, -20 °C, and -60 °C on the cone with DREs at a unit Reynolds number of 9x10^6 /m.

The increase in heating observed in the temperature profiles can be quantified by drawing lines and marking the points where the slope changes. This was done for the smooth cone and a similar approach was used by Blanchard and Selby at NASA Langley [67]. Fig. 3.15 shows the lines drawn on the temperature profiles and points marked. The transition onset location moves from 336.5 mm from the tip for the 20 °C case to 317.5 mm for the -20 °C case and then to 311.1 mm for the -60 °C case. As the temperature of the model wall decreases the boundary-layer height

decreases and the sonic line moves closer to the surface, thus increasing the Mack-mode frequency and increasing its destabilizing effect [75].

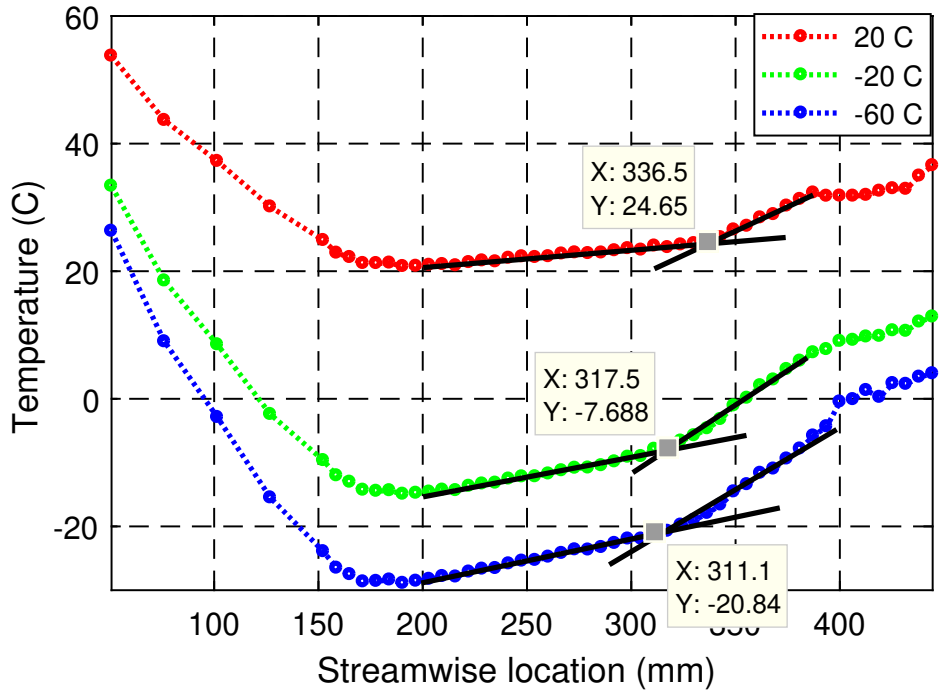

Figure 3.15: Temperature profiles on the cone with DREs at a unit Reynolds number of 9x10^6 /m with quantification of transition onset location.

The boundary layer was observed as the unit Reynolds number was swept from 8x10^6 /m to 11x10^6 /m. The recirculating chiller was set to coolant set points of 20 °C, -20 °C, and -60 °C. The temperature profiles at unit Reynolds numbers of 8, 9, 10, and 11 x10^6 /m have been plotted for each coolant set point. Fig. 3.16 shows the temperature profiles from the cone with DREs at coolant set point 20 °C. The onset of transition moves upstream as the Reynolds number increases and the heating also increases as the Reynolds number is increased. The locations can be quantified but drawing that many lines leaves the image hard to decipher and so the data have been presented qualitatively here. The temperature profiles at the aft end of the cone show the 8x10^6 /m and 9x10^6 /m profiles to be near identical. The temperature profile for the 10x10^6 /m unit Reynolds number profile shows an increase in heating. The 11x10^6 /m profile shows a significant increase in

temperature compared to the lower Reynolds numbers, indicating a fully turbulent boundary layer.

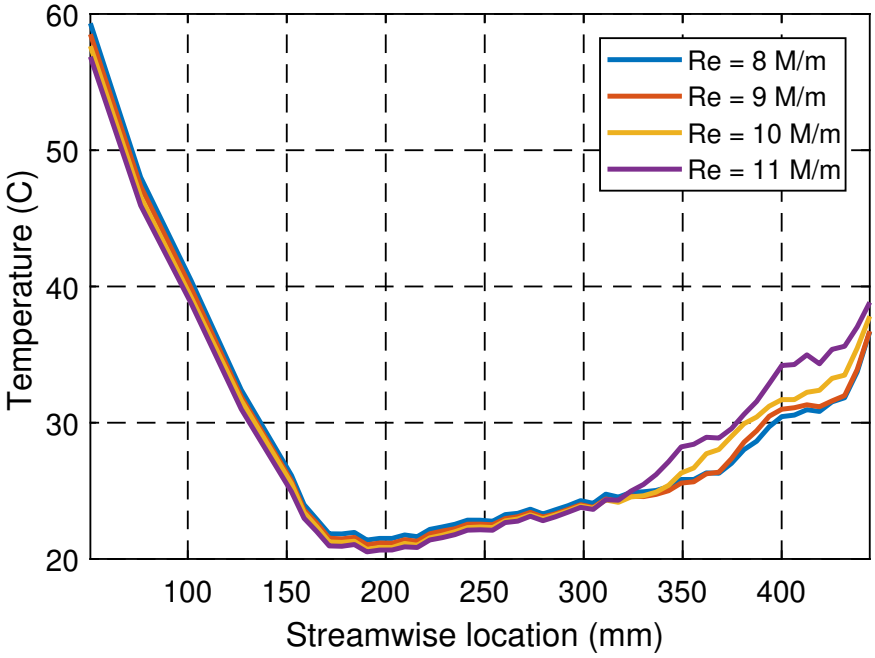

Figure 3.16: Temperature profiles over Reynolds number sweeps for the cone with DREs at 20 °C coolant set point.

The coolant temperature set point was set to -20 °C and the Reynolds number sweep repeated. The temperature profiles are shown in Fig. 3.17. The temperature profiles at unit Reynolds numbers of $8x10^6$ /m and $9x10^6$ /m are almost identical with the $9x10^6$ /m profile slightly hotter. The $10x10^6$ /m unit Reynolds number profile shows earlier onset of transition and higher heating at the aft end of the cone. The $11x10^6$ /m unit Reynolds number profile shows even higher heating.

Fig. 3.18 shows the temperature profiles at increasing unit Reynolds numbers as the Reynolds number is swept and the coolant set point is set to -60 °C. The $8x10^6$ /m and $9x10^6$ /m profiles are seen to be different for this case as the higher Reynolds number shows higher heating. This indicates the boundary layer is further destabilized than in the previous cases. The $10x10^6$ /m and $11x10^6$ /m unit Reynolds number profiles show earlier onset of transition and higher heating as Reynolds number is increased.

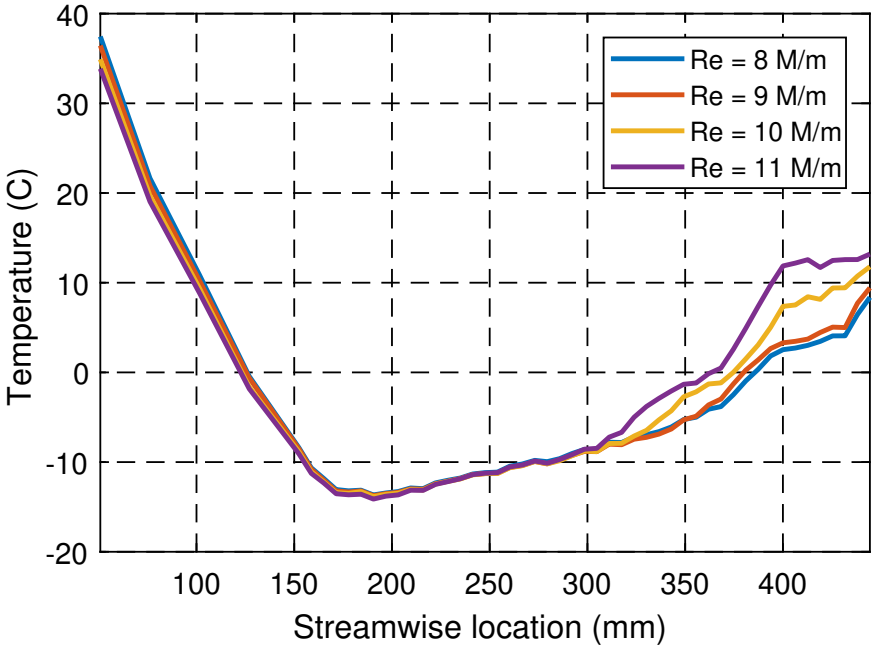

Figure 3.17: Temperature profiles over Reynolds number sweeps for the cone with DREs at -20 °C coolant set point.

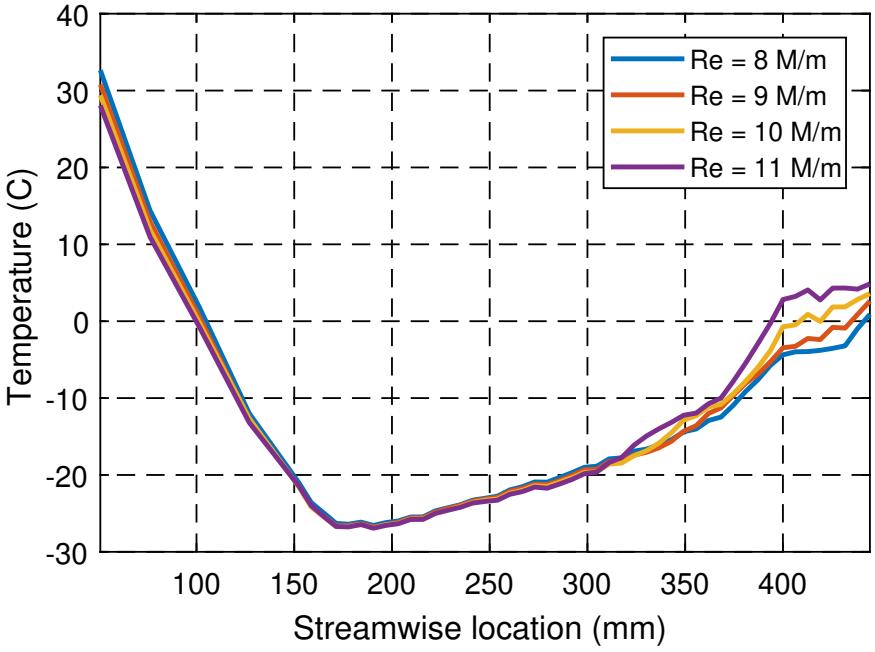

Figure 3.18: Temperature profiles over Reynolds number sweeps for the cone with DREs at -60 °C coolant set point.

3.3.2 Mack-mode instabilities

The Mack-mode instabilities on the cone with DREs have been studied using focusing schlieren as was done for the smooth cone. Focused Laser Differential Interferometry (FLDI) has recently been implemented at the NAL and has also been used to study the Mack-mode instability.

3.3.2.1 Focusing Schlieren

The focusing schliren system was setup with the high-speed camera (Photron FASTCAM SA-Z). The camera settings were identical to those used for the smooth cone, 1500 fps and 0.16 μs. These settings allow for the entirety of the cone outside the nozzle to be captured in the frame and an entire wind tunnel run to be recorded. Wind tunnel runs were done with the coolant set point at 20 °C, -20 °C, and -60 °C. The Reynolds number was increased from 7.5x10^6 /m to 11x10^6 /m for the wind tunnel runs where the camera was part of the diagnostic to observe the boundary layer on the aft end of the cone and its transition from laminar to turbulent. Fig. 3.19 shows the Mack-mode "rope-like" structures present in the boundary layer on the cone with DREs at a coolant set point of -60 °C. Again, this diagnostic was used as a qualitative tool to confirm presence of Mack-mode waves and confirm the boundary-layer transition trends seen from the other diagnostics. The uncertainties when defining transition using this diagnostic are too high for quantification to be useful. Qualitatively the Mack-mode instability was observed to have a wavelength indicating a frequency of $\sim$300 kHz as expected. The intermittency of breakdown of the boundary layer was seen to increase as the unit Reynolds number was increased and resulted in full breakdown to transition at the higher Reynolds numbers.

The high-speed camera was replaced with a fiber-optic coupled photodetector to make measurements at a point in the boundary layer. The photodetector is capable of far higher frequencies ($\sim$50 MHz) than the camera or the DAQ and can be used to analyze spectral data. The limitation in this case is the DAQ which has a maximum sampling rate of 2 MHz. The voltage data from the photodetector were sampled at 2 MHz and then Welch's method used to transform time-domain data to frequency-domain data. The segment size used was 2^8 and overlap was 50%. The reso-

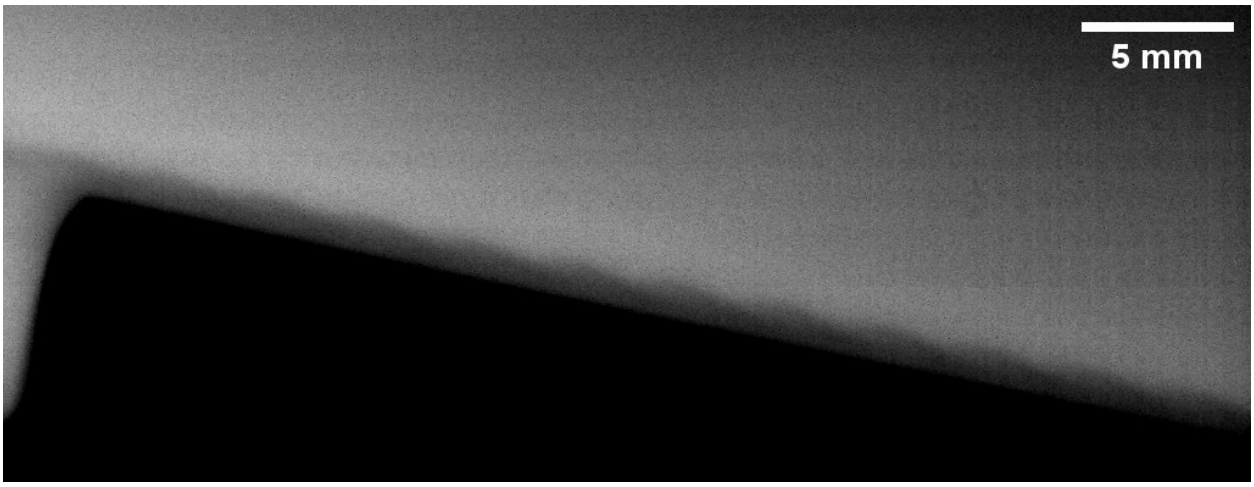

Figure 3.19: Focusing schlieren image on the aft end of the cone with DREs at coolant setpoint -60 °C.

lution of the spectral data was 7.8 kHz which translates to an uncertainty of ±3.9 kHz. The fiber optic was positioned to take data at a point in the boundary layer 25.4 mm from the aft end of the cone.

Fig. 3.20 shows the spectral data for the cone with DREs with the recirculating chiller set to 20 °C. The unit Reynolds number was swept from $8x10^6$ /m to $11x10^6$ /m. The frequency of the Mack-mode instability was observed to be 281.3±3.9 kHz at a unit Reynolds number of $8x10^6$ /m. As the Reynolds number increases the Mack-mode frequency increases as well. At a unit Reynolds number of $8.6x10^6$ /m the overall spectral energy is seen to increase and the peak gets smaller, this is presumed to be the onset of boundary-layer transition. As the Reynolds number is increased further the spectral energy rises and the Mack-mode peak is no longer seen at a unit Reynolds number of $9.7x10^6$ /m. The boundary layer is thought to be fully turbulent at this point. Note the differences from the smooth cone at the same temperature, the Mack-mode frequency is lower (289.1±3.9 kHz for the smooth cone), because the DREs have made the boundary-layer height increase. The rise in spectral energy($9.2x10^6$ /m for the smooth cone) and turbulence ($10.5x10^6$ /m for the smooth cone) are observed earlier as the DREs destabilise the boundary layer.

Fig. 3.21 shows the spectral data on the cone with DREs at coolant setpoint -20 °C as the unit

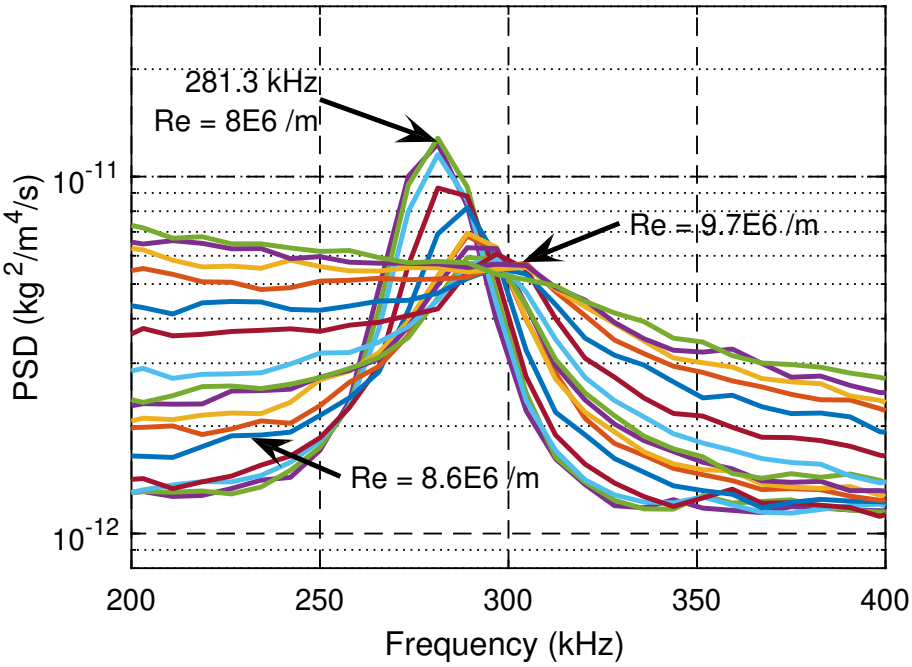

Figure 3.20: Spectral data from focusing schlieren on cone with DREs at coolant setpoint 20 °C.

Reynolds number is swept from 7.5x10^6 /m to 11x10^6 /m. The sweep was started at an earlier Reynolds number for this case because the spectral energy starts increasing earlier. For consistency the Mack-mode frequency at unit Reynolds number of 8x10^6 /m is shown, it is 289.1±3.9 kHz. This is lower than that for the smooth cone (296.9±3.9 kHz), again due to the boundary-layer height increasing from the DREs. The spectral energy is observed to increase at a unit Reynolds number of 8.2x10^6 /m as opposed to 9x10^6 /m for the smooth cone. The spectral energy increases and the Mack-mode peak is no longer observed at a unit Reynolds number of 9.2x10^6 /m as opposed to 9.8x10^6 /m for the smooth cone. The DREs again result in earlier transition.

Fig. 3.22 contains the spectral data obtained from the cone with DREs at coolant set point to -60 °C while the unit Reynolds number is swept from 7.5x10^6 /m to 11x10^6 /m. The Mack-mode frequency at a unit Reynolds number of 8x10^6 /m is observed to be 289.1±3.9 kHz as compared to 296.9±3.9 kHz for the smooth cone at the same coolant set point. The spectral energy is observed to increase at a unit Reynolds number of 8x10^6 /m as opposed to 8.8x10^6 /m for the smooth cone. The spectral energy increased and the Mack-mode peak was no longer observed at a unit Reynolds

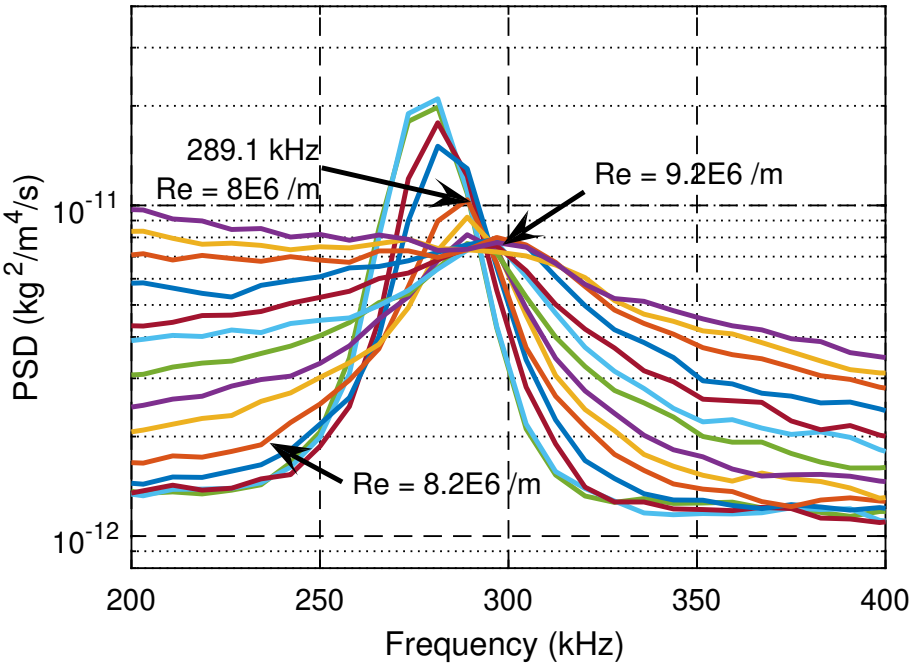

Figure 3.21: Spectral data from focusing schlieren on cone with DREs at coolant setpoint -20 °C.

number of 9x10^6 /m as opposed to 9.5x10^6 /m on the smooth cone.

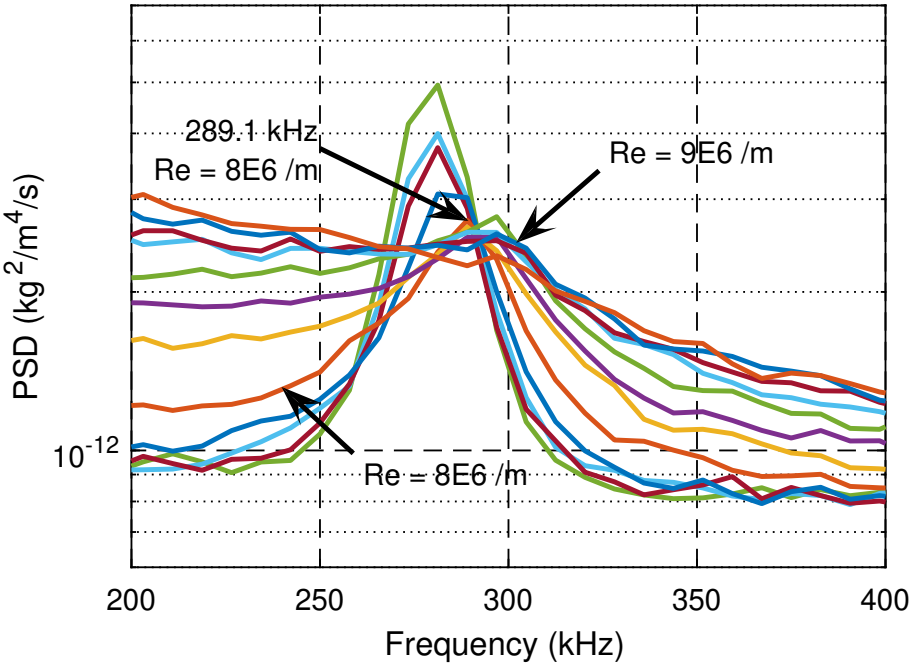

Figure 3.22: Spectral data from focusing schlieren on cone with DREs at coolant setpoint -60 °C.

3.3.2.2 FLDI

Focused Laser Differential Interferometry (FLDI) was used to study the Mack-mode instability on the 91-6 flared cone. The technique used here has been named Linear Array-Focused Laser Differential Interfereometry (LA-FLDI) owing to the multiple beam pairs that can be created and used to probe the flow. The diffractive optic being used for this work splits the laser beam into a 1x6 array but it is possible to split the beam into 2-D arrays using the right optic or by stacking optics that create 1-D arrays. The ability to simultaneously probe multiple points in a boundary layer using a non-intrusive diagnostic is very useful for studying hypersonic flows. In this case the linear array of beam pairs is being placed in the boundary layer either parallel or perpendicular to the model wall.

Initially the array of beam pairs was placed parallel to the model wall at a wall-normal height of 1 ± 0.5 mm and with the furthest-downstream beam 25.4 ± 0.5 mm from the aft end of the cone. Wind tunnel runs were done with the beam pairs in this orientation and the Reynolds number was increased from $8\text{x}10^6$ /m to $11\text{x}10^6$ /m. The LA-FLDI technique provides spectral data similar to the focusing schlieren technique. The data were sampled at 2 MHz as this was the highest the DAQ system was capable of. It should be noted that the photodetectors are capable of higher frequencies and the DAQ system is the limiting factor here. Future experiments may be able to use higher bandwidth data acquisition systems to analyze higher frequency content in the spectral data. Fig. 3.23 shows the spectral data from all 6 channels as the unit Reynolds number is swept up. At a unit Reynolds number of $8.2\text{x}10^6$ /m the Mack-mode peak is seen to have a frequency of $\sim$290 kHz and the harmonics of the Mack mode are seen as well. At a unit Reynolds number of $9.2\text{x}10^6$ /m the Mack-mode frequency has increased to $\sim$305 kHz and the frequency of the harmonics has increased too. At a unit Reynolds number of $10.2\text{x}10^6$ /m the boundary layer is transitional and the harmonics are no longer seen. The Mack mode is a diffuse peak and more importantly there is some separation between the spectral energy from the six channels. This indicates that the most upstream channel (channel 6) was transitioning later than the most downstream channel (channel 1). At a unit Reynolds number of $10.9\text{x}10^6$ /m a classic turbulence hump is observed in the spectra.

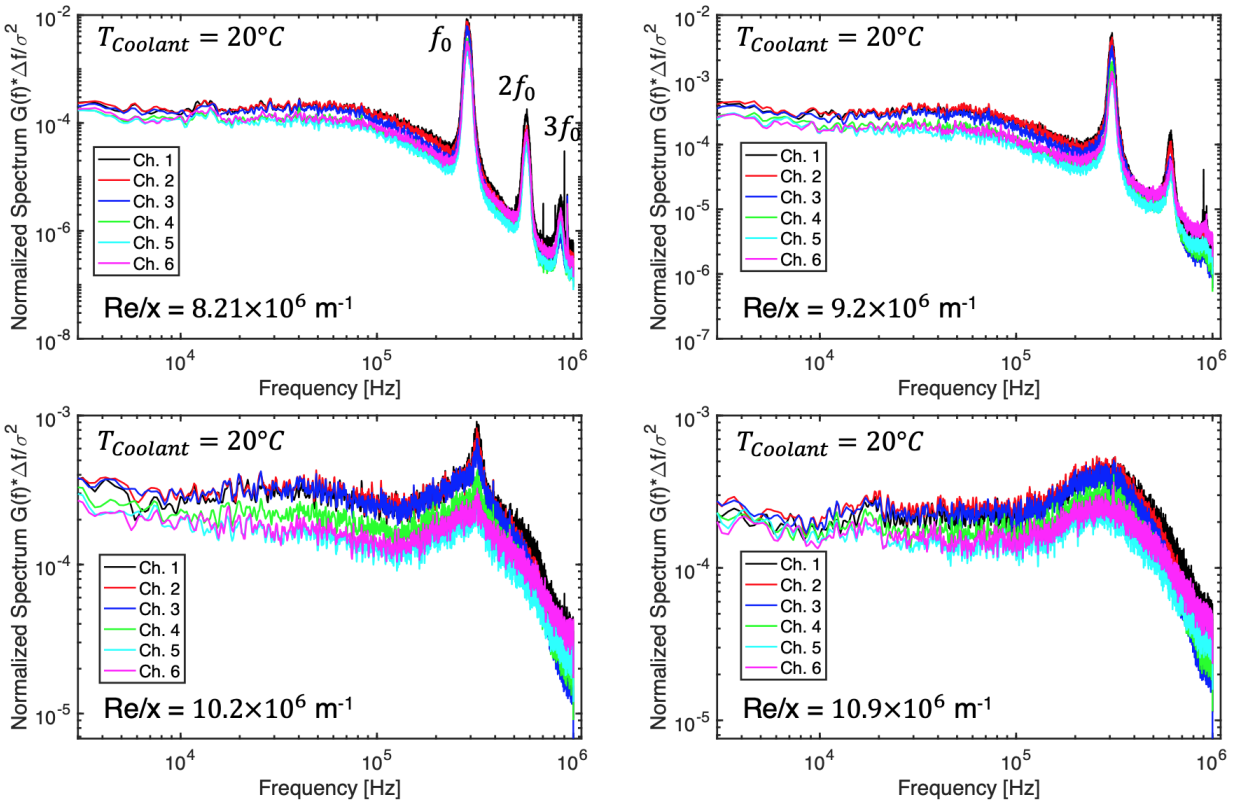

Figure 3.23: Spectral data obtained using the LA-FLDI diagnostic at six points in the boundary layer on the cone with DREs over the course of a Reynolds number sweep.

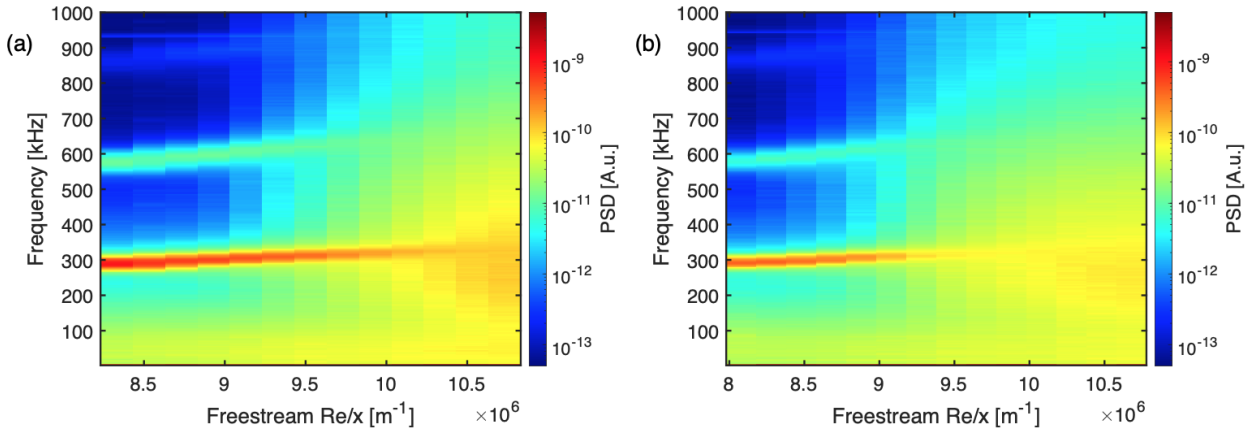

Figure 3.24: Spectral data in the form of colormaps over the course of a unit Reynolds number sweep on the cone with DREs. (a) Coolant temperature set point 20 °C, (b) Coolant temperature set point -20 °C.

The spectral data were plotted as colormaps to better understand trends as the Reynolds number was increased. Fig. 3.24 shows the colormaps showing the evolution of the Mack-mode instability and eventual disappearance as the boundary layer transitions to turbulence. The frequency of the Mack-mode and its harmonics increase as the Reynolds number is increased. For the coolant set point of 20 °C the Mack-mode instability diffuses and cannot be ascertained after a unit Reynolds number of 10.2x10^6 /m. For the -20 °C case the Mack-mode instability cannot be ascertained past a unit Reynolds number of 9.2x10^6 /m, indicating earlier transition.

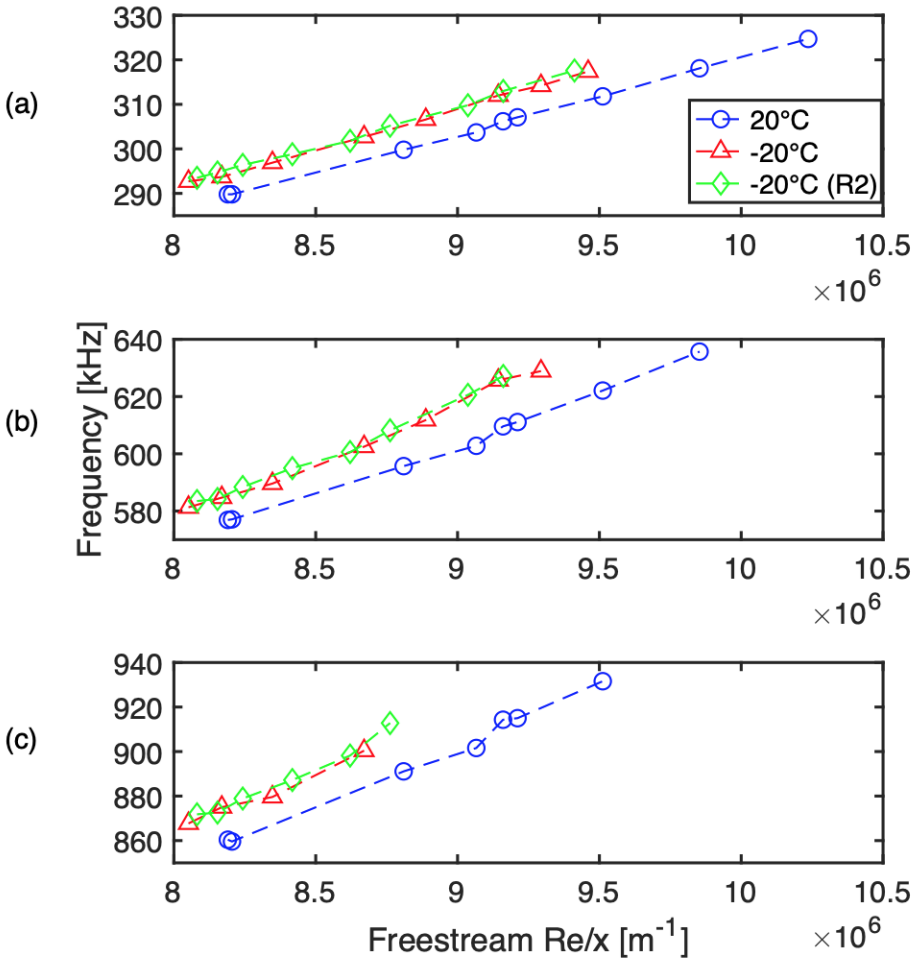

Figure 3.25: Peaks of the Mack-mode instability and its harmonics plotted separately over the course of a unit Reynolds number sweep for different coolant set points at Channel 1. (a) Mack-mode frequency, (b) its first harmonic, and (c) its second harmonic.

For better quantification the peaks of the Mack-mode instability and its harmonics were plotted separately as Reynolds number is increased for the two coolant set points, the result can be seen in Fig. 3.25. The Mack-mode frequency and the harmonics are seen to be higher when the coolant set point is decreased due to the boundary-layer height decreasing and causing the sonic line to get closer to the model wall. The harmonics also disappear much earlier than the Mack-mode peaks, but the detection of two harmonics proves that this is a very sensitive diagnostic.

The orientation of beam pairs was rotated 90° to be in a straight line normal to the model wall. In this orientation the beam pairs would be able to study the boundary layer profile instead of being equidistant from the model. The diffractive optical element (DOE) was adjusted to contract the spacing between beam pairs so more points could be in the boundary layer. The wall-normal orientation of the beam pairs is shown in Fig. 3.26. The lowest beam pair was placed so as to mark the wall location, and then the location of the other beam pairs was determined using beam-profiler imaging.

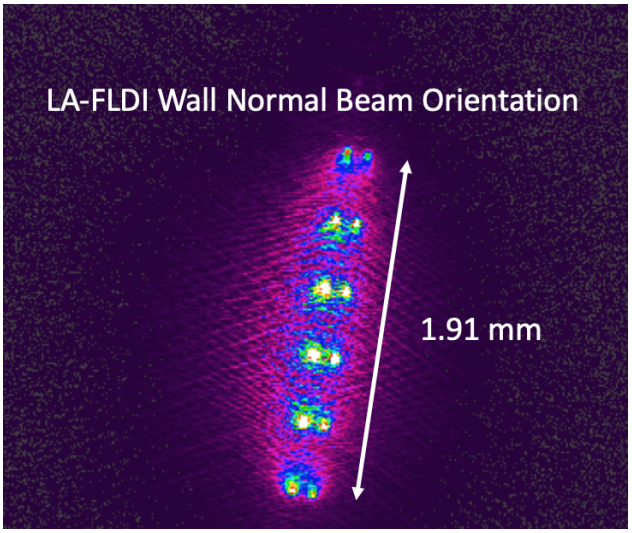

Figure 3.26: Beam profile of the beam pairs in wall-normal orientation for boundary-layer profile analysis.

A Reynolds number sweep was carried out with the coolant set point at 20 °C on the cone with

DREs. The data collected were converted to the frequency domain and plotted. The point closest to the wall was eclipsed by the model and the point furthest away showed no content due to being outside the boundary layer. Thus the four points in the middle have been analyzed and the spectral data plotted in a colormap, as seen in Fig. 3.27. The Mack-mode instability and its harmonics are observed at wall-normal distances of 0.38 mm, 0.76 mm, and just barely for the 1.14 mm. At 1.52 mm from the wall there is no content and this confirms that the spectral content seen for the lower points is present in the boundary layer and is not some effect of tunnel noise.

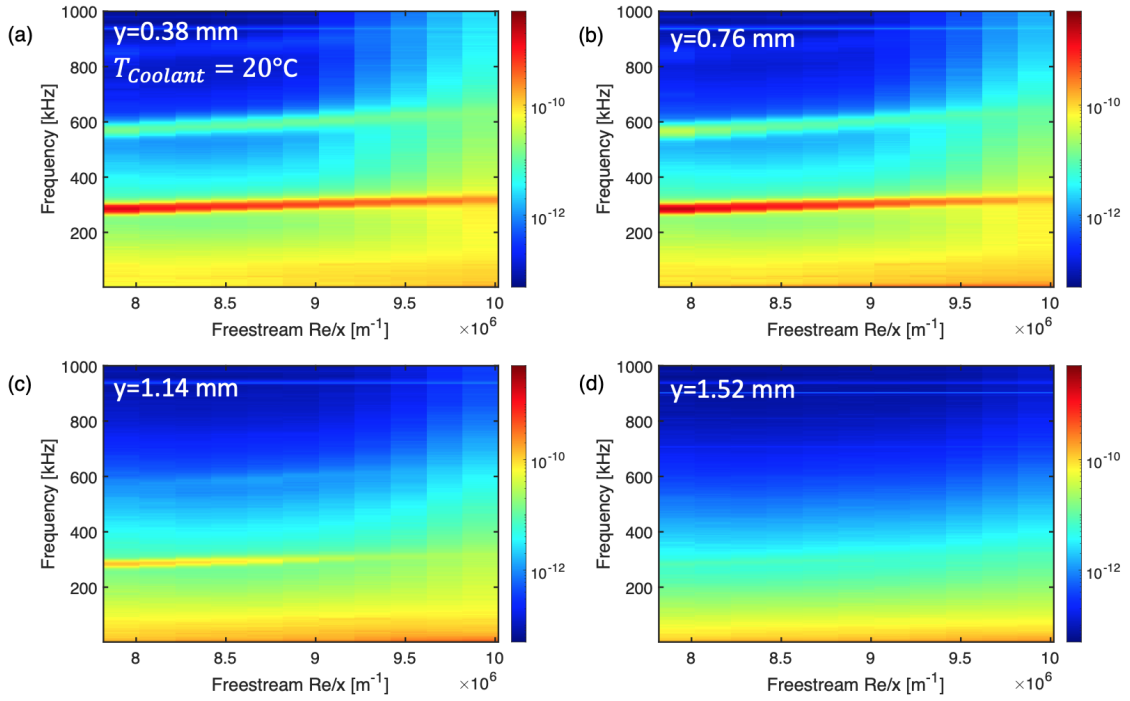

Figure 3.27: Spectral data from channels 2-5 of the LA-FLDI setup with wall-normal orientation over the course of a unit Reynolds number sweep on the cone with DREs. Coolant set point at 20 °C.

3.3.3 Görtler instabilities

The Görtler instability is present in the boundary layer whenever there is concave curvature and contributes to boundary-layer transition. The Görtler instability is a 3-D, axially-growing, sta-

tionary structure and thus has to be probed spanwise along with making streamwise measurements such as those with focusing schlieren and FLDI. Constant Temperature Anemometry (CTA) was used in the form of a hot-film probe to map the boundary layer over the aft end of the cone. The stationary voltage output of the anemometer can be used to represent the mass flux to qualitatively study spatially-growing variations in the boundary layer.

The map was created in a plane parallel to the nozzle exit and 35$\pm$0.5 mm from the aft end (422.2$\pm$0.5 mm from the tip) of the cone. The data were sampled at 500 kHz for 100 ms at each point. The hot-film probe was traversed in 0.5° steps to do azimuthal sweeps from 80° to 101° using a conventional cylindrical coordinate system. Only one sweep could be accomplished in one wind tunnel run and thus several wind tunnel runs were carried out at the same flow condition to create the map. The step size for the sweep on the cone with DREs was half what it was on the smooth cone to better capture the structure of the Görtler instability. The range was also increased slightly from 20° to 21° to fully capture the last peak. The distance of the sensor from the surface was estimated by placing the sensor very close to the model and taking images. The images were processed using known distances like dimensions of the probe holder to estimate the wall-normal distance of the probe from the model surface.

Fig. 3.28 shows the map of voltage variations created from data collected over several wind tunnel runs. The coolant set point 20 °C case is shown in Fig. 3.28a and shows some structure and periodicity. Fig. 3.28b shows more definition and a periodicity of peaks every 4° can be seen. The boundary layer is also seen to decrease in thickness with the lower wall temperature. Fig. 3.28c shows the variations captured using the hot-film sensor over the cone with DREs at a coolant set point of -60 °C. The boundary-layer height is seen to decrease further and the structure of the Görtler vortices is seen to be stronger. The periodicity is again seen to be every 4° which equates to a wavenumber of 90. As for the smooth cone case, it can be concluded that wall cooling decreases boundary-layer height and makes the Görtler instability more structured. It can also be said that adding DREs at the observed Görtler wavenumber on the smooth cone had an organizing effect on the Görtler vortices observed on the cone with DREs.

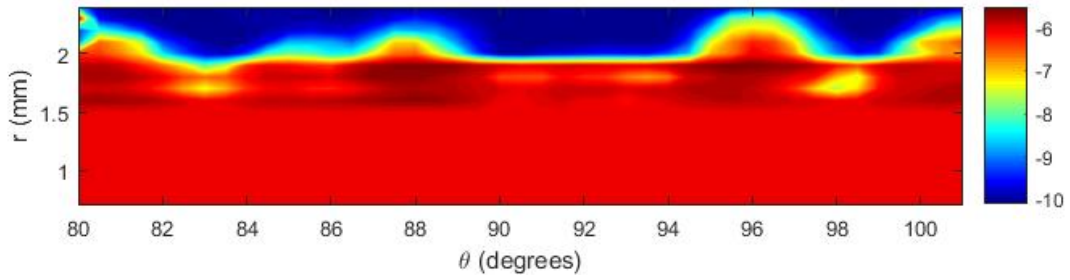

(a) Coolant set point 20 °C

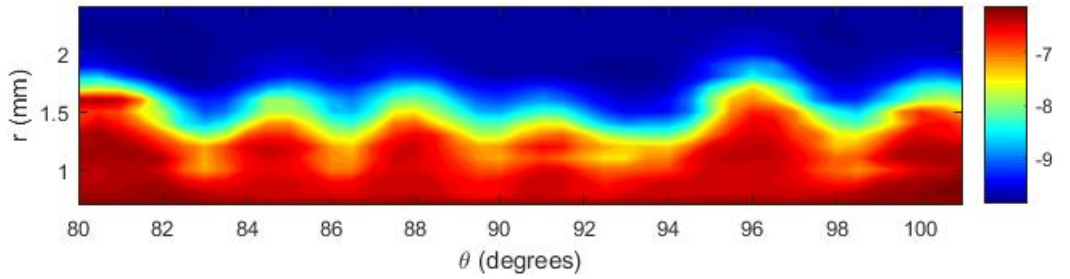

(b) Coolant set point -20 °C

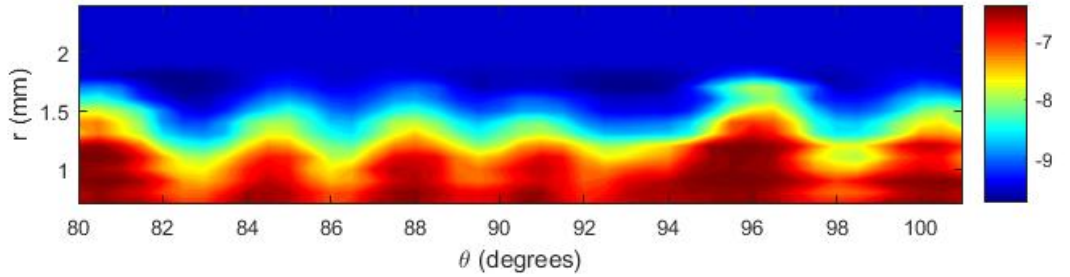

(c) Coolant set point -60 °C

Figure 3.28: Hot-film voltage variation over a 21° azimuthal sweep on the cone with DREs at a unit Reynolds number of 9x10^6 /m.

3.4 Computational work

Data Parallel Line Relaxation (DPLR) is a hypersonic Computational Fluid Dynamics (CFD) code developed by NASA. DPLR was used to compute a laminar, disturbance-free basic state. The flow conditions of the M6QT were used at a unit Reynolds number of 10x10^6 /m. The model wall temperature was the same as that recorded on the 91-6 cone when the coolant set point was at 20 °C. The tip was assumed to be at the adiabatic wall temperature ($\sim$380 K) and then wall temperature was extrapolated to the first thermocouple position at 50.8 mm.

Euonymous Parabolized Instability Code (EPIC) is a boundary-layer stability code developed in-house at the Texas A&M University Computational Stability & Transition (CST) lab and uses Linear Stability Theory (LST), Linear Parabolized Stability Equations (LPSE), and Non-linear Parabolized Stability Equations (NPSE) to analyze boundary-layer instabilities. EPIC uses grid clustering to better capture boundary layers and shock development. EPIC uses LST to initialize marching solutions and then marches LPSE and NPSE solutions along predefined paths.

For the smooth 91-6 flared cone, a single straight path was extracted from the basic state. The LPSE capability of EPIC was then used to determine the most unstable frequency of the Mack-mode instability and the most unstable wavenumber of the Görtler instability. LPSE was used instead of LST to accurately capture the flow features caused by the geometry and conditions. The smooth cone case has been used for the computations and the wall temperature mimics that on the cone when coolant set point is 20 °C.

Fig. 3.29 shows the most unstable frequency of the Mack-mode instability to be 300 kHz, reaching an N-factor of $\sim$19. The frequency matches very well the Mack-mode frequency observed from the focusing schlieren and FLDI measurements. Fig. 3.30 shows the most unstable wavenumber of the Görtler instability to be 90, reaching an N-factor of $\sim$4.8 at the aft end of the cone. Again this matches very well with the 4° periodicity seen in the anemometry data collected using hot film probes.

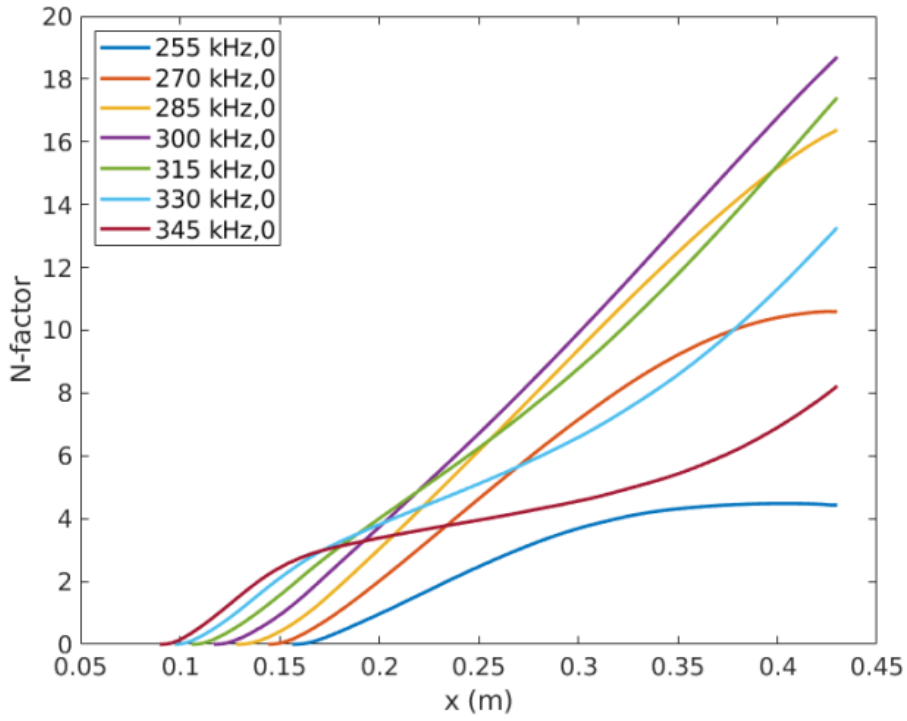

Figure 3.29: CFD results showing the most unstable frequency of the Mack-mode instability on the smooth cone at coolant set point 20 °C.

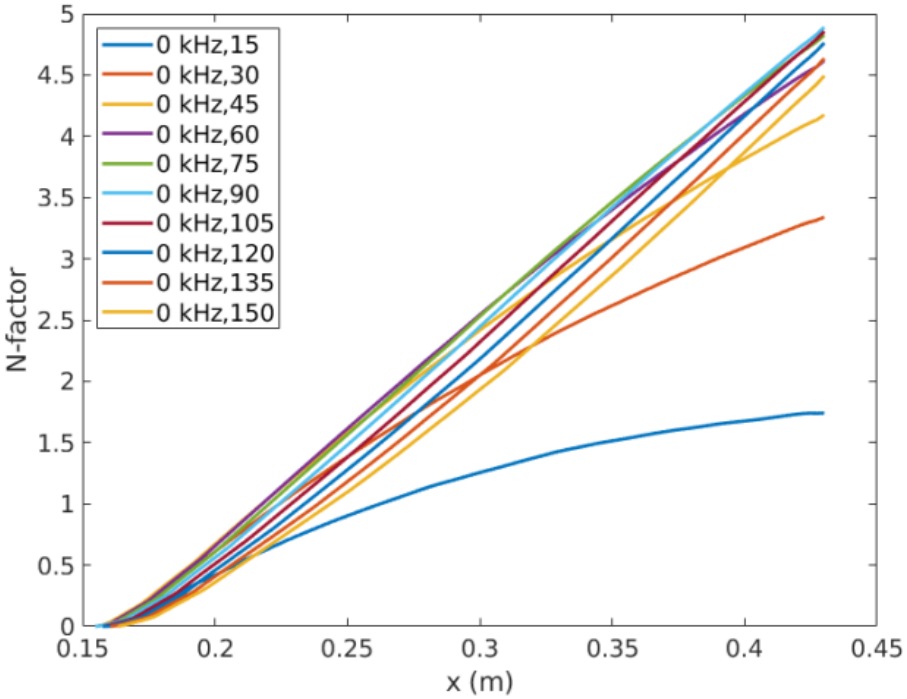

Figure 3.30: CFD results showing the most unstable wavenumber of the Görtler instability on the smooth cone at coolant set point 20 °C.

4. SUMMARY AND CONCLUSIONS

4.1 Summary

Hypersonic boundary-layer transition is an important consideration in the design of hypersonic vehicles, missiles, and re-entry vehicles. One of the most important problems is the large heat transfer to the vehicle that occurs at high speeds. This heating can increase by an order of magnitude when the boundary layer transitions from laminar to turbulent. Thus it is important to understand how and why this transition process occurs.

The governing equations of the flow are the Navier-Stokes equations which are very complex and nonlinear, making them hard to solve. They can be simplified by making assumptions and introducing similarity parameters. Linear Stability Theory writes the equations in terms of disturbance quantities with parallel-flow basic states that makes them easier to solve. The e^N method is a semi-empirical way to predict transition location for 2-D incompressible flows, it is also used for 3-D compressible flows, albeit cautiously and with caveats. The Mack mode is a 2-D inviscid instability, it is the dominating cause of transition at hypersonic speeds. The Görtler instability manifests in the form of streamwise-oriented, counter-rotating vortices when concave curvature is present. These vortices can cause earlier transition of the boundary layer. Receptivity is the process by which external disturbances in the flow make the laminar boundary layer transition to turbulence. The process the boundary layer undergoes as it transitions from laminar to turbulent is different depending on the amplitude of external disturbances and this was discussed in detail.

Many experiments have been done to study the stability of hypersonic boundary layers, the experiments relevant to this work were discussed. The experiments done by Blanchard and Selby [67] using the same model in the same nozzle were discussed and used to guide experiments. Hofferth [2] and Craig [8] carried out experiments with cone models in the M6QT and their findings were discussed as well. The objectives of this experiment were to study the transition caused by Mack-mode and Görtler instabilities. Computational work was done by another group and the

experimental data were used as validation data.

All experiments were conducted in the M6QT on the 91-6 flared cone. The M6QT is a quiet wind tunnel with an operating Mach number of 5.9 and a maximum run time of 40 seconds. The 91-6 cone is a flared cone with embedded thermocouples and active cooling, a recirculating chiller outside the test section continuously cools and pumps coolant through the cone. The experiments were carried out first on the smooth cone and then DREs added and experiments repeated. The diagnostics used were temperature profiles, hot-film anemometry, focusing schlieren, and focused laser differential interferometry (FLDI).

Wind tunnel runs were done with the coolant set points set to 20 °C, -20 °C, and -60 °C. The unit Reynolds number was held constant at $9x10^6$ /m. Analysis of the temperature profiles obtained from the embedded thermocouples showed an earlier increase in heating for the cases with lower wall temperature. This is in agreement with previous experiments that show increased destabilization with lower wall temperature due to a decrease in boundary-layer height causing higher frequencies of the Mack-mode instability. This trend was observed for both the smooth cone and the cone with DREs and has been quantified for both cases. Comparing the smooth cone and cone with DREs at the same coolant set points, earlier heating is observed for the cone with DREs due to the destabilizing effect of the DREs. The temperature profiles were also analyzed over the course of a Reynolds number sweep for the same three coolant set points on the smooth cone and the cone with DREs. Earlier heating was observed for all profiles for the higher Reynolds numbers. For the smooth cone case the temperature profiles were near identical at the aft end of the cone for unit Reynolds numbers of $8x10^6$ /m and $9x10^6$ /m. An increase in heating was observed for the $10x10^6$ /m profile and another increase for the $11x10^6$ /m profile as the boundary layer transitioned to turbulence. For the cone with DREs similar trends were observed except for the unit Reynolds number of $9x10^6$ /m profile at coolant setpoint -60 °C where higher heating was seen compared to the smooth cone profile signifying earlier transition of the boundary layer.

Focusing schlieren was used to visualize the structure of the Mack-mode instability in the boundary layer using a camera. Spectral data were also collected and showed peaks ranging from

$\sim$280 to $\sim$320 kHz. The frequencies were seen to increase as Reynolds number was increased due to a decrease in boundary-layer height. An increase was seen in the spectral energy at certain Reynolds numbers and grew till the Mack-mode peak was no longer seen, this was considered a turbulent boundary layer. For the smooth cone and cone with DREs the spectral energy was observed to increase at lower Reynolds numbers for lower wall temperatures. The Mack-mode peak also disappeared at lower Reynolds numbers as the wall temperature was decreased. The Mack-mode frequencies were observed to be lower in general for the cone with DREs due to a higher boundary-layer height caused by the DREs. The cone with DREs was also observed to be more unstable as the increase in spectral energy and disappearance of Mack-mode peak were observed at earlier Reynolds numbers for the same wall temperatures.

Hot-film anemometry was used to map the uncalibrated voltages from the anemometer to study mass-flux variation on a 20° azimuthal span at the aft end of the cone. The same three coolant set points were used again and the unit Reynolds number held constant at $9\text{x}10^6$ /m. The maps created showed peaks every 4° for the smooth cone and the cone with DREs. The structure became more prominent and the height of the boundary layer was observed to decrease for the lower wall temperatures. The boundary-layer height was observed to be higher for the cone with DREs than for the smooth cone, in agreement with the focusing schlieren data. These peaks were assumed to be from Görtler vortices caused by the flare and this was confirmed by computational work.

The FLDI diagnostic was only used for the cone with DREs as it is a new diagnostic at the NAL and was not available when the smooth cone experiments were done. The cone currently has DREs on it and further experiments are planned so it has been left as it is. Removing DREs and reapplying them is also a risky endeavor on the very delicate model. FLDI was used to probe six linear points (streamwise) in the boundary layer simultaneously. Spectral data were obtained and the Mack-mode instability and two harmonics documented. Unit Reynolds number sweeps were done and the spectral data showed boundary-layer transition as the Reynolds number was increased. Two coolant set points were studied with the FLDI diagnostic, 20 °C and -20 °C. Earlier transition was seen on the colder wall case and analyzed using color maps. The harmonics

of the Mack-mode instability were also observed to wash out earlier for the lower wall temperature case. The array of beam pairs was rotated to be wall normal and data collected. The Mack-mode peaks were observed in the boundary layer but not seen when further away from the wall. This demonstrated that the peaks seen are present in the boundary layer and not an effect of tunnel noise or something else.

Computations were carried out using the EPIC boundary-layer stability code with a temperature distribution to match that of the 20 °C coolant set point and a unit Reynolds number of $10x10^6$ /m. The LPSE results showed the most unstable Mack-mode frequency to be 300 kHz and the most unstable wavenumber of the Görtler instability to be 90. These results are in good agreement with the experimental data.

4.2 Conclusions

The boundary layer on a sharp-tip flared cone has been investigated at different wall temperatures and at varying Reynolds numbers. Several diagnostics have been used to probe the flow and the results have been discussed in detail. The significant conclusions from this experiment are listed below.

1. Wall cooling leads to boundary-layer transition on a sharp-tip flared cone. Previous experiments with similar geometries and adiabatic walls did not show transition, even with added roughness.

2. Increased wall cooling destabilizes the boundary layer at lower Reynolds numbers, observed by tracking wall temperature on the model.

3. Adding roughness in conjunction with wall cooling further destabilizes the boundary layer.

4. The Mack-mode instability is present in the boundary layer and has been visualized. Its frequency ranges from 280-320 kHz depending on Reynolds number, wall temperature, and the presence of DREs.

5. Wall cooling destabilizes the Mack-mode instability, as seen in the spectral data from focusing schlieren, causing an earlier increase in spectral noise and transition.

6. The Görtler instability is present in the boundary layer and has been documented using anemometry and verified by computations. This is the first revelation of Görtler vortices on flared cones to the authors best knowledge.

7. The Mack-mode instability has harmonics and two of them have been documented using FLDI. The boundary layer has also been probed at six points simultaneously. The destabilization of the boundary layer caused by wall cooling was confirmed.

8. Computations showed good agreement with the experimental data and will be using these data to help guide future studies.

9. The Mack-mode (2-D) and Görtler (3-D) instabilities have been demonstrated to co-exist in the boundary layer and contribute to boundary-layer transition.This paves the way for further study of interaction of these instabilities to cause a Klebanoff-type oblique breakdown.

4.3 Future Work

Boundary-layer stability is and has been a rich area of study. The numerous instabilities and their interactions are not fully understood and there is a lot more work to be done. For this experiment specifically there are a few things that can be done.

1. Measuring growth rates of the Mack-mode instability

   FLDI provides multi-point measurements along a streamwise line in the boundary layer. Growth rates of the Mack-mode instability can be found with carefully designed and executed experiments. This can be attempted with a new diffractive optic with greater separation angle. If no discernible growth is observed, two separate and complete FLDI systems may be used to make measurements further apart on the model to quantify growth of the instability.

2. Improving the FLDI diagnostic

   The data were collected for this work using the UTSI setup. A similar setup is now in place that was built in-house at Texas A&M. The new system uses Wollaston prisms instead of a diffractive optic element (DOE) to split the laser beam. This creates four beam pairs instead of six with the DOE but provides increased flexibility in orientation of the beam pairs. A DOE for this system has also been ordered. Experiments should be conducted using both methods of splitting the beam and the differences analyzed. More advanced beam-pair patterns can be created, such as 2-D arrays, but the DAQ system then becomes the limiting factor. It would be worthwhile to upgrade the DAQ systems so more channels can be sampled simultaneously. Acquiring a DAQ that can sample at higher rates than the current 2 MHz would also allow for spectral data to be analyzed to higher frequencies, which may show higher harmonics and other interactions. The FLDI diagnostic can also be modified by using different lenses and used on other wind tunnel facilities at the NAL.

3. Calibrating anemometry sensors

   Calibration of sensors would provide actual pressure fluctuations in the flow instead of voltage fluctuations. It is possible to calibrate them in the wind tunnel but this strategy requires several assumptions, data extrapolation, and risks damaging the sensor. Ideally, a dedicated calibration facility would be built to calibrate each sensor before use in the wind tunnel.

4. Future model design

   The 91-6 cone model is a very sophisticated model and has provided great insight into the transition process. There are several lessons to be learned from the design of this model, especially regarding the embedded instrumentation and design of cooling apparatus. Some improvements can be made to make it easier to place roughness on the model, the tip can be made bigger and with a key insert, this would accommodate different tips with roughness when needed instead of trying to adhere roughness to the surface. Machining tips with roughness would open up many new opportunities for the configuration of DREs.

5. Model alignment tool

   An axisymmetric model can be designed with PCB sensors around the span in the same streamwise location. This could be used to align the mounting apparatus with the nozzle. Then the only uncertainty would be the machining tolerance of models. In general, models are machined with very small tolerances in terms of how square they are. This would pay dividends for every campaign carried out in the M6QT.

6. Infrastructure issues

   There have been several periods over the last few years where the wind tunnels are down for maintenance due to some part being defective and waiting for a new part to come in. Some of this has been mitigated by ordering extra parts for components that are known to fail. It would be better to have some sort of maintenance schedule for all the infrastructure. If there is a list of all parts and their life cycles, then preventative maintenance could be performed when experiments are slow or during scheduled downtime instead of unexpected failures in the middle of testing campaigns. This will no doubt be a laborious task but would pay dividends in the long run.

REFERENCES

[1] J. D. Anderson, "Hypersonic and high temperature gas dynamics," *AIAA Education Series*, pp. 13–23, 2006.

[2] J. W. Hofferth, *Boundary-Layer Stability and Transition on a Flared Cone in a Mach 6 Quiet Wind Tunnel*. PhD thesis, Texas A&M University, College Station, TX, 2013.

[3] J. M. Floryan and W. S. Saric, "Stability of Gortler vortices in boundary layers," *AIAA journal*, vol. 20, no. 3, pp. 316–324, 1982.

[4] J. W. Hofferth, R. A. Humble, D. C. Floryan, and W. S. Saric, "High-bandwidth optical measurements of the second-mode instability in a Mach 6 quiet tunnel," *AIAA 2013-0378*, 2013.

[5] M. Gragston, T. J. Price, K. Davenport, J. D. Schmisseur, and Z. Zhang, "An m by n FLDI array for single-shot multipoint disturbance measurements in high-speed flows," in *AIAA Scitech 2021 Forum*, p. 0599, 2021.

[6] M. Gragston, F. Siddiqui, and J. D. Schmisseur, "Detection of second-mode instabilities on a flared cone in Mach 6 quiet flow with linear array focused laser differential interferometry," *Experiments in Fluids*, vol. 62, no. 4, pp. 1–12, 2021.

[7] T. S. Kocian, *Computational hypersonic boundary-layer stability and the validation and verification of EPIC*. PhD thesis, 2018.

[8] S. A. Craig, *Stability of High-Speed, Three-Dimensional Boundary layers*. PhD thesis, Texas A&M University, College Station, TX, 2015.

[9] T. C. Lin, "Influence of laminar boundary-layer transition on entry vehicle designs," *Journal of Spacecraft and Rockets*, vol. 45, no. 2, pp. 165–175, 2008.

[10] J. D. Schmisseur and P. Erbland, "Introduction: Assessment of aerothermodynamic flight prediction tools through ground and flight experimentation," *Progress in Aerospace Sciences*, vol. 48-49, pp. 2 – 7, 2012.

[11] S. P. Schneider, "Hypersonic laminar–turbulent transition on circular cones and scramjet forebodies," *Progress in Aerospace Sciences*, vol. 40, no. 1, pp. 1 – 50, 2004.

[12] L. M. Mack, "Boundary-layer linear stability theory," *AGARD*, vol. Rep. No. 709, 1984.

[13] D. W. Dunn and C.-C. Lin, "On the stability of the laminar boundary layer in a compressible fluid," *Journal of the Aeronautical Sciences*, vol. 22, no. 7, pp. 455–477, 1955.

[14] H. L. Reed, W. S. Saric, and D. Arnal, "Linear stability theory applied to boundary layers," *Annual review of fluid mechanics*, vol. 28, no. 1, pp. 389–428, 1996.

[15] L. Lees and C.-C. Lin, *Investigation of the stability of the laminar boundary layer in a compressible fluid*. No. 1115, National Advisory Committee for Aeronautics, 1946.

[16] A. Smith and N. Gamberoni, "Transition, pressure gradient and stability theory," *Report ES-26388, Douglas Aircraft Company, Long Beach, CA*, 1956.

[17] J. Van Ingen, "A suggested semi-empirical method for the calculation of the boundary layer transition region," *Technische Hogeschool Delft, Vliegtuigbouwkunde, Rapport VTH-74*, 1956.

[18] M. Morkovin and E. Reshotko, "Dialogue on progress and issues in stability and transition research," in *Laminar-Turbulent Transition*, pp. 3–29, Springer, 1990.

[19] W. S. Saric, "Görtler vortices," *Annual Review of Fluid Mechanics*, vol. 26, no. 1, pp. 379–409, 1994.

[20] P. G. Drazin and W. H. Reid, *Hydrodynamic stability*. Cambridge university press, 2004.

[21] G. I. Taylor, "Viii. stability of a viscous liquid contained between two rotating cylinders," *Philosophical Transactions of the Royal Society of London. Series A, Containing Papers of a Mathematical or Physical Character*, vol. 223, no. 605-615, pp. 289–343, 1923.

[22] W. R. Dean, "Fluid motion in a curved channel," *Proceedings of the Royal Society of London. Series A, Containing Papers of a Mathematical and Physical Character*, vol. 121, no. 787, pp. 402–420, 1928.

[23] H. Görtler, "Further development of a boundary layer profile for a given pressure distribution," *The Aeronautical Journal*, vol. 45, no. 362, pp. 35–50, 1941.

[24] I. Beckwith, M. Malik, F.-J. Chen, and D. Bushnell, "Effects of nozzle design parameters on the extent of quiet test flow at mach 3.5," in *Laminar-Turbulent Transition*, pp. 589–600, Springer, 1985.

[25] F.-J. Chen, M. Malik, and I. Beckwith, "Instabilities and transition in the wall boundary layers of low-disturbance supersonic nozzles," in *18th Fluid Dynamics and Plasmadynamics and Lasers Conference*, p. 1573, 1985.

[26] J. Floryan, "On the Görtler instability of boundary layers," *Progress in Aerospace Sciences*, vol. 28, no. 3, pp. 235–271, 1991.

[27] H. Peerhossaini and J. Wesfreid, "On the inner structure of streamwise Görtler rolls," *International journal of heat and fluid flow*, vol. 9, no. 1, pp. 12–18, 1988.

[28] H. Peerhossaini and J. Wesfreid, "Experimental study of the Taylor-Görtler instability," in *Propagation in Systems far from Equilibrium*, pp. 399–412, Springer, 1988.

[29] A. Nayfeh, S. Ragab, and A. Al-Maaitah, "Effect of roughness on the stability of boundary layers," in *4th Joint Fluid Mechanics, Plasma Dynamics and Lasers Conference*, p. 1044, 1987.

[30] P. Hall and S. Seddougui, "On the onset of three-dimensionality and time-dependence in Görtler vortices," *Journal of Fluid Mechanics*, vol. 204, pp. 405–420, 1989.

[31] M. Malik and M. Hussaini, "Numerical simulation of interactions between Görtler vortices and Tollmien–Schlichting waves," *Journal of Fluid Mechanics*, vol. 210, pp. 183–199, 1990.

[32] A. Federov and A. Tumin, "High-speed boundary-layer instability: Old terminology and a new framework," *AIAA Journal*, vol. 49, no. 8, pp. 1647–1657, 2011.

[33] M. V. Morkovin, E. Reshotko, and T. Hebert, "Transition in open flow systems: a reassessment," *Bull. APS.*, vol. 39, no. 9, pp. 1–31, 1994.

[34] W. S. Saric, H. L. Reed, and E. J. Kerschen, "Boundary-layer receptivity to freestream disturbances," *Ann. Rev. Fluid Mech.*, vol. 34, pp. 291–319, 2002.

[35] D. Arnal, "Boundary layer transition: predictions based on linear theory," *In AGARD*, 1994.

[36] E. Reshotko, "Transient growth: a factor in bypass transition," *Physics of Fluids*, vol. 13, no. 5, pp. 1067–1075, 2001.

[37] M. V. Morkovin, "On the many faces of transition," in *Viscous drag reduction*, pp. 1–31, Springer, 1969.

[38] M. V. Morkovin, "Bypass-transition research: issues and philosophy," in *Instabilities and Turbulence in Engineering Flows*, pp. 3–30, Springer, 1993.

[39] G. B. Schubauer and H. K. Skramstad, "Laminar boundary-layer oscillations and stability of laminar flow," *Journal of the Aeronautical Sciences*, vol. 14, no. 2, pp. 69–78, 1947.

[40] A. Demetriades, "An experimental investigation of the stability of hypersonic laminar boundary layer," *Journal of the Aerospace Sciences*, vol. 25, no. 9, pp. 599–600, 1958.

[41] A. Demetriades, "An experiment on the stability of hypersonic laminar boundary layers," *Journal of Fluid Mechanics*, vol. 7, no. 3, pp. 385–396, 1960.

[42] J. Kendall, "Supersonic boundary layer stability experiments," in *Boundary Layer Transition Study Group Meeting*, vol. 2, pp. 10–1, WD McCauley. Aerospace Corporation, Air Force Report No. BSD-TR-67–213, 1967.

[43] A. Demetriades, "Hypersonic viscous flow over a slender cone. iii-laminar instability and transition," in *7th Fluid and PlasmaDynamics Conference*, p. 535, 1974.

[44] J. M. Kendall, "Wind tunnel experiments relating to supersonic and hypersonic boundary-layer transition," *Aiaa Journal*, vol. 13, no. 3, pp. 290–299, 1975.

[45] A. Demetriades, "Laminar boundary layer stability measurements at Mach 7 including wall temperature effects," tech. rep., Ford Aerospace and Communications Corp, Newport Beach, CA, Aeronutronic Div, 1977.

[46] A. Demetriades, "Boundary-layer instability observations at Mach number 7," tech. rep., 1977.

[47] A. Demetriades, "New experiments on hypersonic boundary layer stability including wall temperature effects," in *Heat Transfer and Fluid Mechanics Institute, Meeting, 26 th, Pullman, Wash*, pp. 39–55, 1978.

[48] K. Stetson, E. Thompson, J. Donaldson, and L. Siler, "Laminar boundary layer stability experiments on a cone at Mach 8. i-sharp cone," in *16th Fluid and Plasmadynamics Conference*, p. 1761, 1983.

[49] K. Stetson, E. Thompson, J. Donaldson, and L. Siler, "Laminar boundary layer stability experiments on a cone at Mach 8. iii-sharp cone at angle of attack," in *23rd Aerospace Sciences Meeting*, p. 492, 1985.

[50] K. Stetson, E. Thompson, J. Donaldson, and L. Siler, "Laminar boundary layer stability experiments on a cone at Mach 8. iv-on unit Reynolds number and environmental effects," in *4th Joint Fluid Mechanics, Plasma Dynamics and Lasers Conference*, p. 1087, 1986.

[51] K. F. Stetson, E. R. Thompson, J. C. Donaldson, and L. Siler, "On hypersonic transition testing and prediction," *AIAA Paper*, no. 88-2007, 1988.

[52] K. F. Stetson, "On nonlinear aspects of hypersonic boundary-layer stability," *AIAA journal*, vol. 26, no. 7, pp. 883–885, 1988.

[53] K. Stetson, E. Thompson, J. Donaldson, and L. Siler, "Laminar boundary layer stability experiments on a cone at Mach 8. v-tests with a cooled model," in *20th Fluid Dynamics, Plasma Dynamics and Lasers Conference*, p. 1895, 1989.

[54] K. Stetson, R. Kimmel, J. Donaldson, and L. Siler, "A comparison of planar and conical boundary layer stability and transition at a Mach number of 8," in *22nd Fluid Dynamics, Plasma Dynamics and Lasers Conference*, p. 1639, 1991.

[55] K. F. Stetson and R. L. Kimmel, "Example of second-mode instability dominance at a Mach number of 5.2," *AIAA journal*, vol. 30, no. 12, pp. 2974–2976, 1992.

[56] K. F. Stetson and R. L. Kimmel, "Surface temperature effects on boundary-layer transition," *AIAA journal*, vol. 30, no. 11, pp. 2782–2783, 1992.

[57] K. Stetson and R. Kimmel, "On hypersonic boundary-layer stability," in *30th Aerospace Sciences Meeting and Exhibit*, p. 737, 1992.

[58] J. Laufer, "Aerodynamic noise in supersonic wind tunnels," *Journal of the Aerospace Sciences*, vol. 28, no. 9, pp. 685–692, 1961.

[59] M. V. Morkovin, "On supersonic wind tunnels with low free-stream disturbances," *Journal of Applied Mechanics*, vol. 26, no. 3, pp. 319–324, 1959.

[60] L. M. Mack, "Linear stability theory and the problem of supersonic boundary- layer transition," *AIAA Journal*, vol. 13, no. 3, pp. 278–289, 1975.

[61] L. M. Mack, "Stability of axisymmetric boundary layers on sharp cones at hypersonic mach numbers," in *19th AIAA, Fluid Dynamics, Plasma Dynamics, and Lasers Conference*, p. 1413, 1987.

[62] S. P. Schneider, "Effects of high-speed tunnel noise on laminar-turbulent transition," *J. Spacecraft and Rockets*, vol. 38, no. 3, pp. 323–333, 2001.

[63] S. P. Schneider, "Development of hypersonic quiet tunnels," *Journal of Spacecraft and Rockets*, vol. 45, no. 4, pp. 641–664, 2008.

[64] J. T. Lachowicz, *Hypersonic boundary layer stability experiments in a quiet wind tunnel with bluntness effects*. North Carolina State University, 1995.

[65] J. T. Lachowicz, N. Chokani, and S. P. Wilkinson, "Boundary-layer stability measurements in a hypersonic quiet tunnel," *AIAA journal*, vol. 34, no. 12, pp. 2496–2500, 1996.

[66] G. P. Doggett, *Hypersonic boundary layer stability on a flared-cone model at angle of attack*. North Carolina State University, 1996.

[67] A. E. Blanchard and G. V. Selby, "An experimental investigation of wall cooling effects on hypersonic boundary-layer stability in a quiet wind tunnel," tech. rep., NASA CR 198287, 1996.

[68] S. P. Wilkinson, "A review of hypersonic boundary layer stability experiments in a quiet Mach 6 wind tunnel," *AIAA 1997-1819*, 1997.

[69] J. Hofferth, R. Bowersox, and W. Saric, "The Mach 6 quiet tunnel at Texas A&M: quiet flow performance," in *27th AIAA Aerodynamic Measurement Technology and Ground Testing Conference*, p. 4794, 2010.

[70] J. Hofferth and W. Saric, "Boundary-layer transition on a flared cone in the Texas A&M Mach 6 quiet tunnel," in *50th AIAA Aerospace Sciences Meeting including the New Horizons Forum and Aerospace Exposition*, 2012.

[71] S. A. Craig, R. A. Humble, J. W. Hofferth, and W. S. Saric, "Nonlinear behaviour of the Mack mode in a hypersonic boundary layer," *J. Fluid Mech.*, vol. 872, pp. 74–99, 2019.

[72] S. A. Craig and W. S. Saric, "Crossflow instability in a hypersonic boundary layer," *J. Fluid Mech.*, vol. 808, pp. 224–244, 2016.

[73] J. Sivasubramaniam and H. F. Fasel, "Nonlinear stages of transition and breakdown in a boundary layer on a sharp cone at Mach 6," *AIAA 2012-0087*, 2012.

[74] P. S. Klebanoff, K. Tidstrom, and L. Sargent, "The three-dimensional nature of boundary-layer instability," *Journal of Fluid Mechanics*, vol. 12, no. 1, pp. 1–34, 1962.

[75] F. Siddiqui, W. S. Saric, and R. D. Bowersox, "Interaction of second-mode disturbances and 3-d roughness on a cooled flared cone at Mach 6," in *AIAA Scitech 2021 Forum*, p. 1092, 2021.

[76] I. E. Beckwith, "Development of a high Reynolds number quiet tunnel for transition research," *AIAA Journal*, vol. 13, no. 3, pp. 300–306, 1975.

[77] M. P. Borg and S. P. Schneider, "Effect of freestream noise on roughness induced transition for the X-51A forebody," *J. Spacecraft and Rockets*, vol. 45, no. 6, pp. 1106–1116, 2008.

[78] S. R. Pate and C. Schueler, "Radiated aerodynamic noise effects on boundary-layer transition in supersonic and hypersonic wind tunnels.," *AIAA Journal*, vol. 7, no. 3, pp. 450–457, 1969.

[79] I. Beckwith, F.-J. Chen, S. Wilkinson, M. Malik, and D. Tuttle, "Design and operational features of low-disturbance wind tunnels at NASA Langley for Mach numbers from 3.5 to 18," in *16th Aerodynamic Ground Testing Conference*, p. 1391, 1990.

[80] M. Kegerise and E. Spina, "A comparative study of constant-voltage and constant-temperature hot-wire anemometers part i: The static response," *Experiments in fluids*, vol. 29, no. 2, pp. 154–164, 2000.

[81] M. Kegerise and E. Spina, "A comparative study of constant-voltage and constant-temperature hot-wire anemometers: Part ii–the dynamic response," *Experiments in fluids*, vol. 29, no. 2, pp. 165–177, 2000.

[82] L. S. G. Kovasznay, "The hot-wire anemometer in supersonic flow," *J. Aero. Sci.*, vol. 17, no. 9, pp. 565–572, 1950.

[83] A. J. Smits, A. K. Hawakawa, and M. C. K, "Constant-temperature hotwire anemometer practice in supersonic flows – part 1: The normal wire," *Experiments in Fluids*, vol. 1, pp. 83–92, 1983.

[84] L. M. Weinstein, "Large-field high-brightness focusing schlieren system," *AIAA Journal*, vol. 31, no. 7, pp. 1250–1255, 1993.

[85] L. R. Boedeker, *Analysis and construction of a sharp focussing schlieren system*. PhD thesis, Massachusetts Institute of Technology, 1959.

[86] A. N. Leidy, *An Experimental Characterization of 3-D Transitional Shock Wave Boundary Layer Interactions at Mach 6*. PhD thesis, Texas A&M University, 2019.

[87] G. Smeets and A. George, "Application of laser differential interferometers to gas dynamics," *NASA STI/Recon Technical Report N*, vol. 75, p. 14123, 1973.

[88] G. Smeets and A. George, "Visualization methods using the differential interferometer," *NASA STI/Recon Technical Report N*, vol. 75, p. 25148, 1974.

[89] G. Smeets and A. George, "Instantaneous laser-doppler velocimeter using a fast wavelength tracking Michelson," *Journal Review Scientific Instrum*, vol. 49, p. 1589, 1977.

[90] G. Smeets and A. George, "Laser-differential interferometer applications in gas dynamics," tech. rep., Institut Franco-Allemand De Recherches Saint-Louis (France), 1996.

[91] A. Laderman and A. Demetriades, "Detection of boundary-layer transition with a laser beam," *AIAA Journal*, vol. 14, no. 1, pp. 102–104, 1976.

[92] M. Azzazy, D. Modarress, and T. Hoeft, "High sensitivity boundary layer transition detector," in *High speed photography, videography, and photonics III*, vol. 569, pp. 64–73, International Society for Optics and Photonics, 1986.

[93] M. Azzazy, D. Modarress, and T. Hoeft, "High-sensitivity density fluctuation detector," *Journal of Physics E: Scientific Instruments*, vol. 20, no. 4, p. 428, 1987.

[94] J. O'Hare, "A nonperturbing boundary-layer transition detector," in *High speed photography, videography, and photonics III*, vol. 569, pp. 58–63, International Society for Optics and Photonics, 1986.

[95] G. Smeets, "Laser-interferometer mit grossen, fokussierten lichtbündeln für lokale messungen," *Institut Saint-Louis Report ISL*, no. 11/73, 1973.

[96] N. J. Parziale, *Slender-body hypervelocity boundary-layer instability*. PhD thesis, California Institute of Technology, 2013.

[97] N. J. Parziale, J. E. Shepherd, and H. G. Hornung, "Free-stream density perturbations in a reflected-shock tunnel," *Experiments in fluids*, vol. 55, no. 2, pp. 1–, 2014.

[98] N. J. Parziale, J. E. Shepherd, and H. G. Hornung, "Observations of hypervelocity boundary-layer instability," *Journal of Fluid Mechanics*, vol. 781, p. 87–112, 2015.

[99] A. Hameed, N. J. Parziale, L. A. Paquin, C. Butler, and S. J. Laurence, "Hypersonic slender-cone boundary-layer instability in the UMD HyperTERP Shock Tunnel," in *AIAA Scitech 2020 Forum*, p. 0362, 2020.

[100] A. Roshko and H. Liepmann, *Elements of Gas-dynamics*. Wiley, 1957.

[101] M. Gragston, T. Price, K. Davenport, Z. Zhang, and J. D. Schmisseur, "Linear array focused-laser differential interferometry for single-shot multi-point flow disturbance measurements," *Opt. Lett.*, vol. 46, pp. 154–157, Jan 2021.

APPENDIX A

91-6 CONE DOCUMENTATION

Detailed calculations were carried out to verify the structural integrity of the model by its designers. Structural criteria from LHB1710.15 were used as a design guide. The model was designed to be able to withstand the loads it would be subjected to during wind-tunnel testing at 0° AoA with varying safety factors for various parts. The calculations can be found in a document named "Cryo-cone 3480-9304.pdf" on the NALshare server, in the sub folder named "91-6 Cooled cone design", which is in the "Drawings" folder. Also included are the drawings used to manufacture the model. These drawings can be helpful to understand how the model works and how the instrumentation is routed.

In case any repairs or refurbishing needs to be done a precision machining company has to be carefully selected. Most machine shops do not have the capability to work with the tolerances required for machining this model. Modern Machine & Tool Inc. in Newport News, VA is one company that is capable of working on this model. They have worked with NASA Langley for a long time manufacturing delicate and precise models and tunnel components. The drawings would be very helpful if any work needs to be done. A sample of the drawings is shown in Fig. A.1

The original manual of the recirculating chiller is also at the NAL and can be useful for troubleshooting any issues.

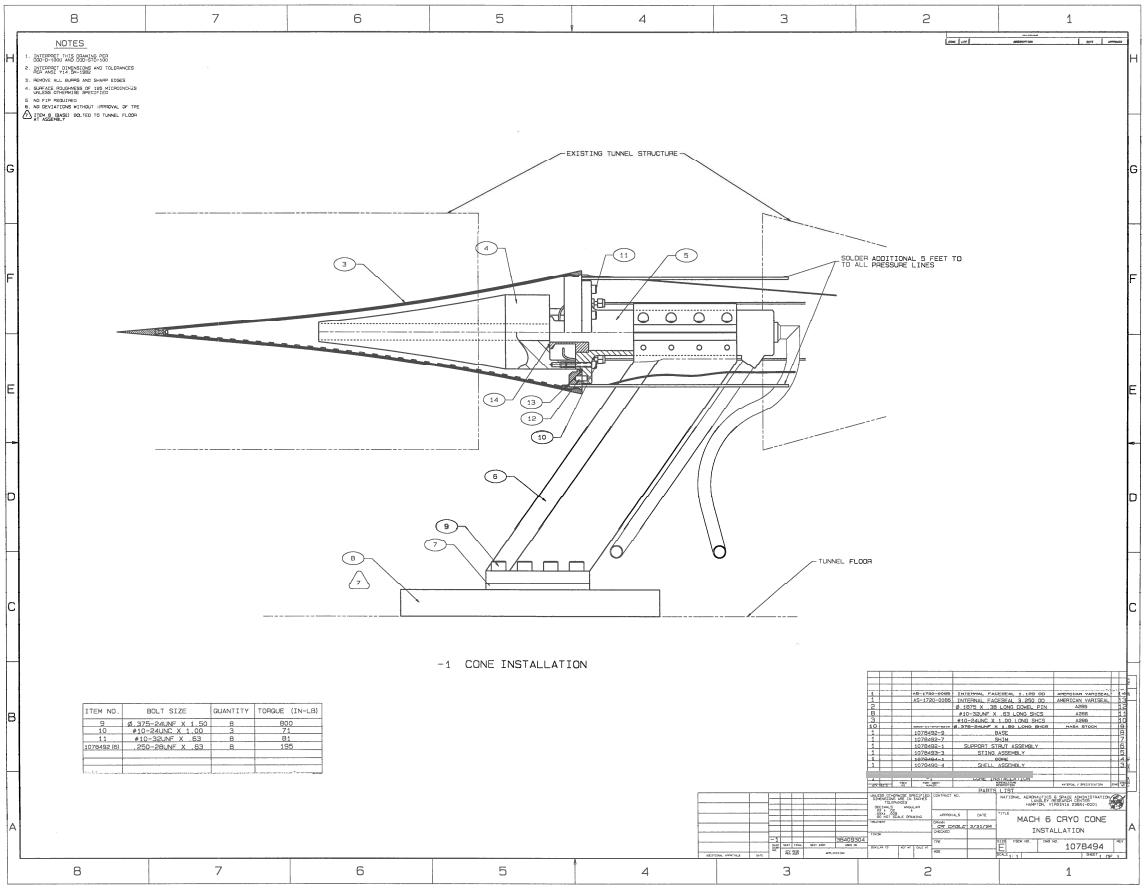

Figure A.1: One of the drawings used to manufacture the 91-6 cone model.